NTNU
Norwegian University of
Science and Technology

New Materials for Mg-ion batteries

Mn_3O_4 as cathode

Karina Asheim

Chemical Engineering and Biotechnology
Submission date: June 2016
Supervisor: Fride Vullum, IMTE
Co-supervisor: Lu Wang, IMT

Norwegian University of Science and Technology
Department of Materials Science and Engineering

Preface

This Master's thesis is written as the final part of the Master's degree program Chemical Engineering and Biotechnology at the Norwegian University of Science and Technology, NTNU. The work has been performed by the author at the Department for Materials Science and Engineering within the Inorganic Materials and Ceramics Research Group. The thesis work has been supervised by associate professor Fride Vullum-Bruer and co-supervised by Ph.D. candidate Lu Wang. The thesis is a continuation of the specialization project *New Materials for Mg-ion Batteries*, submitted by the author December 2015 [1]. Some results from that report will be presented again in the thesis to support findings. It will be stated which results this apply for.

I would like to thank my main supervisor, associate professor Fride Vullum-Bruer, first of all for giving me the opportunity to work with her and within the field of batteries. This has given me the chance to discover that energy storage is something I want to continue working with. Secondly, I want to thank for the guidance and motivation during the thesis work. Further, I want to thank my co-supervisor, Ph.D. candidate Lu Wang, for all the help with experimental work, for providing the electrolyte and for all constructive discussions about both our batteries. In addition, I want to thank Per Erik Vullum at SINTEF for being operator on TEM and providing very good images for the thesis. The technical staff at the department are also owed a thank for giving training in using equipment and help during experimental work.

Lastly, I need to thank my domestic partner, without whom I probably would not have had a single warm meal this last month.

Tondheim, June 14, 2016

Karina Asheim

Abstract

Due to drawbacks with the lithium ion battery technology, magnesium ion batteries are being researched as an alternative replacement system. An optimal combination of component materials has however not been discovered yet. This thesis investigates the unexplored Mn_3O_4 as a cathode material. A commercial powder was studied, and performance was determined for both pure Mn_3O_4 and powder subjected to simple treatments first. The treatments were milling and mixing with reduced graphene oxide. Mixing with reduced graphene oxide resulted in the highest performance, i.e. 78 $mAh\,g^{-1}$. Through charge-discharge cycling of cathodes with active mass between 1 and 2.7 mg, an active mass dependency on the capacity output was found. Long term cycling proved that the batteries can withstand 500 cycles, with no sign of failure. A rate dependency was also discovered, where it was found to occur more oxidation than reduction at low rates, owed to oxidation of the electrolyte solvent, THF. Ex situ study of cathodes, using SEM, XRD and TEM, revealed that Mg-ions attach on the cathode through a surface reaction during discharge.

Samandrag

Magnesium ionebatteri blir utforska som ei alternativ erstatning for litium ionebatteri grunna ulemper ved bruk av desse. Ein optimal kombinasjon av material for dei ulike komponentane i eit slikt batteri er ikkje funne enno. Denne oppgåva undersøkjer Mn_3O_4 som katodemateriale, då dette ikkje er gjort før. Eit kommersielt pulver er studert, og batterikapasitet er bestemt for både reint Mn_3O_4 og pulver utsett for enkle behandlingar først. Behandlingane var mølling og blanding med redusert grafenoksid. Blanding med redusert grafenoksid resulterte i høgast kapasitet, nemleg 78 $mAh\,g^{-1}$. Gjennom opplading og utladingssykling av katodar med aktiv masse mellom 1 og 2.7 mg, vart det oppdaga at kapasiteten avheng av aktiv masse. Langtidssykling beviste at batteria toler 500 syklar utan å vise teikn til å svikte. Ei hastigheitsavhengigheit vart også observert, der meir oksidasjon enn reduksjon fann stad ved lågare hastigheit. Dette er grunna oksidasjon av løysingsmiddelet i elektrolytten, THF. *Ex situ* undersøkingar av katodar, ved hjelp av SEM, XRD og TEM, avdekka at magnesiumion festast på katoden ved ein overflatereaksjon under utlading.

List of abbrevations

APC	$MgPhCl_2AlCl_3$
BET	Brunauer-Emmett-Teller
GBL	γ-butyrolactone
GO	Graphene oxide
LIB	Li-ion battery
MACC	Magnesium aluminum chloride complex
MIB	Mg-ion battery
NMP	N-methyl pyrrolidinone
RGO	Reduced graphene oxide
SE	Secondary electrons
SEM	Scanning electron microscopy
STEM	Scanning transmission electron microscopy
TEM	Transmission electron microscopy
THF	Tetrahydrofuran
XPS	X-ray photoelectron spectroscopy
XRD	X-ray diffraction

Contents

List of Figures

Chapter 1

Introduction

Development of Mg-ion batteries are at the research stage, aiming to become an alternative to Li-ion batteries. The Li-ion batteries are today the leading technology in energy storage. They are used in most portable electronics and also in electric vehicles [2]. This is due to the unique energy density these batteries possess. Li^+-ions are monovalent and have the second smallest ionic radius after hydrogen. Thus, Li^+-ions have an ease for reversible insertion into materials and is a suitable charge transfer specie [3]. However, there are some important drawbacks regarding cost, abundance and safety. The most important being safety since energy storage devices are a vital part of every day life. Thermal runaway is an effect causing Li-batteries to overheat till the point where they can catch fire or even explode [4]. It is not especially desirable to own an electric vehicle containing a battery that can catch fire during operation.

The world's energy demand, for transportation, grid storage and electronics, grow constantly larger. Due to the drawbacks with lithium, looking beyond this material to evaluate others is one way to proceed. Magnesium has been deemed the most promising candidate. Compared to lithium, magnesium is about 300 times more abundant, being the earth's sixth most abundant metal [2,5]. Also, Mg-ion batteries are safer in operation than Li-ion batteries since they do not suffer from thermal runaway or dendritic growth [5,6]. The last great advantage is the divalency of magnesium, providing two electrons per atom. This provides Mg with a higher volumetric capacity (3833 $\mathrm{mAh\,cm^{-3}}$), than Li (2046 $\mathrm{mAh\,cm^{-3}}$) [3].

The divalency of Mg causes however difficulties finding material systems where Mg can cycle reversibly. The high charge/radius ratio of Mg^{2+} causes interactions with the host ions in the cathode, resulting in slow insertion kinetics [2,7]. Different manganese oxides have been investigated as possible cathode materials for Mg-ion batteries. This is due to availability, cost and success in Li-ion battery systems [8]. However, there are still many unexplored materials when it comes to Mg-ion batteries. One such material is Mn_3O_4, which will be the focus of this work.

1.1 Aim of work

This Master's thesis will be a continuation of earlier work on Mn_3O_4 as a Mg-ion battery cathode, conducted by the author [1]. In the earlier work, commercial Mn_3O_4 provided by Erachem Comilog, was found to work as a cathode material for Mg-ion batteries. Knowing this, the main objective of this thesis will be to determine how the Mn_3O_4 is functioning as cathode material. By utilizing different characterization techniques, such as SEM, XRD and TEM, an attempt on revealing the charge and discharge mechanism at the cathode will be made. How Mn_3O_4 act as cathode for the Mg^{2+}-ions during charge and discharge is vital knowledge when evaluating the potential this material has as a Mg-ion battery cathode.

In addition, attempts will be made to find how well this commercial powder can perform with simple treatments. Such a simple treatment will be milling down the initial powder. This will investigate the effect of surface area on the capacity. An interesting feature found in the earlier work was a possible capacity dependency on active mass. This will be investigated more in order to be able to verify. Also, earlier work showed very stable performance of the cathodes. This stability will be investigated further by long term cycling of batteries, which also will serve as a verification of durability.

Chapter 2

Theory

2.1 Rechargeable batteries

Batteries are charge storage devices. They convert chemical energy stored in materials into electrical energy through electrochemical oxidation and reduction [9]. In a battery the main components are the anode, cathode and electrolyte. The two electrodes are connected by an external circuit and are internally in contact with the electrolyte.

A primary battery can only be discharged once. Here, the anode is the negative electrode where oxidation occurs when electric contact with the cathode is established by the external circuit. During the discharge, electrons from the oxidation pass through the external circuit to the cathode. At the same time, positive ions are released from the anode into the electrolyte. The cathode is the positive electrode where reduction occurs when the electrons from the anode and the positive ions in the electrolyte reach the cathode.

In a rechargeable battery, reduction and oxidation occur at both electrodes depending on whether the battery is being charged or discharged. Here, the cathode is defined as the most positive electrode. Recharging the battery occurs by applying a voltage, forcing the electrons in the opposite direction compared to the discharge. The cathode is then the site for oxidation, while reduction occur at the anode. Both the electrons and ions transferred to the cathode during discharge are transferred back to the anode during charging, restoring the battery. The working principle of a rechargeable battery is shown in Figure 2.1.

So, the anode and cathode in a rechargeable battery are the sites for both oxidation and reduction. As established above, the electrons involved in these reactions are transferred between the electrodes through an external circuit. To ensure good electronic contact, the cathode is on top of a current collector. The electrolyte, being the medium between the electrodes is responsible for the transport of charge as ions. Thus, the electrolyte must have high ionic conductivity. The medium can however not be electronically conductive as this would cause internal short circuiting. All internal electric contact between the electrodes

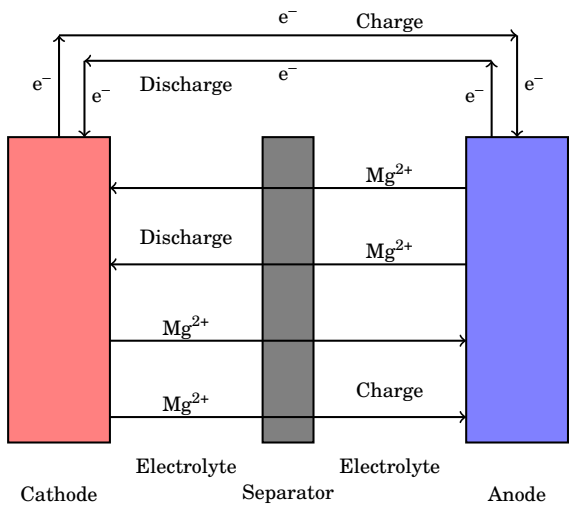

Figure 2.1: Working principle of a rechargeable battery.

would cause short circuiting, hence the electrodes must be kept apart from each other. A separator between the electrodes ensures this.

All the components needed in a rechargeable battery is hence; anode and cathode, connected by an external circuit, electrolyte and a separator. These components must fulfill certain requirements in order for the battery to function well. The separator, sitting right in the middle of the cell, must be permeable and chemically compatible with the electrolyte. Unintended reactions between the electrolyte and separator would cause unwanted damage to the cell. The anode in Mg batteries is usually metallic Mg, but can in theory also be an intercalation anode, like graphitic carbon is in Li-ion batteries [9]. The cathode must be able to host the active ions in the structure, and release them during charging. The insertion and release of the active ions should proceed easily and reversibly. Lastly, the electrolyte must preferably be compatible with all the other components in the cell, so that transport of the positive ions between the electrodes can run without any unwanted reactions. Hence, the electrolyte should support reversible deposition and dissolution of Mg^{2+} on the Mg anode, ensure anodic reaction stability and not cause corrosion of the current collector [2]. Compatibility with the anode is demonstrated by a good Coulombic efficiency which is defined as the ratio of the charge accumulated during the Mg deposition/dissolution.

2.1.1 Electrochemical testing

Electrochemical tests are required to determine how well a battery works. The capacity the battery works at is the important feature. The capacity is a measure of how much charge the battery delivers during discharge and stores during charge. Hence, the capacity should be both high and stable. A stable battery would show negligible decrease in capacity during

cycling, indicating good reversibility of the redox reactions occurring in the cell. In order to measure the capacity, galvanostatic cycling (or voltammetry) is performed. Batteries are then charged and discharges between two set voltage values at a constant current rate [9]. By including the active mass of the cathode, the specific capacity of the cathode is measured continuously. The resulting data from this test is often presented as charge-discharge curves where voltage is plotted against specific capacity. That way, the obtained capacities can be seen at the endpoint of the curves while the oxidation- and reduction reactions are illustrated as plateaus on the curves.

Another test able to provide information about the battery performance is cyclic voltammetry (CV). In this test the voltage is controlled while the responding current is measured. The result is a current-voltage curve showing at which voltages the oxidation- and reduction reactions occur. An example of a CV curve, collected from [9], is given in Figure 2.2. The voltage difference between the peaks for oxidation and reduction is in this figure denoted ΔE. This corresponds to the voltage difference between the plateaus at the charge and discharge curves in a plot showing specific capacity obtained during gavanostatic cycling. Ideally, for reversible reactions, ΔE should be close to zero [9], as smaller ΔE indicate faster kinetics [10].

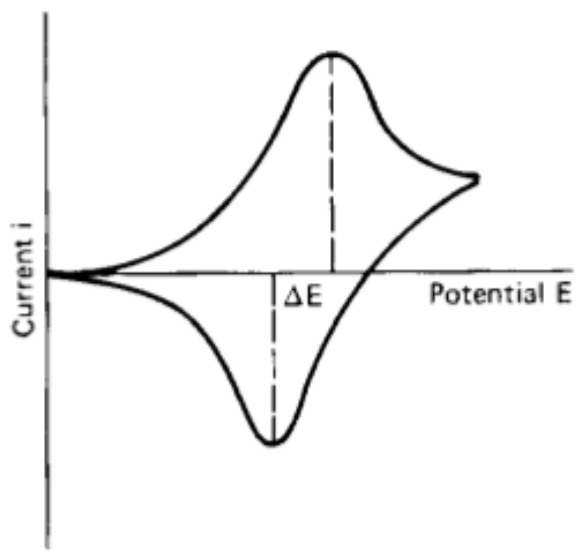

Figure 2.2: Illustration of CV curve for a reversible process, collected from [10]. ΔE is the voltage separation between the two peaks.

Cyclic voltammetry is a well established electrochemical test used for several types of devices, not only batteries. One of these devices, baring resemblance to batteries, is capacitors. Capacitors are energy storage devices like batteries, however for these devices the energy is stored by charge separation [11]. An electrochemical capacitor is very similar to batteries.

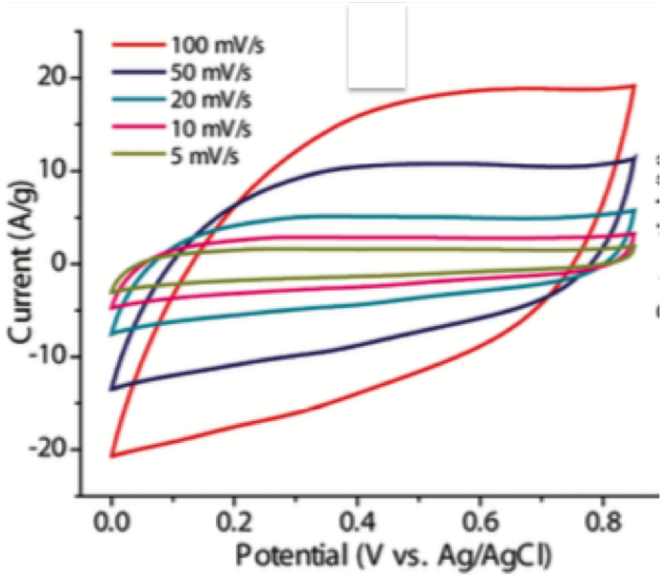

Figure 2.3: Illustration of CV curve for an electrochemical capacitor, collected from [12]. The figure was part of a study testing electrode of a ternary system containing graphene, MnO_2 and carbon nanotubes.

There, two electrodes are immersed in electrolyte and kept apart from each other with a separator. However, a requirement is that the electrodes are made from a material with both high surface area and high porosity. Charge is then stored in micropores at or near the interface between the electrode and the electrolyte. A cyclic voltammogram of a capacitor is similar to that of a battery, but without the peaks for oxidation and reduction. It looks more like a rectangle, the size varying depending on the cycling rate. An example of CV curves for a capacitor is shown in Figure 2.3, which is collected from a study on improving MnO_2 as electrode material for electrochemical capacitor [12].

2.2 Established materials for Mg-ion batteries

Development of Mg-ion batteries has been an ongoing process since started by Gregory et al. in the 1980s [13]. In this section, materials for the different components in a Mg-ion battery, except the cathode, will be briefly described. Cathode materials will be looked more closely into in the next section.

For the anode, the easiest is to use pure magnesium metal. As long as any oxide layer is removed before assembly to battery, the pure metal works well. Since magnesium is cheap and abundant, there is no major downside to using the pure metal. However, magnesium alloys have been found to work as good as, and even better than, pure magnesium [14]. This is due to the alloy's higher resistance against oxidation, which makes it easier to handle during processing. A thin layer of oxide on the anode would passivate the surface and prevent

both oxidation and reduction of Mg during charge/discharge. Seeing as alloy is cheaper than pure metal, using an alloy as anode material instead of pure metal also lowers the total cost. An important aspect for a battery anode, learned from Li-ion batteries, is ion deposition on the surface. In Li-ion batteries having Li metal anode, the ions depositing on the anode surface have dendritic growth, leading to poor cycling performance [15]. In addition, if the dendrites grow large, they can come into contact with the cathode causing short circuiting and spontaneous rapid discharging, resulting in heating of the cell and explosion [16]. Magnesium on the other hand is shown not to grow in dendritic morphologies [6]. The reason for this difference is that the Mg-Mg bond is stronger than the Li-Li bond [17].

The electrolyte for Mg-ion batteries have been through much development since the first working composition was found in 1990. This electrolyte was made from Grignard reagents (RMgX, where R = alkyl or aryl group and X = Cl or Br) mixed with aluminum halides in an ethereal solution [13]. During testing, the transfer of Mg between electrodes occurred at a current efficiency of 99.9 %. However, the electrolyte solutions based on Grignard reagents are strong reducing agents, and have a low anodic stability [2]. Ten years later, a new electrolyte based on magnesium organohaloaluminate salts, $Mg(AlCl_2BuEt)_2$, in tetrahydrofuran (THF) was discovered [18]. In this, deposition-dissolution of Mg at the anode was reversible at almost 100 % efficiency and the anodic stability window increased to 2.2 V vs Mg. In 2007, the electrolyte was once again improved. This time by replacing all the organic ligands with phenyl groups [19]. This resulted in improved ionic conductivity and the anodic stability was enhanced from 2.2 to 3.2 V. The electrolyte formula was $MgPhCl_2AlCl_3$ (APC) and the solvent was unchanged, i.e. THF. This electrolyte is the one used today.

THF is used in electrolytes for Mg batteries due to it being a polar aprotic solvent. Aqueous, or protic, solvents react with Mg and form a passivating oxide layer on the anode surface. Mg^{2+} can not pass through this layer, thus it prevents ionic transport [20]. Conventional electrolyte systems will react on the Mg surface and create such a layer which blocks movement of Mg^{2+} completely. When using THF as solvent, this is prevented.

The separator is glass fiber. It provides sufficient distance between the anode and cathode, thus preventing short circuiting. The glass fiber is permeable to the electrolyte and Mg^{2+}-ions so these can cycle back and fourth between the electrodes. Another important feature for the separator is chemical compatibility with the electrolyte. The separator is right in the middle of the cell so there can be no unwanted reactions between the electrolyte and the separator. THF is not the easiest solvent to work with, the boiling point for example is only at 65 °C [21], so the compatibility can be a serious issue. However, no reports have been found which suggests that glass fiber causes problems in the Mg-ion batteries using THF containing electrolyte.

When it comes to the current collector on the other hand, there are several reports on compatibility problems with the electrolyte. Metal current collectors (stainless steel, aluminum,

nickel) have been found to corrode in Cl^- containing electrolyte [22–24]. Corrosion of current collector can change the practical voltage window the cell operates in [2]. However, it has been found that carbon paper is compatible with the electrolyte and do not corrode, thus the electrochemical oxidation stability is not affected [25].

2.3 Cathode materials for Mg-ion batteries

The search for cathode materials for Mg-ion batteries (MIBs) has been going on since Gregory et al. did the first test on some alternatives [13]. Since then many more alternative materials have been explored. Two well investigated and relevant candidates will be described below, after some practical cathode features are noted.

2.3.1 Important features for MIB cathode

A good cathode for Mg-ion batteries need both high ionic and electronic conductivity to be able to transport charge through the material. In order for reversible intercalation to occur, the material must have available space to accommodate the Mg^{2+}-ions and have multivalent ions to maintain the electroneutrality. The cathode morphology on micro scale should be porous so that electrolyte can come into contact with as much particle surface as possible.

First of all, the electronic conductivity is necessary for the reduction and oxidation reactions to occur. Electrons must be transferred into and out of the cathode during discharge and charge respectively. If the cathode material itself is not conductive, the active material must be deposited onto a current collector which is electronically conductive. Also, addition of an electronic conductive material, like carbon, to the cathode during fabrication can be a mean to ensure or enhance the electronic conductivity.

Ionic conductivity is also an obvious feature for an intercalation cathode. The material needs to allow reversible intercalation of the positive Mg^{2+}-ions. This has however proved itself to generally be more difficult than to intercalate Li^+ions. Magnesium is an earth alkali metal in the upper left corner of the periodic table of elements. Litium, being an alkali metal, is found in the same area, though in the neighboring column. Elements with close proximity in the periodic table, often have similarities with regard to some features. The ionic size is one of these. Mg^{2+} has ionic radius of 0.72 Å when the coordination number is 6, and 0.57 Å when the coordination number is 4. Li^+ has ionic radius of 0.59 Å when the coordination number is 4 and 0.76 Å when the coordination number is 6 [26, 27]. Seeing as Li^+ easily can be inserted into other materials, ionic size cannot be the restricting factor for Mg. An important difference between Mg and Li is however the valence. Being divalent gives Mg a much higher charge/radius ratio than Li. This causes strong electrostatic interactions with the ions in the cathode material. Such a polarization effect causes slow solid state diffusion of Mg^{2+} into the cathode, hence lowers the insertion kinetics [28].

Slow kinetics give poor performance. Means to increase the kinetics should then be found. Decreasing the particle size of the active material is a well known method for increasing the kinetics. A decrease in particle size would give a higher surface area, which means that more electrolyte comes into contact with active surface sites on the cathode material. Then, more electrochemical reactions would occur, and with thin pore walls the diffusion path for electrons and ions would be shorter providing faster kinetics [29]. It is also of importance that the pores have a suitable size. Micropores have for LIBs been found to be too small for electrolyte complexes [30]. The microporous surface will hence not be utilized. Thus, the particle size, the pore size distribution and the surface area of the active cathode material play an important role in determining the kinetics.

A second and third possible reason for poor Mg solid state diffusion, besides the polarization effect are hard redistribution of host ion's charge and Mg trapping [31]. With regard to the charge redistribution, a reduction must compensate the insertion of Mg^{2+}. If the cathode consist of Mn^{4+}, the compensation can either be that per Mg^{2+}-ion inserted, one Mn^{4+} is reduced to Mn^{2+}, or that two Mn^{4+} are reduced to Mn^{3+}. The problem with these two reactions are firstly that when manganese is reduced from Mn^{4+} to Mn^{2+}, the size of the ion increases by a factor of 1.75 which would cause local distortion. Secondly, creating two Mn^{3+}-ions per Mg^{2+}-ion inserted means that quite a lot of Jahn-Teller active ions are formed. Mn^{3+} have four electrons in the d-orbital and is a Jahn-Teller active ion. It prefers octahedral coordination and the d-electrons are placed in high-spin configuration [32]. $LiMn_2O_4$, for example, is a LIB cathode having instability due to the local Jahn-Teller distortion in the Mn^{3+} octahedra [33].

2.3.2 Manganese oxide, MnO_2

MnO_2 have been investigated extensively as cathode material for several types of batteries, especially lithium batteries [8, 34]. Reasons for the use of MnO_2 are abundance, cost and stability, which are all favorable. Depending on the arrangement of the MnO_6 octahedra making up the structure, MnO_2 can have many polymorphs [34]. Several of the MnO_2 polymorphs have also been investigated for use as MIB cathode. Two examples are $\alpha-MnO_2$ and $\gamma-MnO_2$, which will be described below.

$\alpha-MnO_2$

$\alpha-MnO_2$ has a tunnel structure, where double chains of MnO_6 octahedra are interlinked so that one-dimensional channels, with relative dimentions (2x2) and (1x1), run through the structure [8]. An illustration of the structure is provided in Figure 2.4.

As a Mg-ion battery cathode, $\alpha-MnO_2$ initially showed good potential. The material provided an initial capacity of 280 $mAhg^{-1}$ [35]. However, this faded to below 100 $mAhg^{-1}$ during the first few cycles. The tunnel structure of $\alpha-MnO_2$ was believed to collapse during Mg insertion. This due to formation of Jahn-Teller active Mn^{3+} which distorts the MnO_6

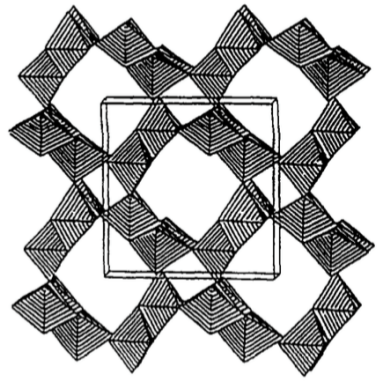

Figure 2.4: Crystal structure of $\alpha-MnO_2$. Collected from [8].

octahedra to the point where the structure collapses. For the recharge, the results indicated a recovery of the $\alpha-MnO_2$ structure, however not completely. XRD diagram showed that discharged material had lower peak heights than as-prepared material.

Later, it was found that the discharge product at the $\alpha-MnO_2$ cathode was a core-shell structure, i.e. with a crystalline MnO_2 core and an amorphous shell [36]. The amorphous shell was not possible to remove again, and consisted of MgO and MnO. Hence, the magnesiation occurs through a conversion reaction. When $\alpha-MnO_2$ is cathode in LIBs on the other hand, lithiation occurs through intercalation with no formation of amorphous layer. It was discovered that the conversion reaction forming the amorphous shell was thermodynamically favorable over intercalation for this material. For the same magnesiation level, the amorphous MnO and MgO were more stable than the intercalated compound. The stability of MgO was believed to be the driving force for the conversion reaction. Also DFT calculations indicated that the reaction path for mangesiation of $\alpha-MnO_2$ would follow the conversion reaction [37]. However, findings suggested a kinetic barrier against direct conversion, in which case intercalation could occur up to a limited concentration [38]. With magnesium concentration higher than $\alpha-Mg_{0.125}MnO_2$ the structure was predicted to undergo a strong tetragonal to orthorombic distortion, which could ruin the host framework.

The distortion occurs because intercalation of Mg^{2+} causes reduction of Mn^{4+} to Mn^{3+}, which causes Jahn-Teller deformation. One axis expands while another shortens as shown in Figure 2.5 collected from [38]. Each cavity in the $\alpha-MnO_2$ structure have four sites available for Mg ions. At the composition $\alpha-Mg_{0.5}MnO_2$, half of these cavity sites are occupied. Mg ion number two will place itself furthest away from the first Mg ion due to electrostatic repulsion. So both structural integrity and electrostatic repulsion suggests concentration of Mg can not exceed $\alpha-Mg_{0.5}MnO_2$.

Diffusivity is also an important factor. For concentration of Mg less than 0.25, hopping barriers are comparable to Li diffusion. At Mg concentration higher than 0.25 the barrier

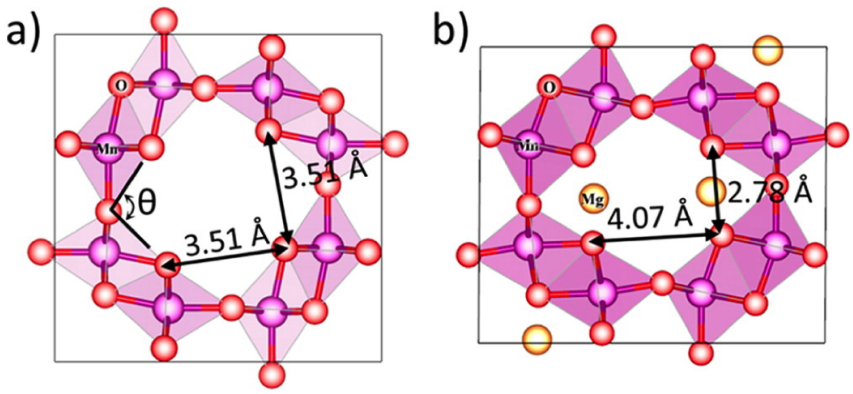

Figure 2.5: (a) Structure of pristine $\alpha-MnO_2$. (b) Structure of $\alpha-Mg_{0.5}MnO_2$ after the insertion of two Mg ions in the same cavity. Collected from [38].

increases to the point where it is suggested not to be kinetically practical. This due to distortion blocking the diffusion path [38].

Yet another study of $\alpha-MnO_2$ revealed that the surface area determined the capacity [39]. When the surface area was higher than 70 $m^2 g^{-1}$, the material performed well at a capacity around 250 $mA h g^{-1}$. When the surface area was below 70 $m^2 g^{-1}$, the capacity decreased to around 50 $m^2 g^{-1}$. Surface area dependency also suggest conversion reaction.

In summary, it is very unlikely that magnesiation of $\alpha-MnO_2$ occur through intercalation. Theoretical and experimental studies strongly indicate a conversion reaction, possibly with some limited intercalation first.

$\gamma-\mathbf{MnO_2}$

Another MnO_2 polymorph is spinel-Mn_2O_4 (or $\gamma-MnO_2$). $LiMn_2O_4$ is actually a commercialized cathode for Li-ion batteries. If the lithium is removed, the cubic spinel structure is maintained and have been found to be able to intercalate divalent ions without destroying the structure [40]. An illustration of the crystal structure of $\gamma-MnO_2$ with intercalated M^{2+}-ions is given in Figure 2.6. Mg^{2+} was in this study found to intercalate reversible into $\gamma-MnO_2$ providing a specific capacity of 155 $mA h g^{-1}$ after 300 cycles. The discharge product was determined, by X-ray photoelectron spectroscopy (XPS) measurements, to be $MgMn_2O_4$. The authors also proposed intercalation of divalent ions into the spinel structure of Mn_2O_4 presented in equation (2.1), where x and y have values between 0 and 1.

$$[]_{8a}[]_{16c}[Mn_2]_{16d}[O_4]_{32e} + M^{2+} + 2e^- \rightleftharpoons [M_x]_{8a}[M_y]_{16c}[Mn_2]_{16d}[O_4]_{32e} \tag{2.1}$$

The different notations in equation (2.1) indicate sites in the spinel structure. In each unit cell there are the same number of octahedral sites as there are oxygen ions, and twice as many tetrahedral sites. However, all of these cannot be occupied. Only half of the octahedral sites and 1/8 of the tetrahedral sites are filled. One unit cell contains 32 oxygen

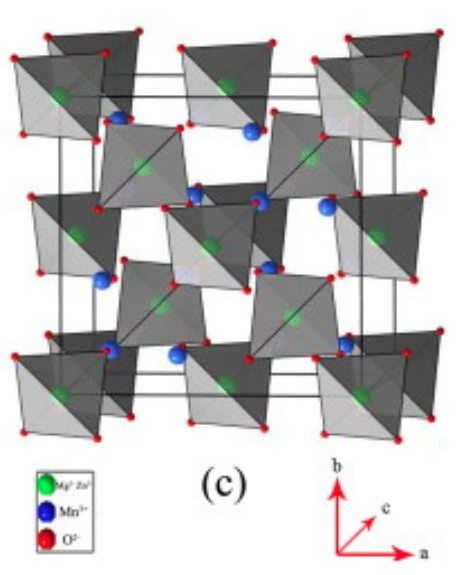

Figure 2.6: Structure of $\gamma-MnO_2$ with intercalated M^{2+}-ions. Collected from [40].

ions, hence there are 8 occupied tetrahedral sites and 16 occupied octahedral sites in a unit cell [41]. Thus in (2.1) above, the site notation 8a is for tetrahedral hole, 16c and 16d are for octahedral holes and 32e is for oxygen sites. This means that manganese originally occupy octahedral 16d sites, while during intercalation Mg^{2+}-ions are inserted into vacant 8a and 16c sites. This accompanied by the reduction of Mn^{4+} to Mn^{3+}.

For the material it was found that the discharge capacity decreased at higher current densities, suggesting that electron transport was greater than the diffusion rate of Mg^{2+}. Hence, mass-transfer control is the rate-determining step at high current densities [40].

Another study also proved reversible intercalation of Mg^{2+} into tetrahedral sites in spinel Mn_2O_4 [42]. The position Mg took in the structure was revealed by scanning transmission electron microscopy (STEM) with element analysis, and X-ray diffraction (XRD) analysis determined that the formed structure bare close resemblance to $MgMn_2O_4$. Element mapping found approximately 11 atom% Mg uniformly distributed. Formation of $MgMn_2O_4$ would correspond to a theoretical capacity of 270 $mAh\,g^{-1}$. STEM image of the crystal structure of $MgMn_2O_4$ is given in Figure 2.7. Hence this is the discharged spinel Mn_2O_4.

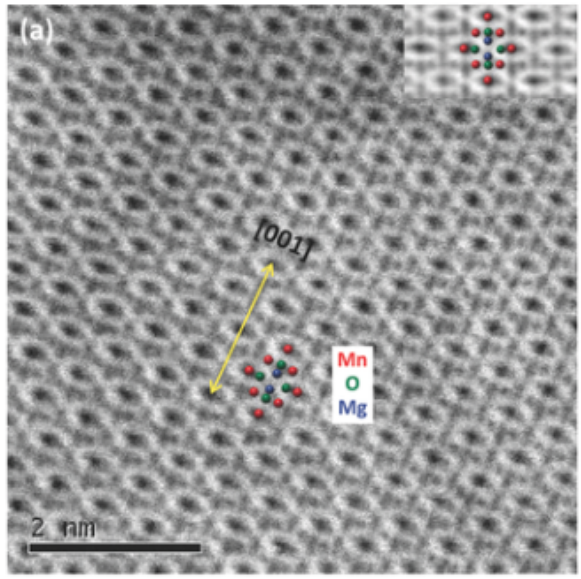

Figure 2.7: STEM image of crystal structure for discharged $\gamma-MnO_2$ with intercalated M^{2+}-ions. Collected from [42].

2.4 Manganese tetraoxide, Mn_3O_4

Mn_3O_4 has the normal spinel crystal structure with the general formula:

$$A^{tet}B_2{}^{oct}O_4$$

where $B_2{}^{oct}O_4$ is organized in the rock salt structure with ccp (closest cubic packing) of O^{2-} and the B cation in alternate octahedral sites. Due to cation-cation repulsion, the A cation can only occupy tetrahedral sites where all the four neighboring octahedral sites are empty. Occupied tetrahedral and octahedral sites can thus not be face sharing [32]. The crystal structure of Mn_3O_4 is illustrated in Figure 2.8, and the structure formula of Mn_3O_4 is:

$$[Mn^{2+}]^{tet}[Mn_2^{3+}]^{oct}O_4$$

The structure have tetrahedral and octahedral holes where foreign ions in theory can insert. The sizes of these tetrahedral and octahedral sites in the spinel structure can be calculated by;

$$r_t = 0.225 r_a \tag{2.2}$$

$$r_o = 0.414 r_a \tag{2.3}$$

where r_t is radius of a tetrahedral site, r_o is radius of octahedral site and r_a is radius of the anion [44]. The O^{2-}-ions are closest cubic packed, thus their coordination number is 6 and

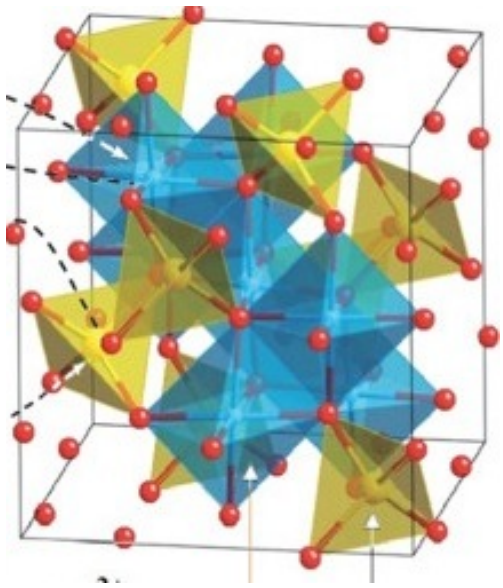

Figure 2.8: Illustration of the spinel structure for Mn_3O_4, collected from [43]. The red dots are oxygen atoms, the Mn^{3+}-ions are placed within the blue octahedra and the Mn^{2+}-ions are placed within the yellow tetrahedra.

the ionic radius of the anions is 1.4 Å [26]. The tetrahedral sites then have radius of 0.315 Å, while the octahedral sites have a radius of 0.580 Å.

As can be seen in Figure 2.8, Mn_3O_4 has closely spaced octahedral sites that share edges. The tetrahedral sites share corners only with the octahedral sites. This causes quite some distance between the Mn^{2+}-ions and the Mn^{3+}-ions. Electron exchange is therefore difficult and this causes Mn_3O_4 to be an insulator. Despite this, the material has a theoretical capacity of 154 $mAh\,g^{-1}$ as MIB cathode [13]. In addition, poor conductivity can be compensated by structuring and coating. An example is adding another material with high electronic conductivity to ensure this property.

2.4.1 Commercial Mn_3O_4

A commercially available Mn_3O_4 was in earlier study by the author [1] investigated as cathode material for MIBs. It was then found that the performance of pure Mn_3O_4 was well below the theoretical capacity. The commercial powder used had a low surface area and agglomerated particles. During performance testing, batteries with Mn_3O_4 cathode, Mg metal anode and APC electrolyte were cycled 50 times. Resulting charge-discharge curves had evident plateaus indicating reactions. Cyclic voltammetry was also performed on the cathodes, the result given in Figure 2.9.

As an attempt to increase the capacity output of the cathodes, the Mn_3O_4 powder was mixed with reduced graphene oxide. This did indeed result in improved performance, and it was

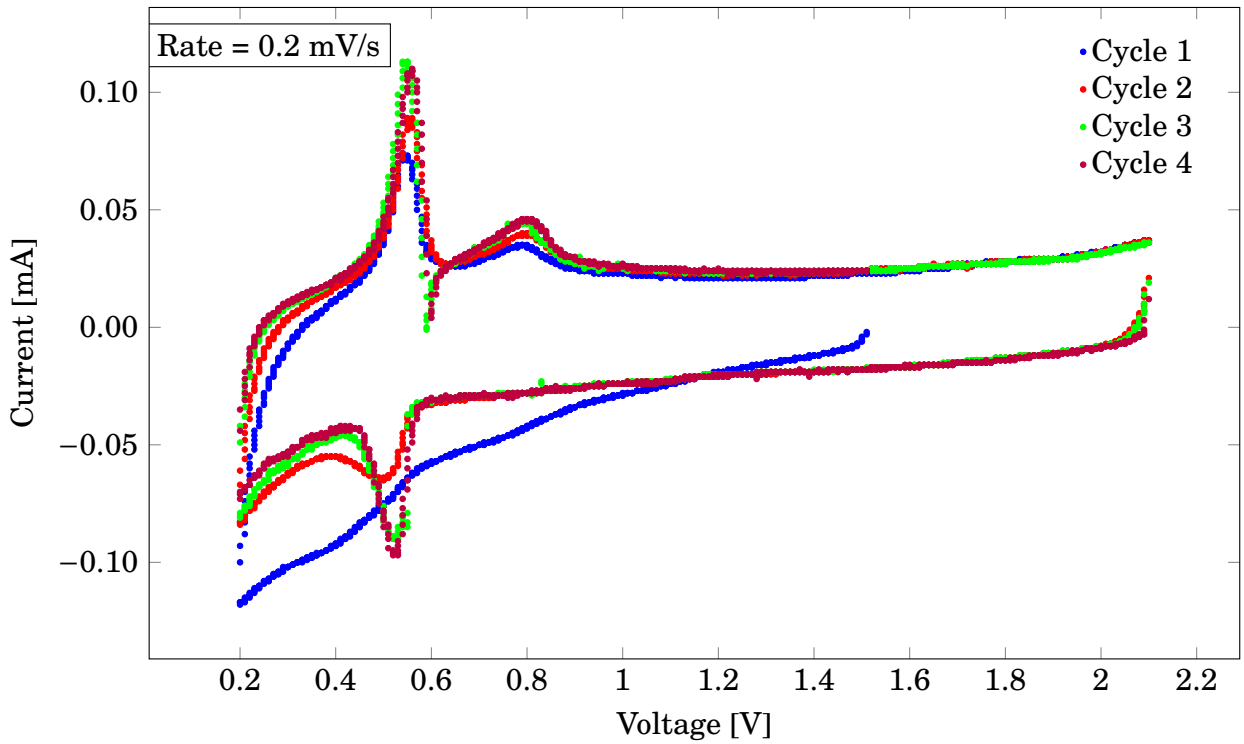

Figure 2.9: Cyclic voltammetry curves for Mn_3O_4. Collected from earlier work [1].

discussed if that was owed to increase in electronic conductivity, kinetics, or both.

2.4.2 Graphene as means for increasing capacity

Graphene is monolayers of carbon atoms packed in a honeycomb lattice. This material has excellent electrical conductivity and extremely high specific surface area. By mixing graphene with materials for electrodes, these wanted properties can contribute to increasing the performance of the electrodes for energy storage systems. Reduced graphene oxide is graphene oxide sheets where some of the oxide groups are reduced leaving functional groups. These groups can be utilized for attaching [45] or growing [46] metal oxide particles on. The reduced graphene oxide sheets form a network that help disperse the metal oxide particles so that the active surface area increases, giving faster transport of electrons [46]. This provides specific capacities higher than the sum of the capacities for the metal oxide and graphene sheets alone [45]. Mn_3O_4 is one metal oxide that has been grown on reduced graphene oxide resulting in better performing electrodes for supercapacitors [47]. The increase in performance was due to higher utilization of the Mn_3O_4 particles because they were more dispersed.

2.5 New findings for electrolyte

A new, stable, inorganic-based electrolyte was discovered about two years ago. This solution is a magnesium aluminum chloride complex (MACC) in THF, which provides reversible Mg deposition with an anodic stability over 3.0 V [48, 49]. The precursors are the non-nucleophilic Mg^{2+} source, $MgCl_2$, and the Al Lewis acid, $AlCl_3$. The solution was found to need an electrolytic precycling process to achieve the desired electrochemical performance [50]. During this precycling it was discovered an irreversible Mg and Al deposition on the anode. The process also resulted in free Cl^- anions in the electrolyte, which depassivates the anode surface, thereby allowing a reversible Mg deposition/dissolution [51]. In addition, inhibitory oligomers develop in the THF via a cationic ring-opening polymerization of THF during initial synthesis of the MACC and under resting conditions [50]. $AlCl_3$ acting as a Lewis acid can catalyze this polymerization, while conditioning, or precycling, removes them again. After the conditioning, reversible Mg deposition occurs.

When the Mg organohaloaluminate $Mg(AlCl_2EtBu)_2$ in THF recently was investigated, some new discoveries were made. The presence of γ-butyrolactone (GBL) was revealed in the solution [52]. This is a known oxidation product of THF, and it was found in both the $Mg(AlCl_2EtBu)_2$ electrolyte and the Grignard reagent EtMgBr. The authors hypothesize that the THF molecules coordinate to RMg^+ species at the electrode surface, and that these are more easily oxidized than uncoordinated THF due to the Lewis acidity of RMg^+. Lewis acids have been reported to facilitate the chemical oxidation of THF to GBL. This GBL decomposition product was also found in the MACC electrolyte [50].

Chapter 3

Experimental work

The experimental work performed for this thesis can be divided into six parts; powder preparation, powder characterization, cathode fabrication, cell assembly, electrochemical testing and ex situ study of the cathodes. All these parts will be described in the following sections.

3.1 Powder preparation

Two powders were prepared in this work. The starting point was a commercial Mn_3O_4 powder from Erachem Comilog, which was tested as a Mg-ion battery cathode material in earlier work by the author [1]. As attempts to improve the performance, simple treatments of the powder was the first step here. The treatments were milling and mixing with reduced graphene oxide. These two powder preparation methods are described in the following sections.

3.1.1 Milling

Earlier study of the commercial Mn_3O_4 (Erachem Comilog) powder showed that the powder had very low active surface area [1]. As an attempt to increase the surface area of this powder, ball milling was performed. The milling balls used were made of yttrium stabilized zirconia, and the milling medium, or solvent dispersing the powder, was aceton. This was all mixed together in a plastic bottle as container. By rotating the bottle continuously, the milling balls tumbles over each other and crush large agglomerates in the powder. The commecial Mn_3O_4 powder was milled for 16 hours, before it was dried and collected as a brown powder. An illustration of the cross section of a working ball mill is shown in Figure 3.1. When milling, there is a critical rotation speed which if exceeded causes the milling balls to follow the wall of the container all the way around. This instead of tumbling down on the powder as shown in Figure 3.1, which is the wanted process. The formula for the critical rotation speed is given as Equation (3.1).

$$V_{cr} = 42.3/(D)^{1/2} \tag{3.1}$$

Where D is the diameter of the container and the unit for V_{cr} is rpm (rotations per min).

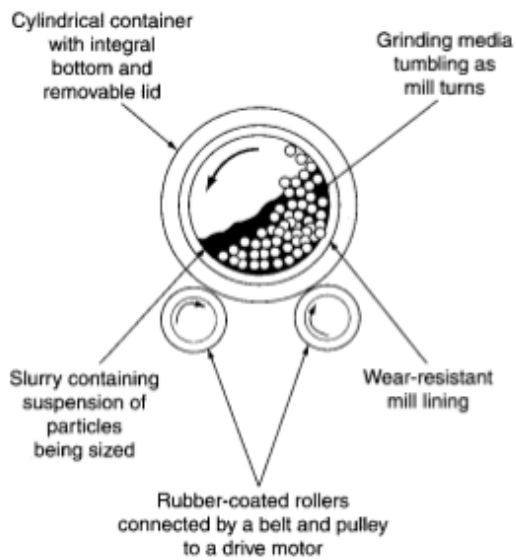

Figure 3.1: Working principle of a ball mill, collected from [53].

3.1.2 Milled Mn_3O_4 mixed with reduced graphene oxide

Due to the advantageous properties graphene oxide possesses, a batch of milled Mn_3O_4 powder mixed with reduced graphene oxide was prepared. Then, 0.2 g graphene oxide (GO) was dispersed in 200 mL distilled water. The solution was ultrasonicated in a Branson digital sonifier (Danbury, USA) at 60 % effective power for 20 - 30 min. After this the solution was centrifuged at 3000 rpm for 10 min. 7 - 8 droplets of a 25 wt% ammonia solution was added to adjust the pH to 10 and help keep the GO sheets from agglomerating. Then, the solution was ultrasonicated again at the same power, this time for 45 - 50 min. Next step was adding 1.13 g dry, milled commercial Mn_3O_4 to the solution while stirring. The stirring was continued for 2 hours before the solution was heated, still with stirring, to 85 °C. When this temperature was reached, 5 wt% hydrazine (N_2H_4) was added as a reduction aid. The weight ratio between GO and N_2H_4 was 10:7, hence 2.8 g of the 5 wt% hydrazine solution was added. The solution was kept at 85 °C while stirring over night. After this, the solution was centrifuged and washed until the pH was 7. Finally the powder was dried and collected as a black and dark brown powder.

3.2 Powder characterization

After milling the commercial Mn_3O_4 powder, it had to be characterized using N_2 adsorption-desorption measurements and SEM. This to evaluate the effect of milling and determine both the new surface area and particle size and morphology. The characterization methods are described in the following sections.

3.2.1 BET

To find the active surface area of the milled Mn_3O_4 powder, N_2 adsorption and desorption measurements were performed using a 3Flex surface and catalyst characterization machine from Micromeritics. The surface area was calculated using the Brunauer-Emmett-Teller (BET) method. To remove any adsorbed water, the sample was degassed at 250 °C under vacuum over night before measuring.

3.2.2 SEM

Scanning electron microscopy (SEM) was used to study particle size and morphology. The milled Mn_3O_4 powder, both pure and complexed with RGO, was imaged. Preparing the powders for SEM involved dispersing them in 100 % ethanol and keep these dispersions in an ultrasonication bath for 40 min. After this, two droplets of the dispersions was deposited onto a clean sample holder each. When dry, the sample of pure Mn_3O_4 was sputter coated with carbon nanoparticles (a few nano meters in size), to ensure conductivity. The samples were imaged in the field emission SEM (FESEM) Zeiss Ultra with secondary electrons using an acceleration voltage of 5 kV. The obtained SEM images are presented in the results section.

3.3 Cathode fabrication

To make cathodes, the pure Mn_3O_4 powder was mixed with Super-P carbon black and polyvinylidene difluorid (PVDF, Keynar, reagent grade) in the presence of N-methyl pyrrolidinone (NMP, Aldrich, > 99 %). This by the weight ratio 80:10:10 respectively. The last component is a binder and solvent solution. Additional droplets of the NMP was used to adjust the viscosity. For pure Mn_3O_4 15 additional droplets of NMP were used, and for the Mn_3O_4 complexed with RGO 30 droplets were used. After adding all the components to a metal container with a metal ball inside (shaker mill), the mixture was ball milled into a stable slurry by a Retsch MM400 shaking machine. The slurries were shaken for 30 min with frequency 25 s^{-1}. Next the slurries were drop coated onto carbon paper discs, 16 mm in diameter. These had been cut from carbon paper, cleaned with ethanol and dried over night under vacuum at 80 °C. Carbon paper with slurry was placed on a hot plate, having an approximate temperature of 50 °C, until dry. Then, the cathodes were dried under vacuum at 120 °C over night (t > 10 hours).

3.4 Cell assembly

In order to test the performance of the cathodes fabricated, coin cell batteries were assembled as described below.

3.4.1 Coin cell battery

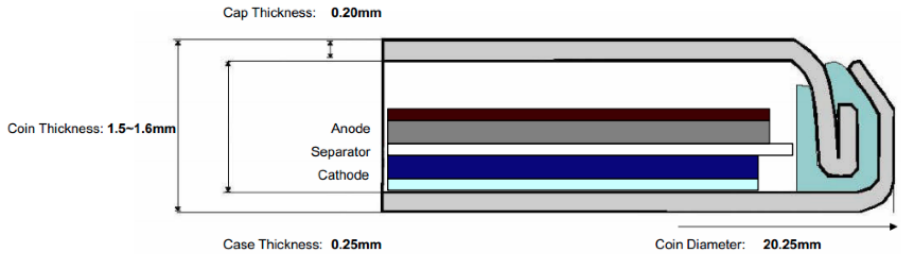

Figure 3.2: Partial cross section of an assembled coin cell battery. Collected from [54].

The coin cell batteries prepared were CR2016 coin cells from Hohsen Corp. An illustration of the cross section of such a battery is shown in Figure 3.2. The illustration also gives the dimensions of a finished assembled cell, i.e. the diameter is 20.25 mm and the hight is 1.6 mm. Before the battery components were put into the bottom case of the battery, a plastic ring was put in. This ensured complete sealing of the cell when the top was pressed on. Since the anode, cathode and separator are not thick enough to fill the entire height of the cell, a metal (stainless steel) spacer was also included. Hence, the assembly order was; bottom case, plastic ring, cathode, separator, anode, spacer and top. Electrolyte was added drop wise onto the cathode, separator and anode to ensure complete soaking. Approximately 12 droplets of electrolyte were in total used for each cell.

The stainless steel spacer was 16 mm in diameter and 0.3 mm thick. The anode was a 12 mm long, pure magnesium piece from a Mg ribbon, 3 mm wide. The Mg ribbon was polished using sandpaper to remove all the oxide on the surface, washed with ethanol and dried under vacuum overnight at 80 °C before use. The separator was a glass microfiber (Whatman) disc, 16 mm in diameter. The APC electrolyte, prepared by Ph.D. candidate Lu Wang according to synthesis procedure [18, 19], had a concentration of 0.4 mol L^{-1} APC. Assembly was done in an Ar-filled glove box (p_{O_2} and p_{H_2O} < 0.1ppm).

3.5 Battery testing

In order to test the performance of the batteries made, they were charge-discharge cycled glavanostatic, i.e. by controlling the current and measuring the voltage response. Three different programs were run on the batteries to study different performance features. The programs are called short term performance, long term performance and rate capability. These programs are described in the following sections. The battery tester used, for all tests, was Landhe CT2001A, shown in Figure 3.3.

3.5.1 Short time performance

The short term test involves cycling the batteries between 2.1 V, charged state, and 0.2 V, discharged state, for 50 cycles. One cycle is one charge and one discharge. A freshly assembled battery is fully charged, hence the program starts with a discharge. This discharge is labeled initial discharge, and is not part of cycle one. The charge/discharge rate used was 0.1C, where 1C is the current density needed to charge/discharge the battery in one hour, i.e. 154 $\mathrm{mAhg^{-1}}$. By entering the active mass of the cathode, the specific capacity of the cathode is measured continuously. This test gives a good indication of the performance since 50 cycles is long enough to know that the battery does not fail very soon after it is put to use, and also the rate is slow enough to get quite some reaction and thus capacity.

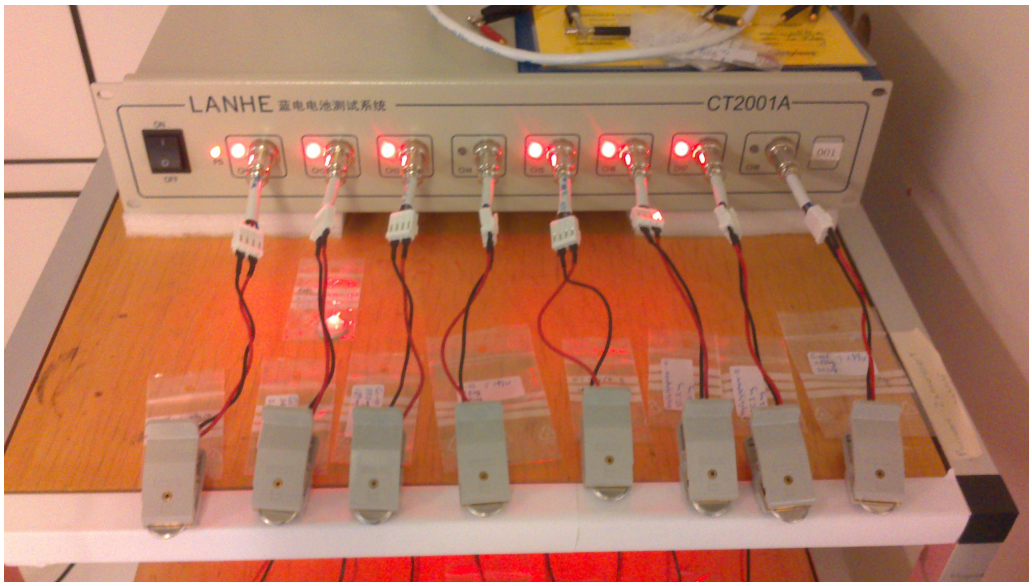

Figure 3.3: 2016 coin cell batteries being electrochemically tested with charge-discharge cycling by Landhe battery testing machine. Collected from [1].

3.5.2 Long term performance

Long term performance of cathodes were done to verify the capacity stability seen in earlier work and to ensure that the batteries do not short circuit after a few hundred cycles. The cathodes were assembled to batteries, which were set to cycle between 2.1 and 0.2 V 500 times at a current rate of 0.1C.

3.5.3 Rate capability

To see how the specific capacity of the cathodes varies with current rate. The cycling program set for these cathodes cycled them five times at each of the following current rates; 0.05C, 0.1C, 0.2C, 0.5C, 1C, 2C, 5C and then back to 0.05C. This way it would be possible to

determine if the capacity returns back to the initial value after cycling at all the different current rates or if there is a permanent effect.

3.6 Ex situ study of cathodes

Different ex situ studies were performed on the cathodes. These were XRD, SEM with EDS analysis and TEM with element analysis. The aim of these studies was to reveal what happens with the cathode material during operation, i.e. an attempt to discover the working mechanism. To do so, cathodes at different stages of cycling were needed. Hence, several batteries were made having the same type of cathode (pure milled Mn_3O_4) and charge-discharge cycled to different end points. The procedures for preparation and executing the studies are described in the following sections.

3.6.1 Sample preparation for ex situ studies

To investigate if or how the cathode material changes during cycling, six cathodes were initially prepared. One was to be a reference to the others and was hence remained fresh. The other five were assembled into batteries and programmed to cycle to different end points using the Lanhe machine. The first of these five batteries only completed the initial discharge to 0.2 V, before the battery was disassembled and the cathode was cleaned in THF and dried. The second battery completed the initial discharge and the first charge. The third battery completed cycle 1, i.e. initial discharge, first charge and second discharge. The fourth battery was stopped at the evident charging plateau in cycle 5, i.e. at 0.6 V. The fifth battery was stopped at the discharge plateau in cycle 5, i.e. at 0.5 V. The six cathodes were labeled A - F respectively. Disassembly, cleaning and drying of the cycled cathodes were done in an Ar-filled glove box (p_{O_2} and $p_{H_2O} < 0.1$ppm). The charge/discharge rate used was 0.02C to ensure as much reaction as possible.

Cycle five was chosen for plateau examination because here the plateaus are well established and experience from earlier work indicate that much of what happens with the cathode during 50 cycles have already happened at cycle five. Meaning that the largest changes in the charge-discharge curves occur between cycle one and five, and only small changes are seen from cycle five to fifty.

Preparation for XRD

After the cathodes were dry, they were prepared for XRD analysis. This preparation included carefully scraping active material off the carbon paper and depositing it on a clean, flat sample holder of Si single crystal. In order to make the material stick to the sample holder, about eight droplets of ethanol (96 %) were deposited on the sample holder before the active material. The ethanol was allowed to dry before the samples were placed in the

XRD machine. The samples were scanned in a Bruker D8-Focus. The recorded XRD patterns are given in the results section.

Preparation for SEM and EDS

When preparing the cathodes for XRD, only half of the active material was scraped off the cathode. The other half was, for cathode A - D, images in SEM to study the surface morphology and to look for differences between the fresh and cycled cathodes. Since the surface morphologies were to be studied and the Mn_3O_4 active material was deposited onto conductive carbon paper, no sample preparation was necessary. The cathodes were merely transferred into the SEM and the uncompromised half of the cathodes were imaged. The SEM used was the field emission SEM (FESEM) Zeiss Ultra with secondary electrons using an acceleration voltage of 5 kV. The obtained SEM images are presented in the results section.

After SEM imaging, EDS analysis was performed on the cathodes to determine the amount of the different elements in the active material. Using a Bruker Quantax EDS detector, spectra of each cathode was obtained and analyzed using the Quantax Espirit program. The analysis results are given in the results section.

Preparation for TEM

Preparation for transmission electron microscopy (TEM) involved firstly carefully scraping the active material off cathode C and D, which had been cycled to charge and discharge of cycle 1. The sample powders where then dispersed in 96 % ethanol. A droplet from each dispersion was transferred to a holey carbon coated Cu TEM grid. Prior to TEM characterizations, the samples were gently plasma cleaned 2 x 10 s inside a shielding port by a Fischione plasma cleaner to remove possible contamination.

TEM was performed with a double Cs corrected, coldFEG JEOL ARM200CF, operated at 200 kV and equipped with a Gatan Quantum ER for electron energy loss spectroscopy (EELS) and a large solid angle (0.98 srad) Centurio detector for X-ray energy dispersive spectroscopy (EDS).

Chapter 4

Results

In this section results from the experimental work will be presented. The results are divided into three main sections; powder characterization, cathode electrochemical performance and investigations of charge-discharge mechanism.

4.1 Powder characterization

The milled Mn_3O_4 powder was characterized by N_2 adsorption-desorption measurements and SEM imaging in order to determine the effect of milling. Therefore the characterization results will be compared to results for untreated Mn_3O_4 found in earlier work [1]. In the following sections the measured active surface area will be presented first, followed by particle size and morphology results obtained by study using SEM.

4.1.1 Active surface area

N_2 adsorption-desorption measurements and calculations utilizing the Brunauer-Emett-Teller (BET) method gave an active surface area of 11.3 $m^2 g^{-1}$ for the milled Mn_3O_4 powder. From this 10.6 $m^2 g^{-1}$ was external surface area and 0.7 $m^2 g^{-1}$ was micropore area. Hence, close to all of the active area is accessible. Investigations on not milled Mn_3O_4 conducted in earlier work found a BET surface area of 9.6 $m^2 g^{-1}$ [1]. This implies that milling the powder resulted in an increase in surface area by 15 %. As both the increase and the total surface area are low, the powder should still contain mostly large agglomerated particles.

The isotherm linear plot is shown in Figure 4.1. The two lines, indicated by dots, illustrating adsorption and desorption show that the micropore area is an insignificant part of the surface area [55]. There are no hysteresis in the curves, hence the powder is macroporous. This again indicates large particles and agglomeration. From the surface area an estimated particle size can be calculated. Assuming spherical particles, equation (4.1) can be used. The estimated particle size is then found to be 113 nm. For the not milled powder

this calculated size was 123 nm [1].

$$S = \frac{6}{d\rho} \tag{4.1}$$

Equation (4.1) gives the relationship between the surface area, S, the material's density, ρ and the particles' average diameter, d assuming spherical particles. The density value, ρ, of Mn_3O_4 used was 4.7 $g\,cm^{-3}$ [27].

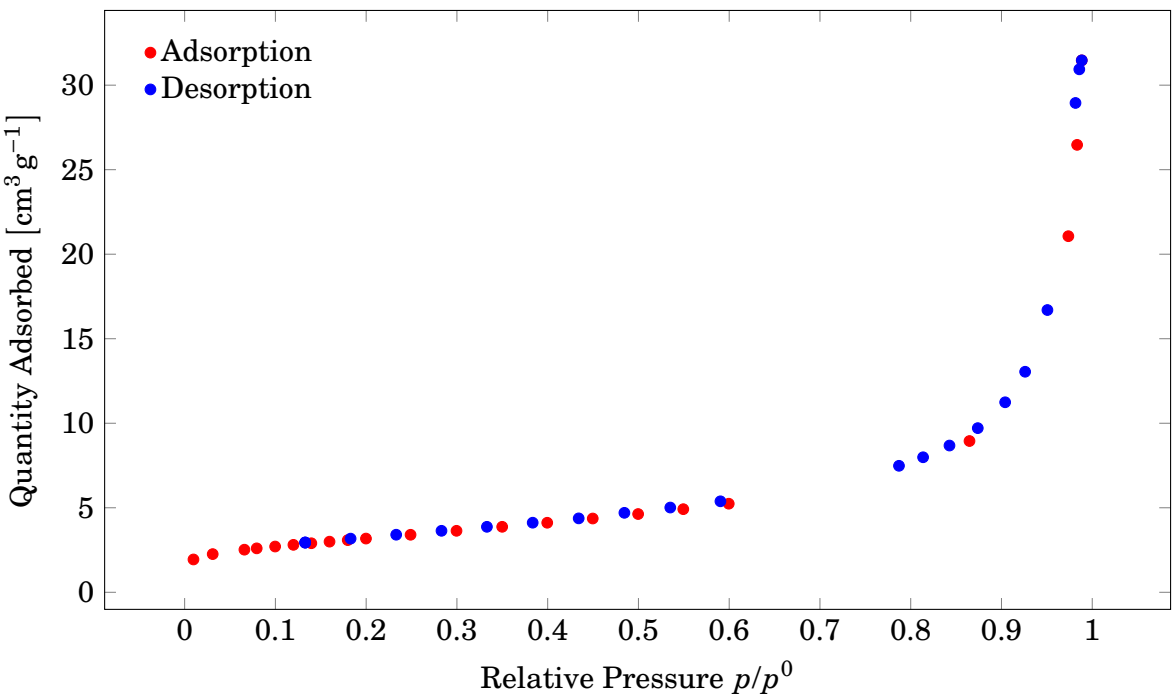

Figure 4.1: Isotherm linear plot from N_2 adsorption-desorption measurement and BET calculations. The red dots indicate adsorption and the blue dots indicate desorption.

4.1.2 Particle size and morphology

In order to determine the size and morphology of the milled Mn_3O_4 powder, SEM and TEM was used to image the powder. The obtained images are divided into two groups, pure Mn_3O_4 and Mn_3O_4 complexed with RGO, and are presented in that order. To determine the effect of milling, SEM images of the milled Mn_3O_4 are given alongside SEM images of not milled Mn_3O_4. The images of not milled Mn_3O_4 are collected from earlier work [1]. TEM images were only obtained for pure, milled Mn_3O_4 as these were taken as part of the ex situ study described in the experimental section. Hence the agglomerates shown in the TEM images are from a cycled cathode.

Pure Mn_3O_4

Four images of pure Mn_3O_4 are presented in Figure 4.2. Two of these, Figure 4.2a and 4.2c, are of untreated Mn_3O_4, while Figure 4.2b and 4.2d are of milled Mn_3O_4. All images were taken using secondary electrons (SE), and the out of lens SE detector. When observing the four images, milling seems to have reduced the sizes and density of the agglomerates. Clearly there are still much agglomeration after milling, but each agglomerate looks to be smaller in size and less densely packed with particles. Estimated reduction in agglomerate size due to milling is from 1 - 2 µm in diameter to 0.5 - 1 µm in diameter, see Figure 4.2a and 4.2b. Also for the not milled powder, the agglomerates are seen to be closely linked together, creating a large system of agglomeration. The milled powder does not seem to have the same strong linking between agglomerates. In addition for the milled powder, there are some visible open channels in between the particles making up each agglomerate. For the not milled powder, some channels between the agglomerates are seen, but due to the dense packing of particles within each agglomerate there are no visible channels through the agglomerates.

To evaluate change in particle size caused by milling, Figure 4.2c and 4.2d are studied. From these images it is seen that the particles' sizes are quite similar before and after milling. For both powders, it can be seen that the particles have a wide size distribution. From the images it can be observed both particles smaller than 50 nm and larger than 100 nm. Though it can be noted that the agglomerate in Figure 4.2d seem to have more of the smaller particles than the agglomerate in Figure 4.2c. In addition, the shape of the particles vary some. While the smaller particles look quite spherical, the larger ones have a rectangular shape. This is seen for the powder both before and after milling. The rectangular shape is particularly noticeable for the not milled powder, but can also be found in the milled powder. The rectangular particles looks to have a length more than twice as long as the width.

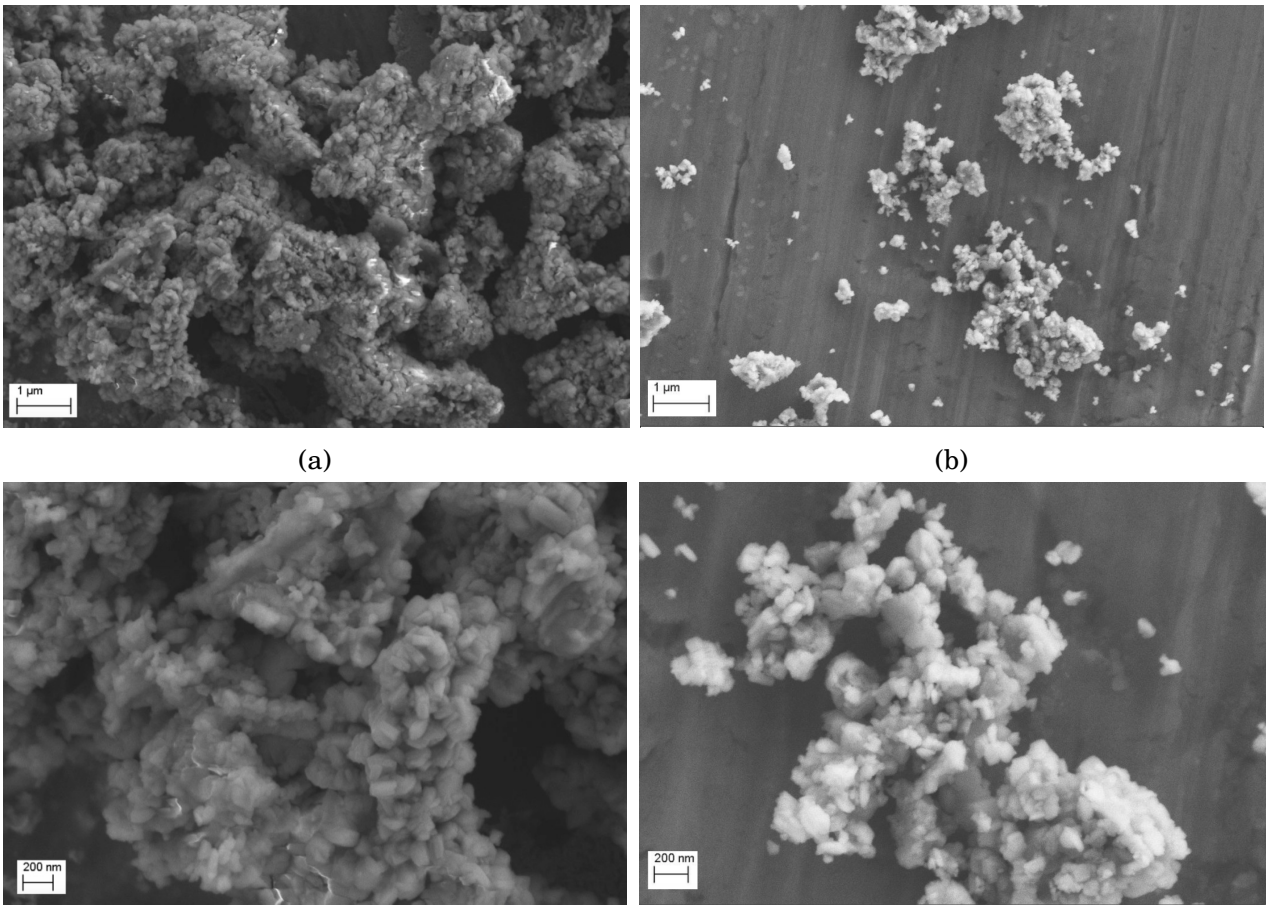

(a) (b)

(c) (d)

Figure 4.2: SEM images of (a) and (c) the untreated commercial Mn_3O_4 at different magnifications, and (b) and (d) the milled Mn_3O_4 at similar magnifications as the untreated samples for comparison. Image (a) and (c) are collected from earlier work [1].

In order to evaluate the size and morphology of the milled Mn_3O_4 powder more thoroughly, TEM was also used. This was done as part of the ex situ study of cathodes described in the experimental section. In Figure 4.3 four TEM images are presented, illustrating how wide the size and shape distribution of the agglomerates are. The agglomerate in Figure 4.3a is both large, about 3 µm long, and quite densely packed. The agglomerate in Figure 4.3b on the other hand is both smaller, about 2 µm long, and less densely packed. This agglomerate will hence have a larger accessible surface area. In Figure 4.3c and 4.3d the particles building up the agglomerates can be observed. From these images it is clear that the particles have varying size. The upper left particles in Figure 4.3c are seen to be rectangular with length of around 150 nm and width between 50 and 100 nm. The largest particles seen in Figure 4.3d are at the bottom of the agglomerate. These are also rectangular, though here the length is about 60 nm while the width is about 40 nm. In the upper part of this agglomerate several smaller particles can be seen, many of which looks to be elongated in one

direction. Some of these are not larger than 20 nm. Hence, the particle size distribution in the powder is wide.

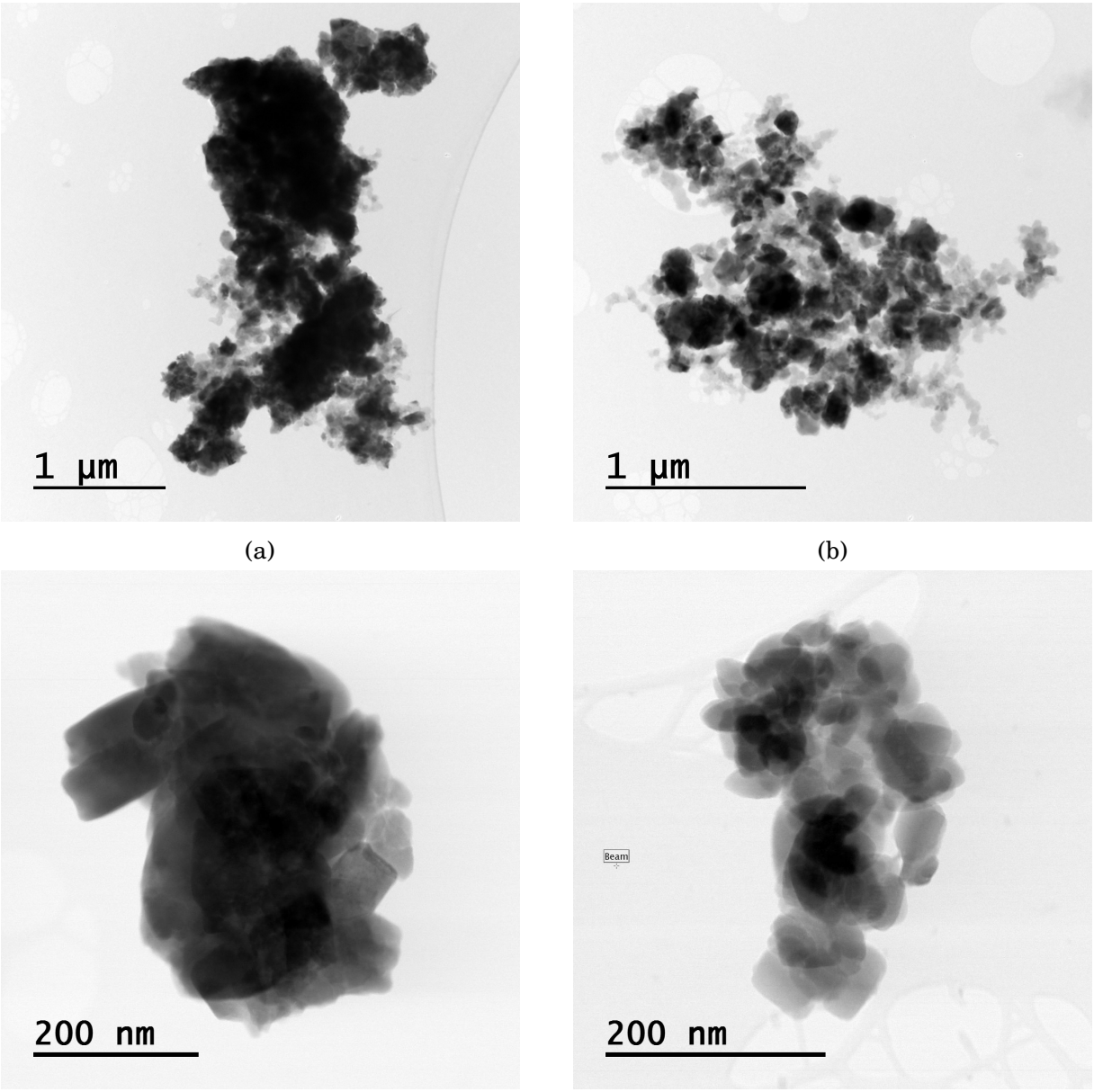

(a) (b)

(c) (d)

Figure 4.3: TEM images of agglomerates in milled powder.

Mn_3O_4 mixed with RGO

For the samples mixed with RGO, four SEM images are presented in Figure 4.4. Two of which are of samples where the Mn_3O_4 was not milled, Figure 4.4a and 4.4c, while Figure 4.4b and 4.4d are of samples where the Mn_3O_4 was milled before mixing. Here image 4.4c was taken using the secondary electron detector outside the microscope lens, while image 4.4a, 4.4b and 4.4d were taken using the SE detector in the lens to better see the RGO sheets. The new, milled powder looks porous and have the reduced graphene oxide sheets more intertwined in between the agglomerates. In the not milled powder, the RGO sheets looks to be wrapping the agglomerates, see Figure 4.4a. There are however some less agglomerated areas, as can be seen in Figure 4.4c. Still, the mixing looks more successful for the milled powder. The RGO sheets seems more dispersed throughout the Mn_3O_4 particles, instead of being layers of sheets wrapping the agglomerates.

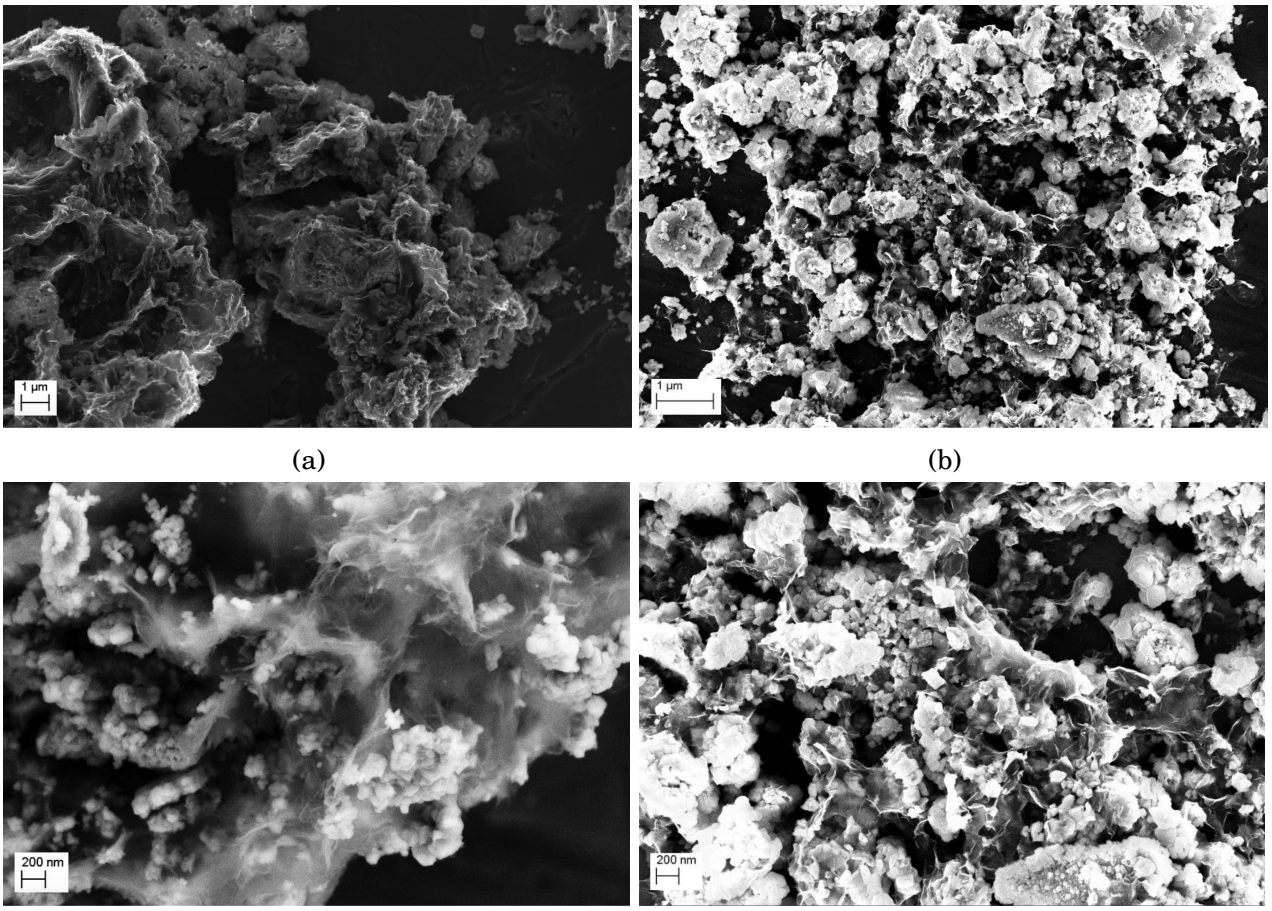

(a) (b) (c) (d)

Figure 4.4: SEM images of (a) and (c) the not milled Mn_3O_4 powder mixed with RGO, and (b) and (d) the milled Mn_3O_4 complexed with RGO. Image (a) and (c) are collected from earlier work [1].

4.2 Cathode electrochemical performance

Four types of cathode have been tested by charge-discharge cycling between the voltages 0.2 and 2.1 V. These are untreated, commercial Mn_3O_4, pure and mixed with RGO, and milled, commercial Mn_3O_4, pure and mixed with RGO. Several performance features were studied for these cathodes. They involve specific capacity obtained during short term performance tests, capacity dependence on active mass, long term performance and rate capability. Obtained results on these features will in that order be described in the sections below.

4.2.1 Short term performance

Untreated Mn_3O_4

Six cathodes of untreated Mn_3O_4 have been tested in this work. All of these had active mass below 2 mg and will be compared to earlier work where 4 cathodes with active mass above 2 mg were tested. In this section, the best and poorest performing of these 10 cathodes will be presented with charge-discharge curves, while the other cathodes are given in Appendix A.1.

The best performing cathode of untreated Mn_3O_4 is shown with charge-discharge curves in Figure 4.5. In the plot, the black line is the initial discharge, the red lines are charge and discharge of cycle one, the green lines are cycle five and the blue lines are cycle fifty. Average specific capacity obtained with this cathode was 50 $mAhg^{-1}$ and the cathode's active mass was 1.36 mg. From the initial discharge to the first charge, a decrease in capacity from about 61 to 45 $mAhg^{-1}$ is seen. From the charge to the discharge of cycle 1 the capacity increases to 51 $mAhg^{-1}$. In cycle five, the charge capacity is slightly larger than the discharge, measuring 53 and 50 $mAhg^{-1}$ respectively. For cycle 50, the charge capacity continued increasing while the discharge showed decreasing capacity compared to cycle 5. The respective values were 55 and 46 $mAhg^{-1}$.

From the charge-discharge curves it can also be seen that there is a close to horizontal segment, or plateau, on each curve except for the initial discharge. For the charge curves, these plateaus are at approximately 0.7 V, and it can be seen that the plateaus for cycle 5 and 50 are wider in x-direction than the plateau for cycle 1. For the discharge curves, cycle 1 do not actually have a plateau, only a change in curve slope. Cycle 5 and 50 however, have clear plateaus around 0.6 V. The curves for cycle 5 and 50, both charge and discharge, are seen to be almost the same, with only slight differences at the end of the curves and at the plateaus. Both the charge and the discharge plateau show a slight upwards shift in voltage from cycle 5 to cycle 50.

The poorest performing cathode on the other hand is illustrated with charge-discharge curves in Figure 4.6. The average specific capacity of this cathode was 24 $mAhg^{-1}$ and the active mass was 2.72 mg. Looking at the endpoints of the curves, a drop in capacity

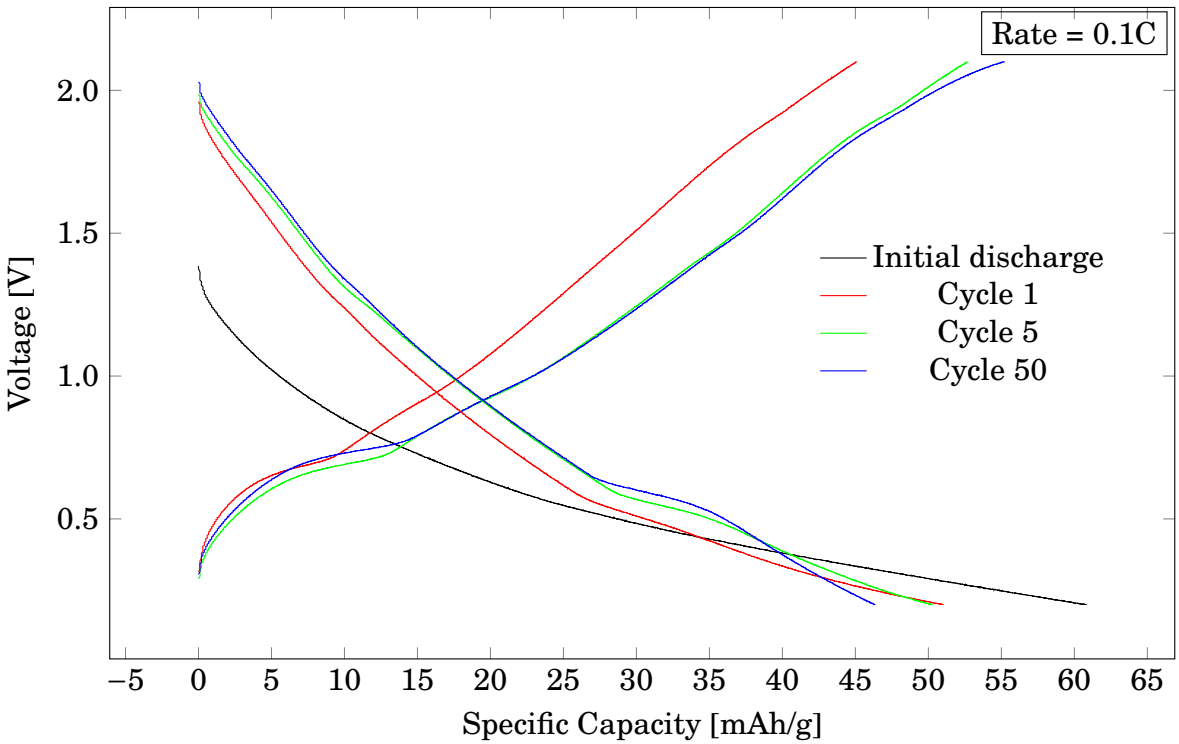

Figure 4.5: Charge-discharge curves for the best performing cathode of untreated Mn_3O_4 cycled 50 times between 0.2 and 2.1 V. Active mass was 1.36 mg and average specific capacity was 50 $mAh\,g^{-1}$. The black line illustrates the initial discharge, the red lines are cycle 1, charge upwards and discharge downwards, the green lines are cycle 5 and the blue lines are cycle 50.

between the initial discharge and cycle 1 is clearly seen. The remaining cycling shows capacities in the same area as cycle 1. More specifically the capacity values for the initial, first, fifth and fiftieth discharge are 38, 25, 24 and 24 $mAh\,g^{-1}$. The charging show an increase in capacity with cycling number, the exact values for 1st, 5th and 50th charge being 21, 23 and 24 $mAh\,g^{-1}$. For this cathode, a charge plateau can be seen for all three cycles shown, and a downwards shift in the plateau with cycling is observed. In the discharge curves on the other hand, only cycle 50 show a proper plateau while cycle 1 and 5 only have a bend in the curves. The plateaus are more narrow and less obvious in these curves compared to the ones for the best performing cathode. Actually, when looking at all the charge-discharge curves for the cathodes of not milled Mn_3O_4, both the two in this section and the seven in Appendix A.1, some overall trends can be seen. These are that with decreasing specific capacity, or increasing active mass, the steeper the curves are and the smaller the plateaus become. In addition, the discharge plateau of cycle 5 looses more and more of it's horizontal degree with decreasing capacity.

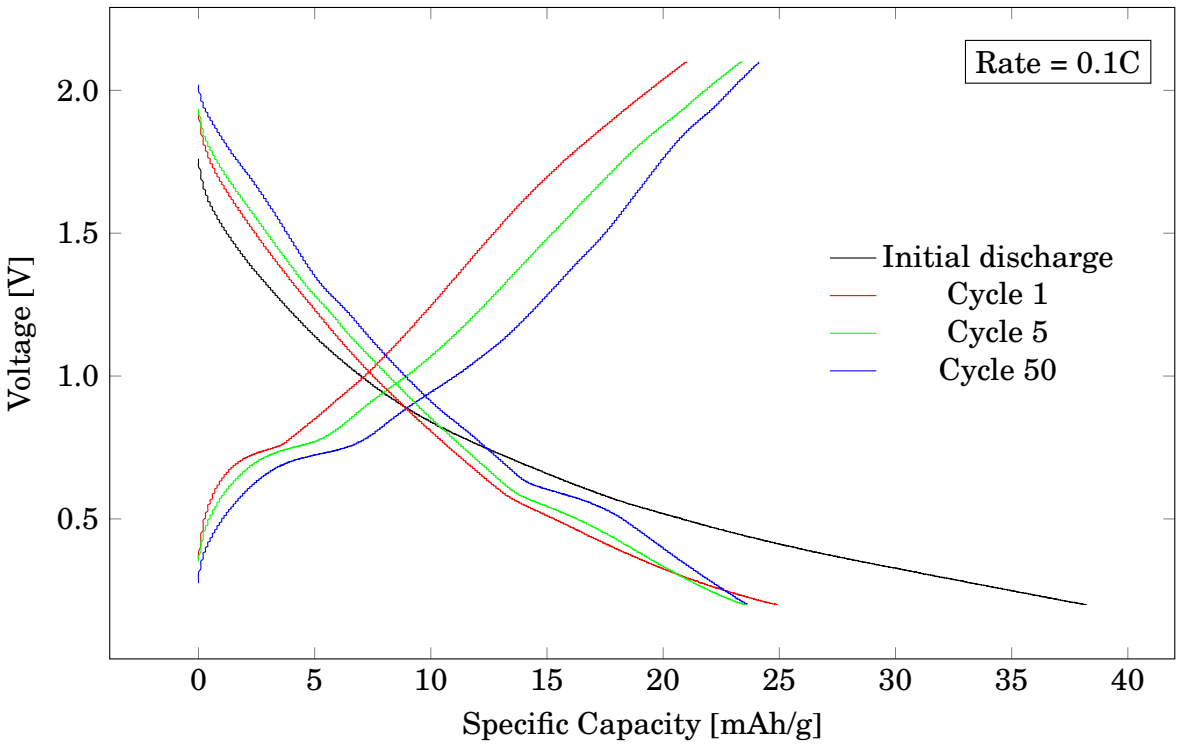

Figure 4.6: Charge-discharge curves for the poorest performing cathode of untreated Mn_3O_4 cycled 50 times between 0.2 and 2.1 V. Active mass was 2.72 mg and the average specific capacity was 24 $mAhg^{-1}$. The black line illustrates the initial discharge, the red lines are cycle 1, the green lines are cycle 5 and the blue lines are cycle 50.

In order to compare the obtained capacities of these two different cathodes more thoroughly, their capacity development during the fifty cycles are plotted in the same diagram in Figure 4.7. There is an obvious difference in capacity between the best cathode, the two upper curves, and the poorest cathode, the two lower curves. However, there is a larger difference in charge and discharge capacities for the best performing cathode than for the poorest cathode. Also, while the difference between charge and discharge capacity for the best performing cathode grows larger during cycling, the charge and discharge capacities for the poorest performing cathode is almost equal throughout the cycling.

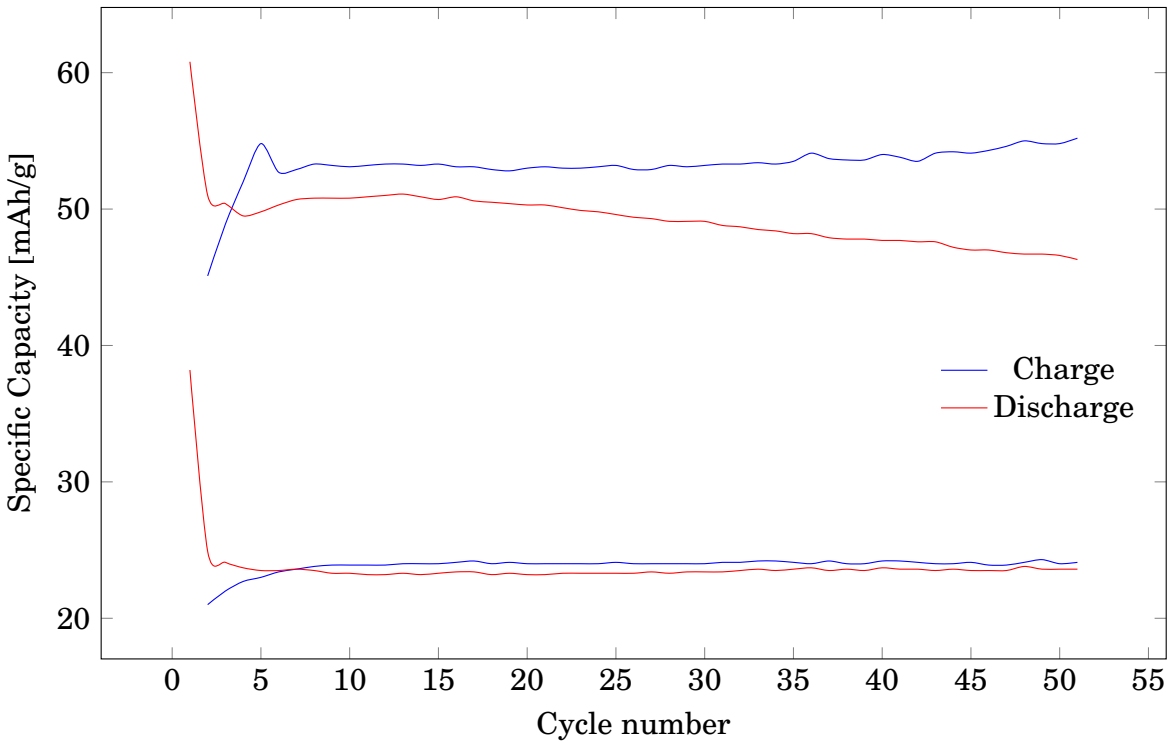

Figure 4.7: Comparison between the best performing cathode with average capacity of 50 $mAhg^{-1}$ and the poorest performing cathode with average capacity of 24 $mAhg^{-1}$ after charge-discharge cycling 50 times. The two upper lines represent charge (blue) and discharge (red) for the best performing cathode, while the two bottom lines represent the poorest performing cathode. The active mass of the cathodes are respectively 1.36 and 2.72 mg.

Milled Mn_3O_4

Eight cathodes of milled Mn_3O_4 have been tested in this work. The cathodes achieving the highest and lowest capacity are shown with charge-discharge curves in this section, while the six other cathodes are given in Appendix A.2. Starting with the best performing cathode, this one is presented in Figure 4.8. The active mass of this cathode was 1.04 mg and the average specific capacity during 50 cycles was 65 $mAhg^{-1}$.

When looking at the discharge curves there are some evident trends. First, the endpoint capacity decreases with increasing number of cycles. The discharge capacities for the initial, first, fifth and fiftieth cycle are respectively 85, 67, 65 and 63 $mAhg^{-1}$. Also, the discharge plateau is shifted to higher voltages with increasing number of cycles. The discharge curve of cycle 1 appears to almost have a plateau because the slope of the curve seems to change twice in the area where cycle 5 and 50 have a plateau. For the charge curves, all cycles have a plateau, and cycle 5 and 50 have plateaus at the exact same voltage. At the endpoint of the charge lines, it can be seen that the capacity increases from cycle 1 to 5 and then decreases

for cycle 50. The respective capacity values are 66, 71 and 65 $mAhg^{-1}$.

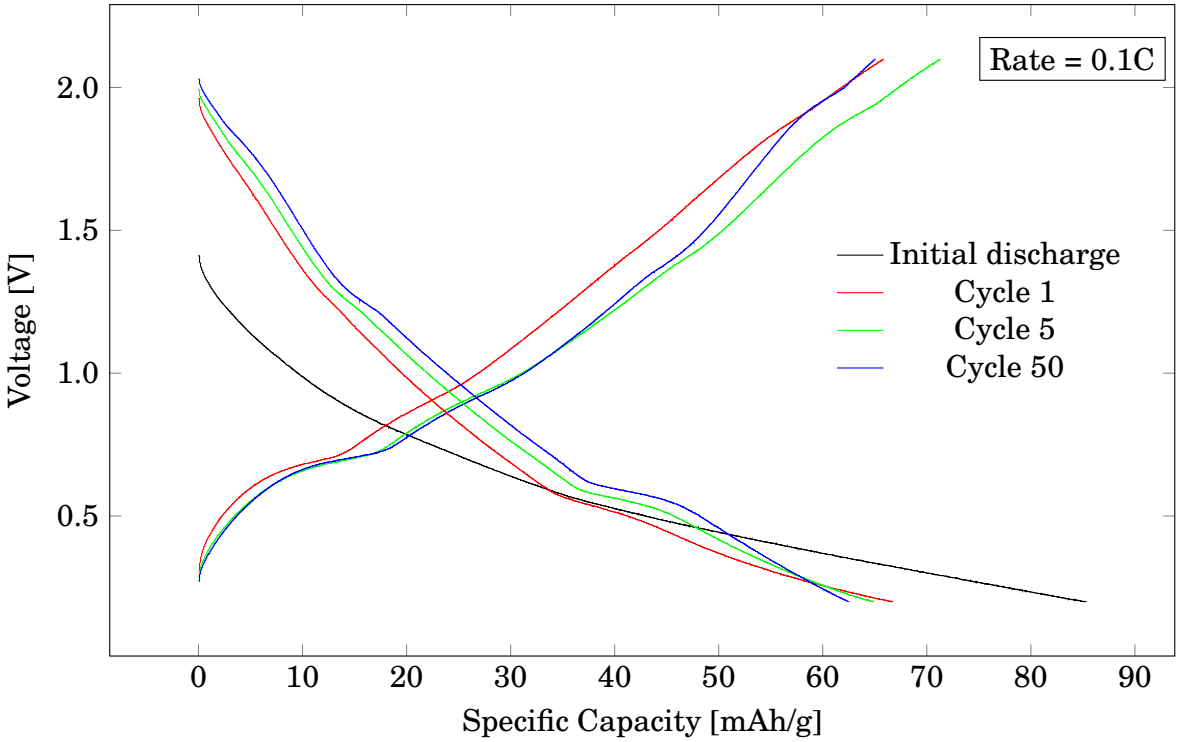

Figure 4.8: Charge-discharge curves for the best performing cathode of milled Mn_3O_4. Active mass was 1.04 mg and the average specific capacity was 65 $mAhg^{-1}$.

The cathode of milled Mn_3O_4 showing the lowest capacity is illustrated in Figure 4.9. This cathode had an active mass of 2.0 mg and an average specific capacity of 33 $mAhg^{-1}$. Compared to Figure 4.8 some, but not all, of the same trends are found here. For the discharge endpoint values, there is an obvious decrease from the initial discharge to the rest, before the capacity stabilizes at 32 - 33 $mAhg^{-1}$. The respective values for the initial, first, fifth and fiftieth discharge are 45, 33, 32 and 33 $mAhg^{-1}$. Compared to the best cathode of milled Mn_3O_4, here the curves for cycle 5 seem to be following the curves for cycle 1 more than those for cycle 50. All the cycles have a charge plateau, however the discharge plateau for cycle 1 looks to only be a bend in the curve. Cycle 5 and 50 are seen to have discharge plateaus. Also, while the discharge plateau shows an upwards shift in voltage with cycling, the charge plateau has a downwards shift. With regard to the charge curves' endpoints, there is not the same decrease in the capacity from cycle 5 to 50 like in Figure 4.8. The capacity values for the first, fifth and fiftieth charge are respectively 31, 35 and 34 $mAhg^{-1}$.

Compared to the cathodes of not milled Mn_3O_4, the cathodes of milled Mn_3O_4 had a nar-

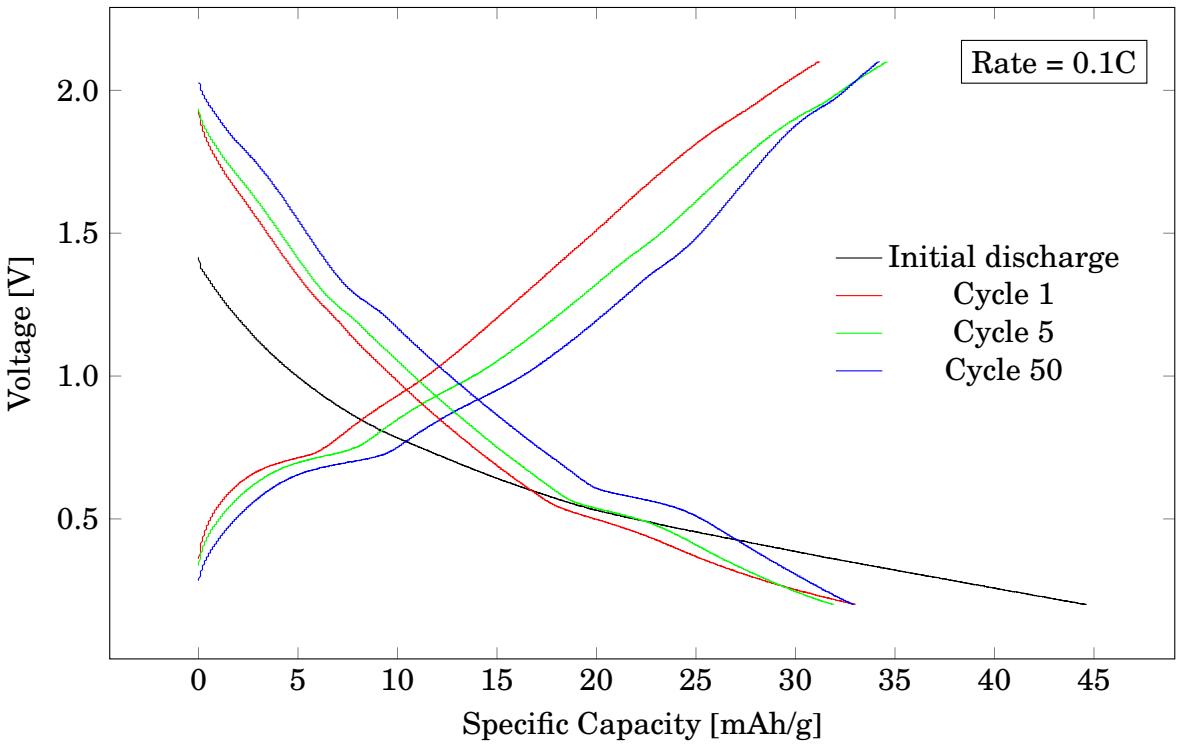

Figure 4.9: Charge-discharge curves for the poorest performing cathode of milled Mn_3O_4. Active mass was 2.0 mg and average specific capacity was 33 $mAh\,g^{-1}$.

rower active mass range and a wider capacity range. When studying all the charge-discharge curves for cathodes of milled Mn_3O_4, i.e. the two here and the six in Appendix A.2, some differences are seen compared to the cathodes of not milled Mn_3O_4. First of all there is not a large difference in how steep the curves are with decreasing capacity. Also, there is no obvious change in the size of the plateaus. The discharge plateau of cycle 5 though, shows a slight tendency of looking more like cycle 1 than 50 with decreasing capacity.

In Figure 4.10 development of the capacity output during the 50 cycles for the best and poorest cathode are presented in the same plot. The two upper lines, blue (charge) and red (discharge) represent the best cathode which had an average specific capacity of 65 $mAh\,g^{-1}$. The two bottom lines represent the poorest cathode with average specific capacity of 33 $mAh\,g^{-1}$. The difference in active mass between the cathodes is 0.96 mg. It can be seen that the lines for the poorest cathode are closer together and more straight than those for the best cathode. This meaning that the charge and discharge capacities are more equal and that the performance is more stable for the poorest cathode. Though there are not large variations for the best cathode either.

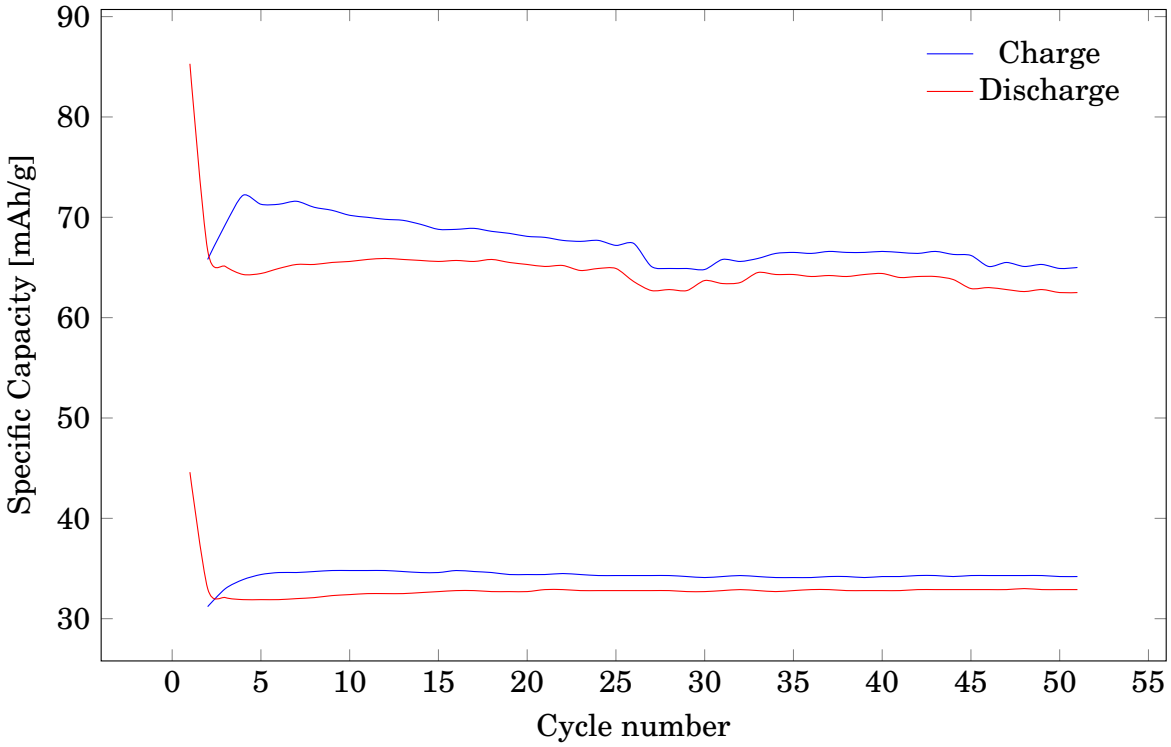

Figure 4.10: Comparison of capacity output for the two cathodes during the 50 cycles. For the best and poorest cathode, average capacity was respectively 65 and 33 $mAh\,g^{-1}$. Active mass of the two were 1.04 and 2.0 mg.

Not milled Mn_3O_4 mixed with RGO

Seven cathodes of not milled Mn_3O_4 with RGO will be presented in this section and the appendix. From these, two were tested during this work, while five were tested and presented in earlier work [1]. The reason these five cathodes are presented again is that some modifications have been made to their data. The cathodes were made from a powder consisting of 85 wt% Mn_3O_4 and 15 wt% graphene oxide. This was not accounted for in the earlier work. The active mass was given as the amount of powder on the cathodes instead of only the amount of Mn_3O_4. In this work on the other hand, the active mass is defined as the loading of Mn_3O_4 on the cathodes. Hence, data on the five cathodes from earlier work have been recalculated according to this active mass. In this section, the cathode with the highest and the cathode with the lowest capacity will be shown with charge-discharge curves, while the others can be found in Appendix A.3.

The best performing cathode of this type is the best from earlier work, modified with new specific capacity and active mass. The charge-discharge curves for this cathode is shown in Figure 4.11. After calculations the new active mass was found to be 1.09 mg and the average specific capacity was 78 $mAh\,g^{-1}$.

Looking at the curve endpoints, there is an increase in the capacity for the charge curves with cycling. The values obtained for the first, fifth and fiftieth charge are respectively 72, 79 and 81 $mAhg^{-1}$. For the discharge curves there is a decrease from the initial to cycle 5, and then an increase for cycle 50. The values are respectively 103, 78, 76 and 79 $mAhg^{-1}$. When it comes to the discharge plateau, there is a clear shift towards higher voltage with increasing number of cycles. All cycles show both a charge and a discharge plateau. For the charge plateau there is a slight downwards shift in the plateau, while the discharge plateau has an upwards shift.

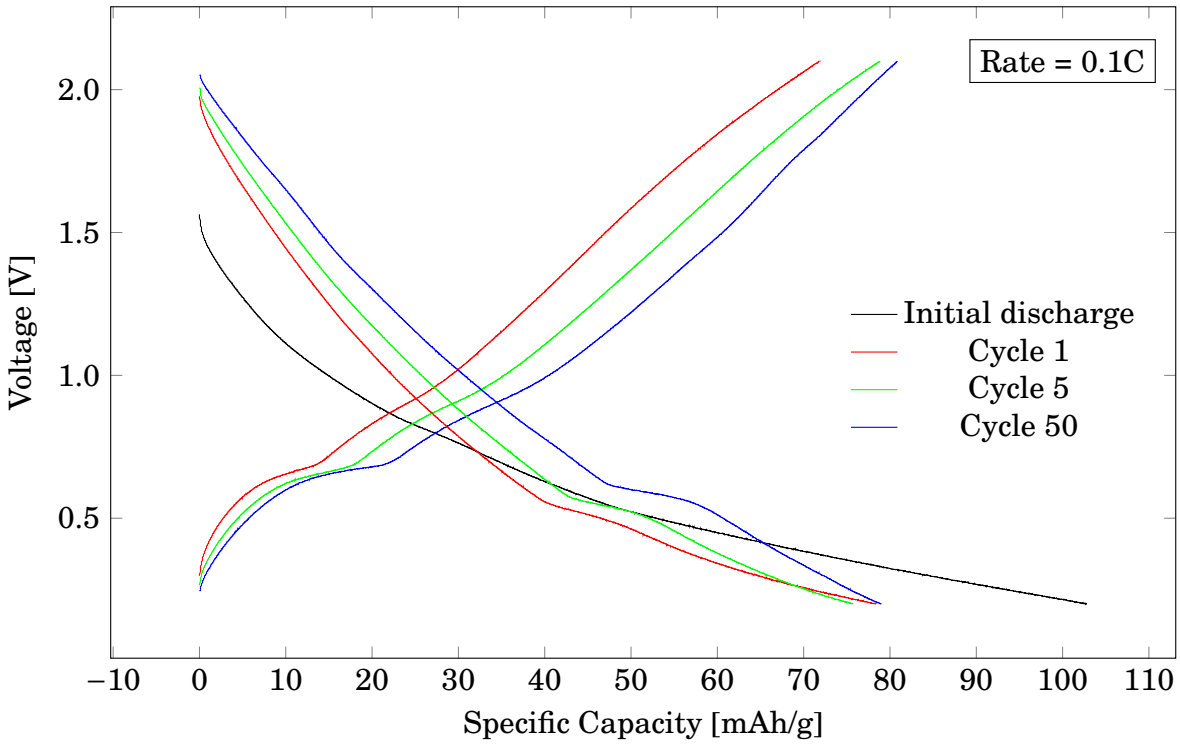

Figure 4.11: Charge-discharge curves for the best performing cathode of not milled Mn_3O_4 with RGO. The average specific capacity was 78 $mAhg^{-1}$ and the active mass was 1.09 mg. Modified from [1].

The poorest performing cathode of not milled Mn_3O_4 with RGO is shown with charge-discharge curves in Figure 4.12. The average specific capacity was 32 $mAhg^{-1}$ and the active mass was 2.18 mg. It can be seen that the discharge values for cycle 1 to 50 are all the same, i.e. 31 $mAhg^{-1}$. The initial discharge capacity was 44 $mAhg^{-1}$. The charge values differ more from one another and increase with increasing cycling number. The capacities for the first, fifth and fiftieth charge are respectively 25, 32 and 33 $mAhg^{-1}$. For the charge curves, all the cycles show a plateau, though the one for cycle 1 is very small. For

the discharge curves, cycle 50 have a small plateau while cycle 1 does not show any sign of a plateau and cycle 5 only has a bend in the curve. For the charge plateau, there is a shift and widening in the x-direction occurring during cycling.

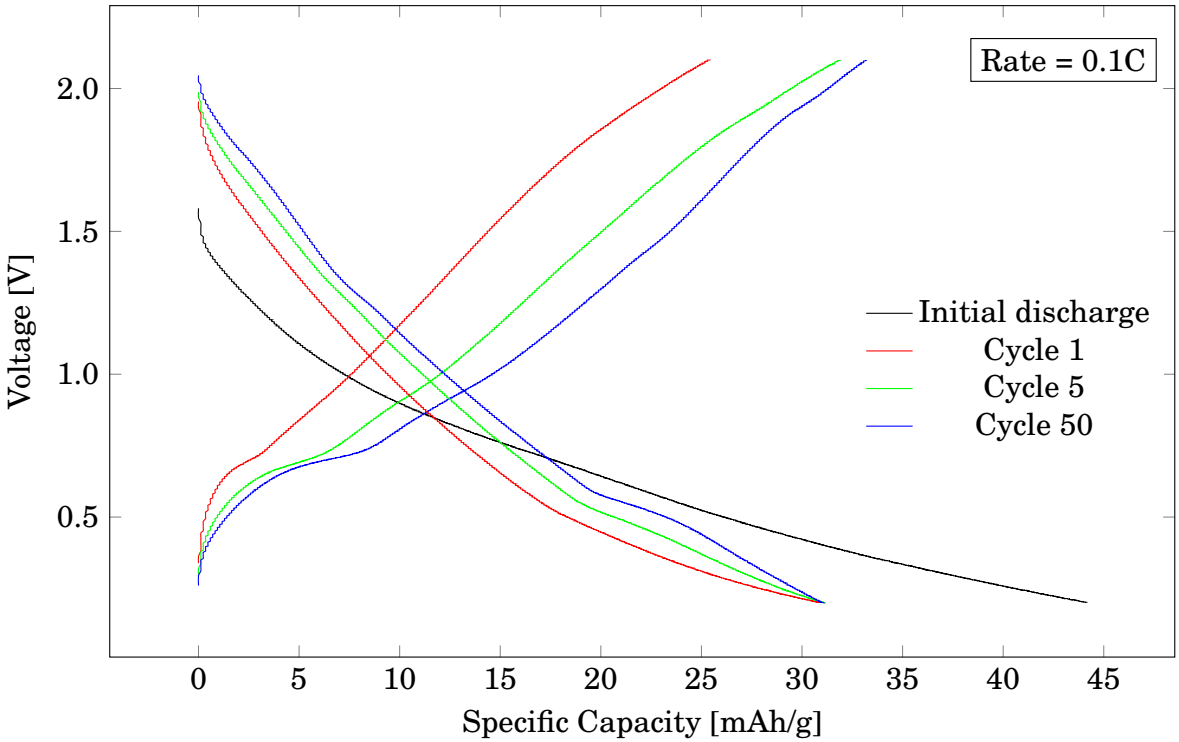

Figure 4.12: Charge-discharge curves of the poorest performing cathode of not milled Mn_3O_4 with RGO. The average specific capacity was 32 $mAh\,g^{-1}$ and the active mass was 2.18 mg.

Comparing all the curves obtained for the cathodes of not milled Mn_3O_4 with RGO, i.e. the two here and the five in Appendix A.3, a trend is seen. With increasing active mass, the discharge plateaus become less of a plateau and more just bend in the curves. Opposite to the cathodes of pure, not milled Mn_3O_4, there does not seem to be a continuous increase in how steep the curves are with decreasing capacity. Also there is no particularly change in the charge plateau.

The development of the capacity during the 50 cycles for the best and poorest performing cathode of not milled Mn_3O_4 with RGO is plotted in Figure 4.13 for comparison. The two upper lines, blue (charge) and red (discharge) represent the best cathode with an average specific capacity of 78 $mAh\,g^{-1}$. The two lower lines are for the poorest cathode with an average specific capacity of 32 $mAh\,g^{-1}$. The difference in capacity is thus 46 $mAh\,g^{-1}$, while the difference in active mass between the two is 1.09 mg. It can be seen that the poorest cathode has more stable capacity throughout the 50 cycles, though it should be noted that there

are only small changes in the capacity for the best cathode as well. Both cathodes have discharge values quite similar to the charge values and the charge values are constantly slightly larger than the discharge.

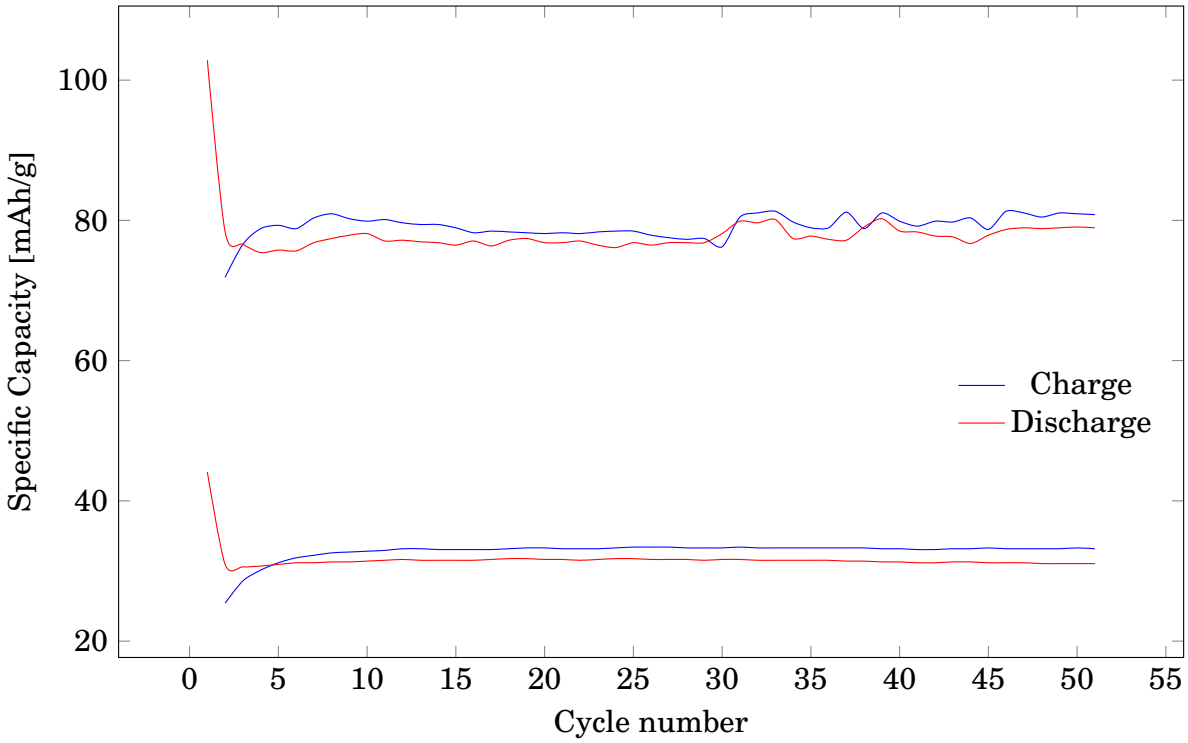

Figure 4.13: Comparison between the best and poorest cathode of not milled Mn_3O_4 with RGO. The best cathode had an average specific capacity of 78 $mAhg^{-1}$ and active mass of 1.09 mg, while the poorest cathode had an average capacity of 32 $mAhg^{-1}$ and active mass of 2.18 mg.

Milled Mn_3O_4 mixed with RGO

The best performing cathode of milled Mn_3O_4 with RGO is given with charge-discharge curves in Figure 4.14. The average specific capacity achieved for this cathode was 60 $mAhg^{-1}$. The cathode's active mass was 1.09 mg. The curves show that except from the initial discharge, the charge and discharge reach capacity values closely spaced. The respective values for initial, 1st, 5th and 50th discharge are 80, 62, 60 and 58 $mAhg^{-1}$. The charge values from 1st to 50th cycle are 55, 61 and 58 $mAhg^{-1}$. The discharge plateau shows an upwards shift in voltage during cycling, while the charge plateau has a slight downwards shift.

The poorest performing cathode of milled Mn_3O_4 with RGO is given with charge-discharge

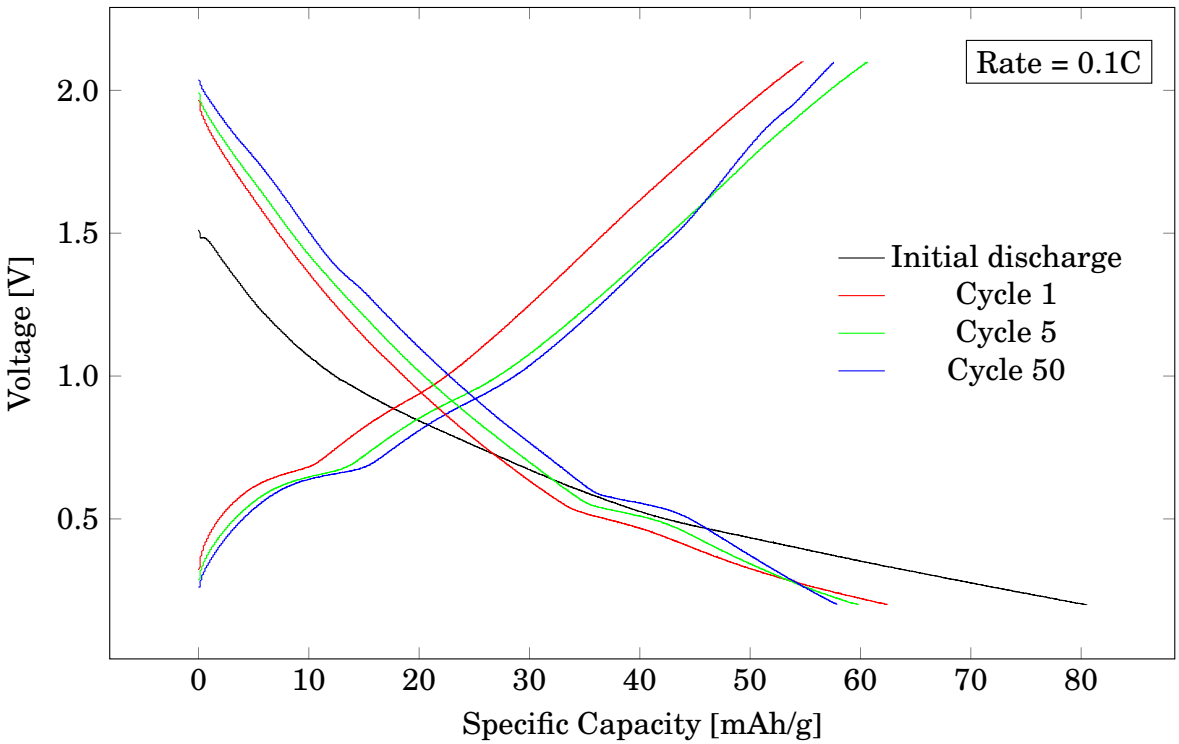

Figure 4.14: Charge-discharge curves for the best performing cathode of milled Mn_3O_4 with RGO. Active mass was 1.09 mg and the average specific capacity was 60 $mAh\,g^{-1}$.

curves in Figure 4.15. The average specific capacity obtained was 26 $mAh\,g^{-1}$ and the active mass of the cathode was 2.58 mg. The capacity values for the initial discharge and the discharge of cycle 1, 5 and 50 are respectively 40, 27, 25 and 26 $mAh\,g^{-1}$. The charge values for cycle 1, 5 and 50 are 26, 31 and 27 $mAh\,g^{-1}$. Just like the poorest cathode of not milled Mn_3O_4 with RGO, the cathode shown here had small charge plateaus, especially cycle 1. Also, only cycle 50 has a discharge plateau, while cycle 1 and 5 just have a small bend in their curves.

Comparing all the cathodes of milled Mn_3O_4 with RGO, hence the two given here and the six presented in Appendix A.4, it can be seen that the charge plateau become smaller with decreasing capacity. Also, cycle 1 and 5 gradually loose their discharge plateau with decreasing capacity.

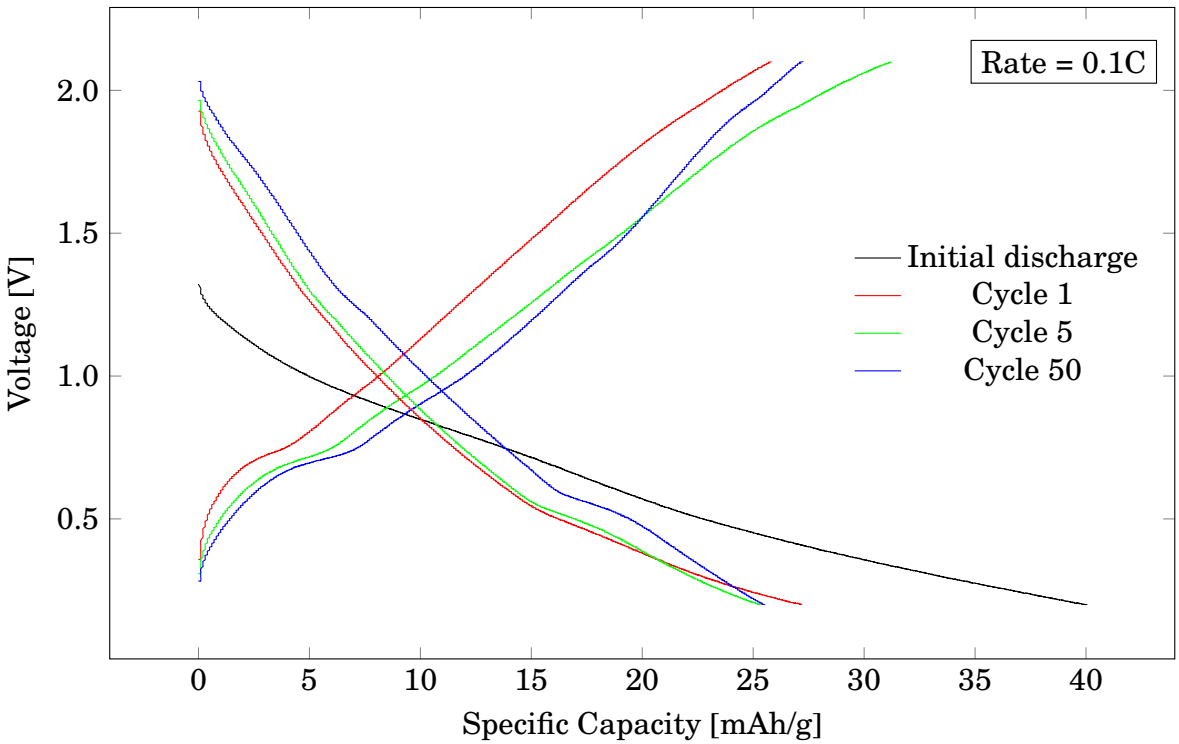

Figure 4.15: Charge-discharge curves for the poorest performing cathode of milled Mn_3O_4 with RGO. Active mass was 2.58 mg and average specific capacity was 26 $mAh\,g^{-1}$.

To compare the performance more thoroughly, the capacity development during the cycling for the two cathodes is plotted in Figure 4.16. The two cathodes have average capacities separated by 34 $mAh\,g^{-1}$, while their active masses differ by 1.49 mg. It can be seen that both cathodes have a very stable capacity throughout the cycling.

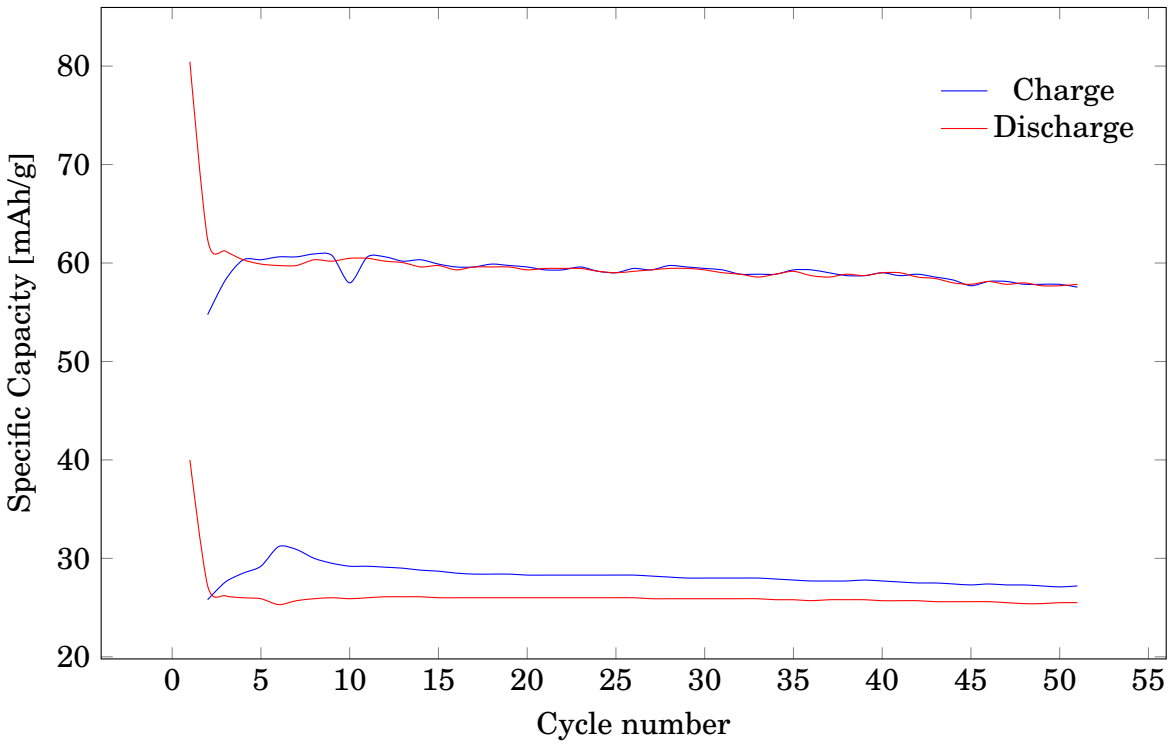

Figure 4.16: Comparison of the performance of the best and poorest cathode of milled Mn_3O_4 with RGO during the 50 cycles. The best cathode had an average specific capacity of 60 $mAh\,g^{-1}$ and active mass of 1.09 mg, while the poorest cathode had an average capacity of 26 $mAh\,g^{-1}$ and active mass of 2.58 mg.

4.2.2 Long term performance

Four batteries with different cathodes were long term cycled at 0.1C. The cycling time was found to be different for each cathode, and to increase with decreasing active mass. Hence, the cathodes did not all reach the same number of cycles in the given time. The goal was 500 cycles, but only the two cathodes with the fastest cycling reached this. The other two cathodes were stopped after 400 and 300 cycles. The cathode that reached 400 cycles did so in 83 days and had an active mass of 1.56 mg. The cathode stopped after 300 cycles had been cycling for 88 days and had an active mass of 1.12 mg. The two cathodes reaching 500 cycles are presented below, while the other two are given in Appendix B.

The first cathode to reach 500 cycles was made of milled Mn_3O_4 with RGO. The active mass of this cathode was 1.56 mg. One charge or discharge took approximately 1 hour and 50 min. This corresponds to a total cycling time of about 1832 hours or 76 days. This cathode is presented in Figure 4.17 with charge-discharge curves of cycle 1, 5, 50, 100, 200, 300, 400 and 500. The average capacity achieved for this cathode was 42 $mAh\,g^{-1}$, and both plateaus can clearly be seen. The charging plateau has a downwards shift from cycle 1 to 50, and then

shifts upwards again to voltages higher than where the cycle 1 plateau is. The discharge plateau has an upwards shift to higher voltages with increasing number of cycles. Just like the cathode cycled 50 times, it can be seen that cycle 1 does not have a discharge plateau.

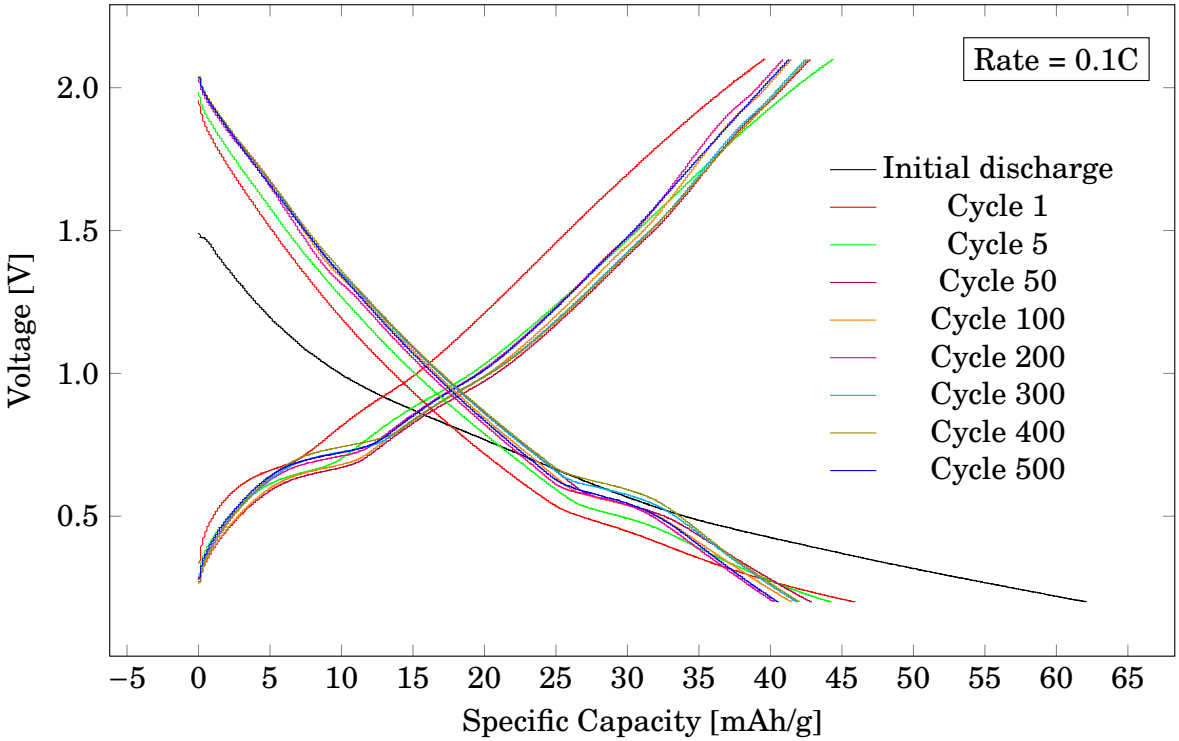

Figure 4.17: Charge-discharge curves for the cathode of milled Mn_3O_4 with RGO enduring 500 cycles. Active mass was 1.56 mg and average specific capacity during the 500 cycles was 42 $mAh\,g^{-1}$.

Focusing on the obtained capacities during the 500 cycles, the development is shown in Figure 4.18. The blue x marks represent charge capacities and red o marks represent discharge capacities, corresponding to the left y-axis. The black dots illustrates the efficiency and corresponds to the right y-axis. The efficiency is here seen to be very good, the average being 99 %. The capacity is also very stable throughout the entire cycling, showing no sign of failure.

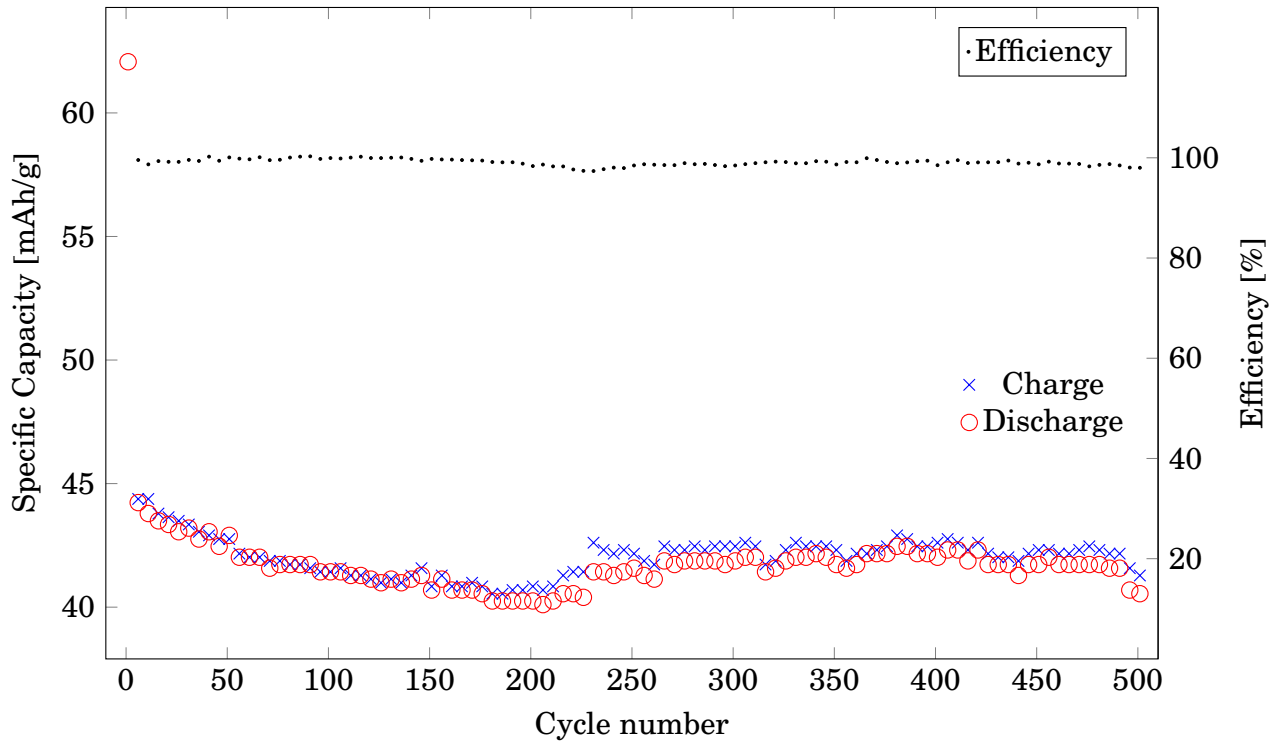

Figure 4.18: Charge and discharge capacities achieved for the cathode of milled Mn_3O_4 with RGO during the 500 cycles. Active mass is 1.56 mg and average specific capacity during the 500 cycles was 42 $mAh\,g^{-1}$.

The second battery to reach 500 cycles had a cathode of not milled Mn_3O_4 with RGO. The active mass of the cathode was 1.84 mg and the average capacity achieved during the cycling was 37 $mAh\,g^{-1}$. Charge-discharge curves of cycle 1, 5, 50, 100, 200, 300, 400 and 500 for this cathode are presented in Figure 4.19. Each charge or discharge took approximately 2 hours for this cathode. This corresponds to a total cycling time of 2002 hours or 83 days. From the curves in Figure 4.19, it can be seen that cycle 1 is different from the rest of the cycles, which are very similar to one another. The first difference is that the charge plateau of cycle 1 is seen to be further to the left than the plateau for the other cycles. In addition, the discharge curve of cycle 1 is the only one without a clear plateau. There is merely a bend in the curve, indicating a reaction. Looking at the plateaus, there are clearly a voltage shift with cycling. For the charge plateau, cycle 50 has the plateau with the lowest voltage while cycle 300 has the plateau with the highest voltage. For the discharge plateau, cycle 400 has the plateau at the highest voltage.

Development of the capacity during the cycling is shown in Figure 4.20. From the figure it can be seen that the capacity had a slow and steady decrease to cycle 200, before it had a small jump and stayed relatively flat throughout the remaining cycling. The charge and

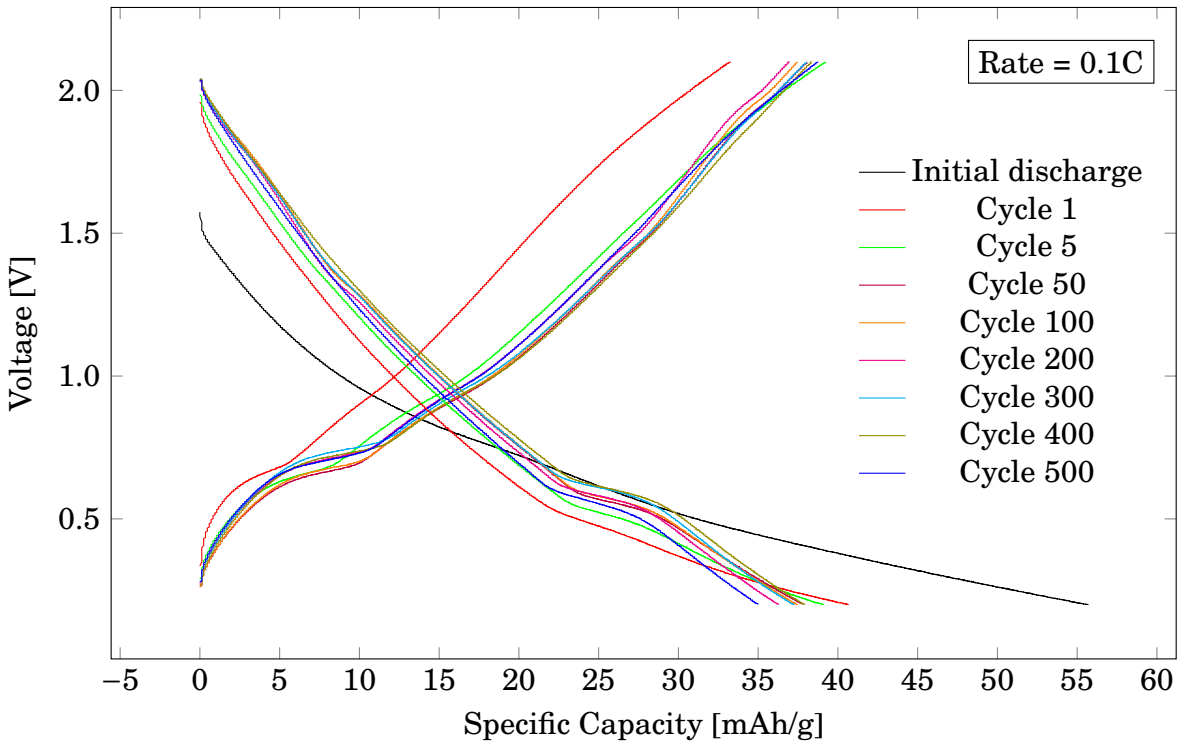

Figure 4.19: Charge-discharge curves for the cathode of not milled Mn_3O_4 with RGO cycled 500 times. Active mass was 1.84 mg and average specific capacity during the 500 cycles was 37 $mAh\,g^{-1}$.

discharge capacities managed to follow each other quite well, so the overall efficiency was good. The average efficiency during the cycling was 98 %.

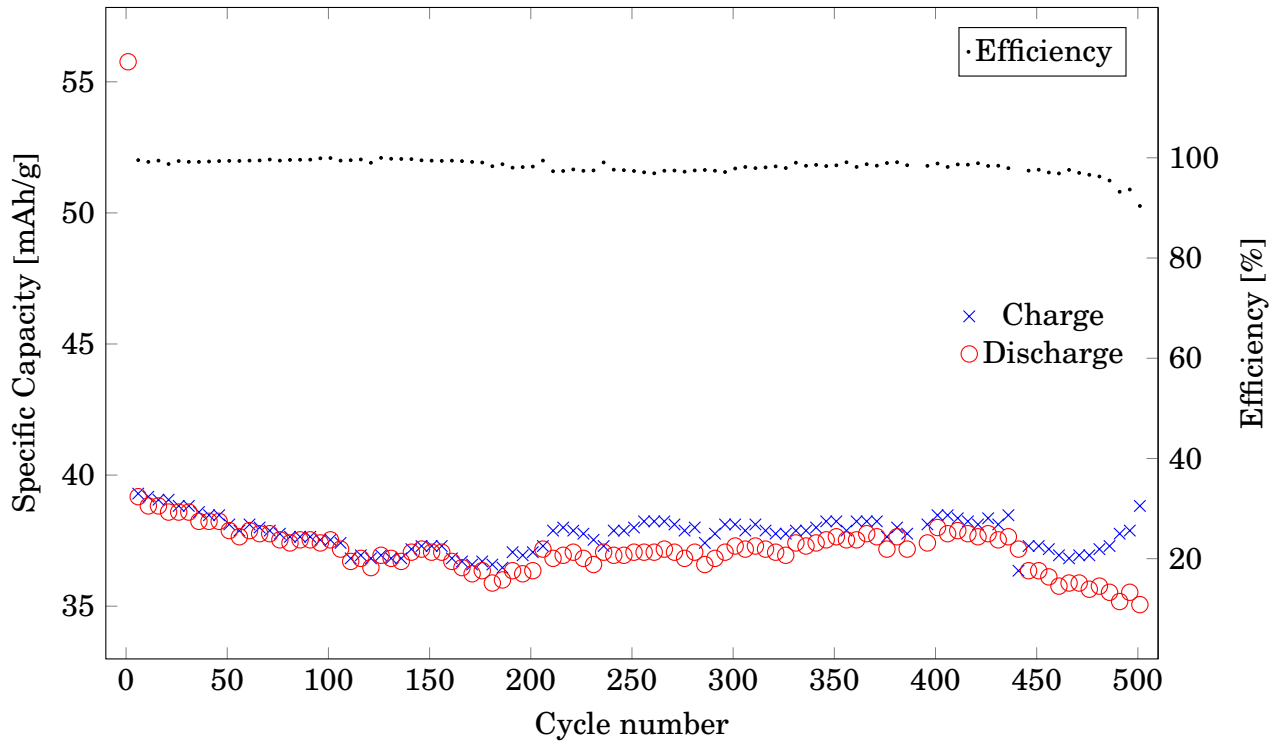

Figure 4.20: Charge and discharge capacities achieved for the cathode of not milled Mn_3O_4 with RGO during the 500 cycles. Active mass was 1.84 mg and average specific capacity during the 500 cycles was 37 $mAh\,g^{-1}$.

4.2.3 Capacity dependency on active mass

Resulting capacity of all the batteries cycled 50 times at 0.1C is shown in Figure 4.21. All the values are also presented in Table 4.1. The red dots represent cathodes of not milled Mn_3O_4 with RGO, and the green dots represent cathodes of milled Mn_3O_4 with RGO. In Figure 4.21 it can be seen that these two generally are positioned slightly above the blue and orange dots. The blue and orange dots corresponds respectively to pure, milled and not milled Mn_3O_4. This means that the cathodes with RGO generally achieved a higher specific capacity per gram Mn_3O_4. From the plot it looks like there are no distinct difference in performance between milled and not. The cathodes of pure Mn_3O_4, milled and not, seem to follow one common trend, while the cathodes with RGO follows a slightly different trend. Thus mixing Mn_3O_4 with RGO was a more effective method to increase the capacity than milling the powder. From Figure 4.21 and Table 4.1 it is found that the highest capacity was obtained by a cathode of not milled Mn_3O_4 with RGO, having an active mass of 1.09 mg. Other cathodes with active mass in the same area, and even lower, are also presented. However, these showed capacities more than 10 $mAh\,g^{-1}$ lower than the best.

Disregarding the different colors of the dots in Figure 4.21, there is an obvious trend in-

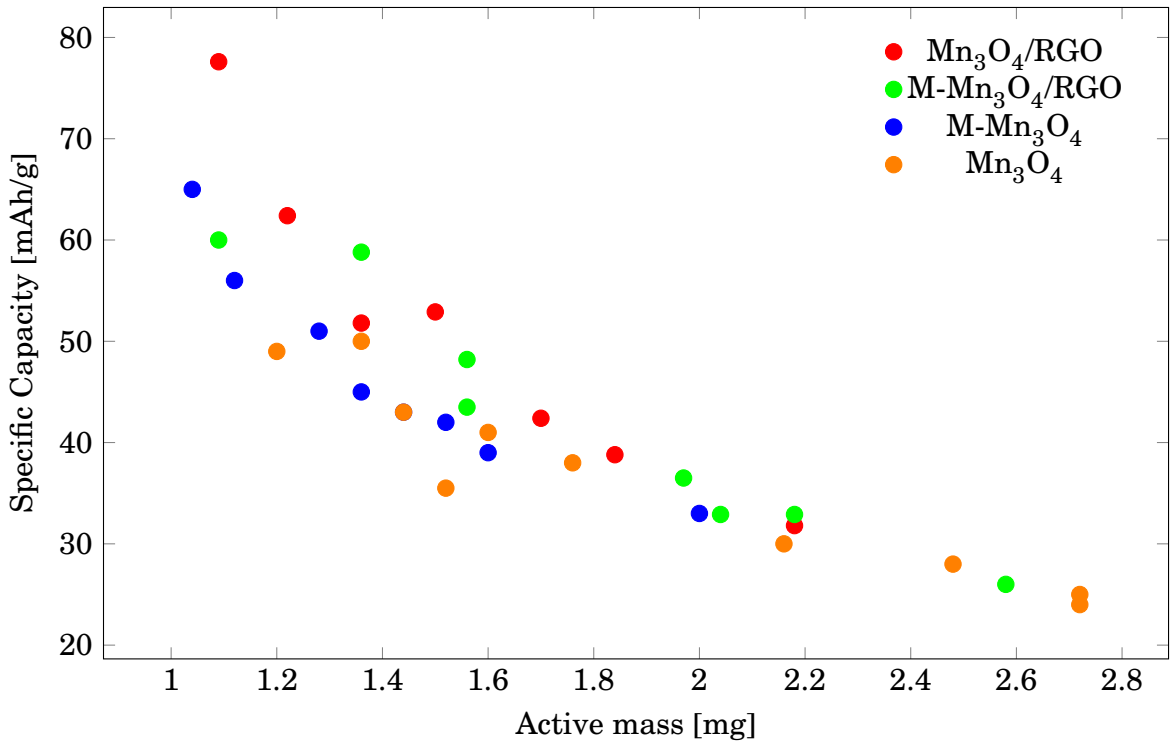

Figure 4.21: Summary of the resulting capacities obtained with the four different types of cathode plotted against amount of active mass on each. The red dots are for cathodes of not milled Mn_3O_4 with RGO, green are milled Mn_3O_4 with RGO, blue are pure, milled Mn_3O_4 and orange are pure, untreated Mn_3O_4.

dicating that the amount of active material on the cathodes affects the resulting capacity. The lower the active mass on the cathodes, the higher the resulting specific capacity is. The capacity achieved for each type of cathode is always highest for the cathode with the lowest active mass. The only exception is the cathodes of pure, not milled Mn_3O_4, where the cathode with the second lowest active mass had the highest capacity. Though it can be noted that only 1 $mAh\,g^{-1}$ separated the two cathodes and the difference in mass was 0.16 mg. Capacity is given as the average discharge capacity of the cathodes during the 50 cycles.

Not milled Mn_3O_4		Milled Mn_3O_4		Not milled Mn_3O_4 + RGO		Milled Mn_3O_4 + RGO	
Active mass [mg]	Specific capacity [mAh/g]	Active mass [mg]	Specific capacity [mAh/g]	Active mass [mg]	Specific capacity [mAh/g]	Active mass [mg]	Specific capacity [mAh/g]
1.2	49	1.04	65	1.09	78	1.09	60
1.36	50	1.12	56	1.22	62	1.36	59
1.44	43	1.28	51	1.36	52	1.56	48
1.52	36	1.36	45	1.5	53	1.56	44
1.6	41	1.44	43	1.7	42	1.97	37
1.76	38	1.52	42	1.84	39	2.04	33
2.16	30	1.6	39	2.18	32	2.18	33
2.48	28	2.0	33			2.58	26
2.72	25						
2.72	24						

Table 4.1: Table of the average specific capacities obtained by the cathodes cycled 50 times at 0.1C and their active masses.

4.2.4 Rate dependency

In order to see how the battery performance varied with charge/discharge rate, two new programs were run. The first one was rate capability, which was tested on five cathodes in total. Two cathodes of pure, milled Mn_3O_4 and three cathodes of milled Mn_3O_4 with RGO. All the cathodes were cycled according to the rate capability program given in the experimental section. Hence the batteries were cycled five times at each of the following current rates; 0.05C, 0.1C, 0.2C, 0.5C, 1C, 2C and 5C. After the 5C cycles, the rate was shifted back to 0.05C to see if the capacity would return to the initial value again. 1C is the current rate needed to discharge or charge the battery in one hour. From the five cathodes tested, two will be presented here while the others are given in Appendix C. Hence, the cathode of each type, cycling with the highest capacity are given below.

The second program was simply cycling at the lowest possible rate. For the Lanhe machine this was 0.02C. The cathode cycled at this rate was intended for ex situ study, but one of these are presented with charge-discharge curves in the section labeled effect of slow rate below.

Rate capability

The cathode of pure, milled Mn_3O_4 showing the highest capacity during the rate capability test is presented in Figure 4.22. The figure shows the charge (blue) and discharge (red) capacities obtained during cycling at the different rates. It can be seen that the specific capacity of the cathode decreases gradually with increasing current rate from 0.05C to 5C. The decrease is subtle from 0.05C to 0.5C, and then more and more evident down to 5C. It

should be noted that when the current rate is reduced to lower values (0.05C) again, the specific capacity of the cathode increases back to the initial values. On the right hand side of the figure, the coulombic efficiency is plotted. It can be seen that the efficiency is quite stable throughout the test, at values between 80 and 100 %.

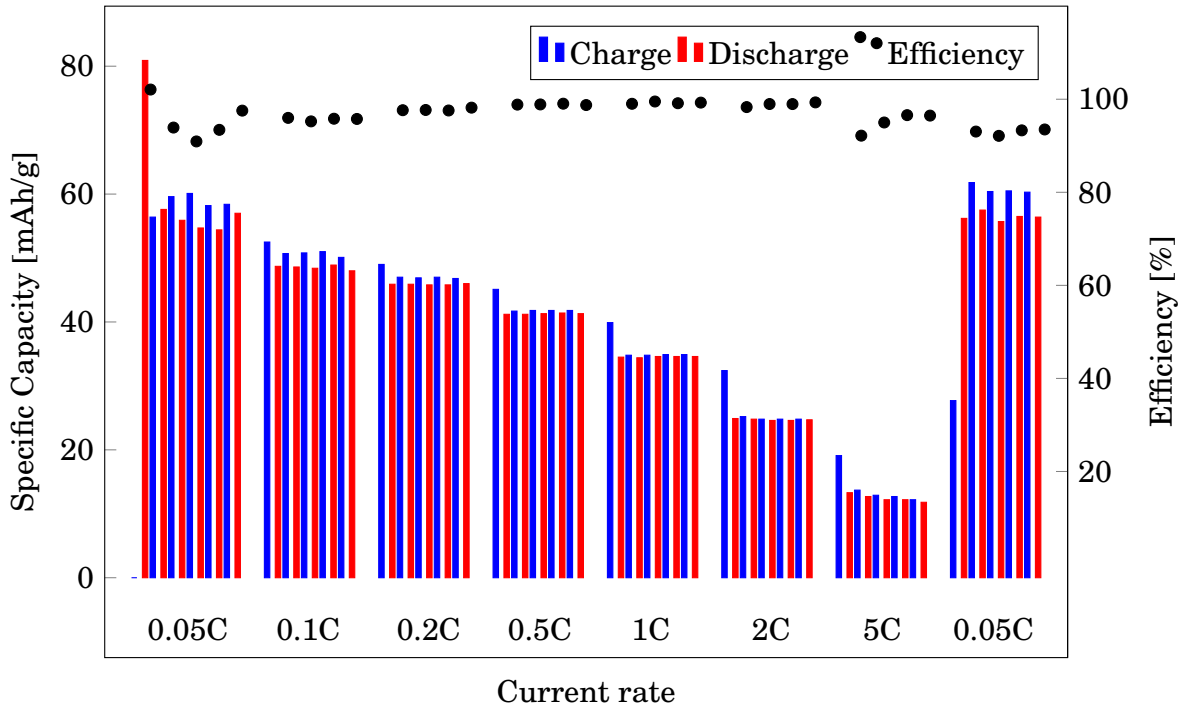

Figure 4.22: Rate capability of cathode of milled Mn_3O_4 showing how the specific capacity changes with current rate from 0.05C to 5C. The blue bars indicate charging values, the red bars indicate discharging values and the black dots show the efficiency. The cathode was cycled five times at each rate. The first group has six red bars due to the initial discharge, which do not count as a cycle. Active mass of the cathode is 1.44 mg.

Studying the charge and discharge bars in the plot, it can be seen that the first charge bar of each group always differ from the rest in that it is much closer in value to the bars of the previous group. Also, the charge capacities are generally higher than the discharge capacities. This is most clearly seen for the first and last bar group, i.e. where the rate is 0.05C. The higher the rate becomes, the smaller the difference between charge and discharge is. The average discharge capacity of each group from left to right are 56, 49, 46, 41, 35, 25, 12 and 57 $\mathrm{mAh\,g^{-1}}$. Here the initial discharge is not part of the first group. The average charge values for each group from left to right are 59, 51, 47, 42, 35, 25, 13 and 61 $\mathrm{mAh\,g^{-1}}$. These values do not include the first charge of each group since those differ so much from the rest. From the numbers it is found that the charge capacity actually ends up

with higher values the second time the rate is 0.05C compared to the first.

Rate capability test on the cathode of milled Mn_3O_4 with RGO showning the highest capacity is shown in Figure 4.23. This figure looks quite similar to Figure 4.22, though there are some differences. First of all there seems to be a larger decrease in capacity from 0.05C to 0.1C, and a bit smaller decrease from 0.5C to 0.1C. In addition, the bar group at 5C looks to have a slightly larger capacity here compared to Figure 4.22. The decrease in capacity from 0.1C to 0.5C is quite small, and the efficiency looks to be almost the same as in Figure 4.22.

In addition to these similarities, it is clear that also here the charge values are generally higher than the discharge and that the difference decreases with increasing rate. The difference is clearly largest for the last group of bars. Since the charge values looks to be the same in the first and last bar group, this means that the discharge values have decreased some the second time the rate is 0.05C compared to the first. The exact average discharge values for each group from left to right are 57, 46, 42, 39, 32, 25, 16 and 55 $\mathrm{mAh\,g^{-1}}$. The charge values are 60, 47, 43, 39, 33, 25, 16 and 60 $\mathrm{mAh\,g^{-1}}$. Hence, the last group shows the biggest difference between charge and discharge, measuring 5 $\mathrm{mAh\,g^{-1}}$.

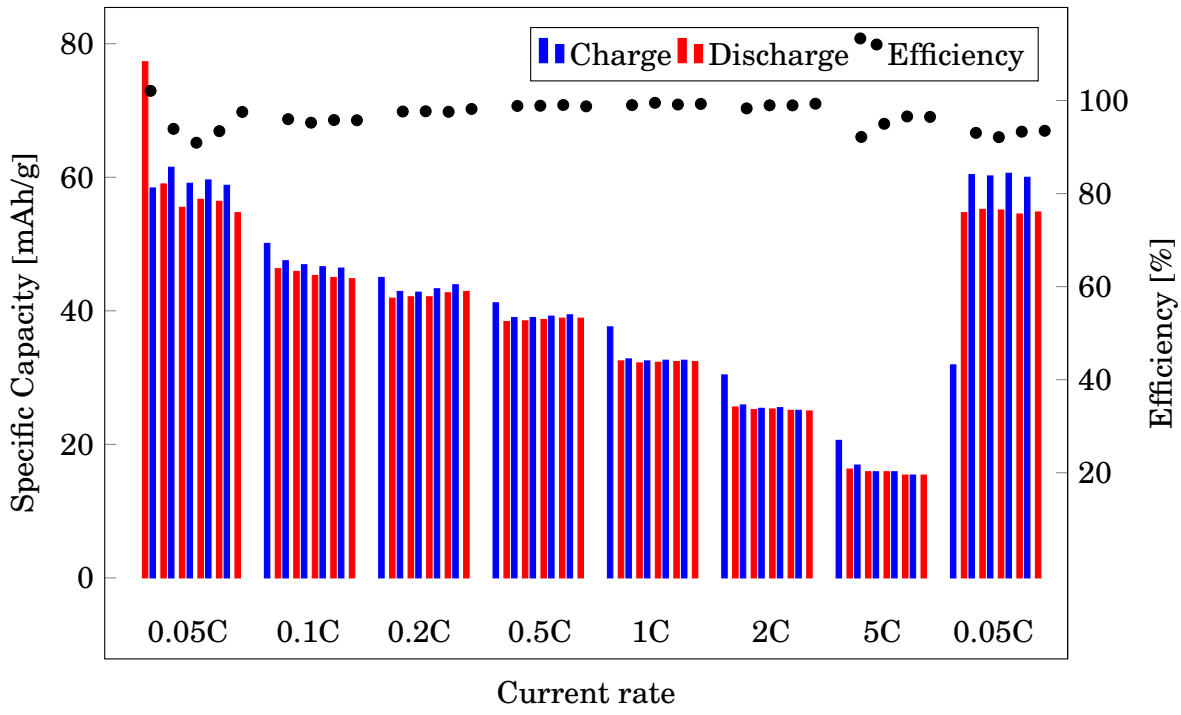

Figure 4.23: Rate capability of cathode of milled Mn_3O_4 with RGO showing how the specific capacity changes with current rate from 0.05C to 5C. The blue bars indicate charging values, and the red bars indicate discharging values. The cathode was cycled five times at each rate. The first group has six red bars due to the initial discharge, which do not count as a cycle. Active mass of the cathode was 1.56 mg.

Effect of slow rate

When preparing cathodes for ex situ study, these were cycled in batteries at the rate 0.02C. The resulting cycling data for some of these cathodes showed remarkably high capacity values for the first charge compared with all the batteries cycled at higher rates. One of the cathodes even obtained a higher capacity during the first charge than during the initial discharge. This feature is only seen for this cathode, which is illustrated in Figure 4.24. The cathode was cycled to the charge plateau of cycle 5, hence cycle 1 and 4 is shown with curves in addition to the initial discharge and the fifth charge up to the plateau. The capacities achieved for the initial, first and fourth discharge was 56, 39 and 38 $mAhg^{-1}$, while for the first and fourth charge the values were 59 and 43 $mAhg^{-1}$. Hence, there is a 5 % increase in the capacity from the initial discharge to the first charge. It can also be seen that there is quite a large difference in the values between the charge and discharge of cycle 1. The difference decreases for cycle 4 since the charge capacity then is lowered. There were two other cathodes cycled at 0.02C that showed similar tendency. These are presented in Appendix C.3 and had first charge capacity only 5 and 7 % lower than the initial discharge. It

should also be mentioned that the same was seen for the first cathode presented in Appendix A.1, were the cathode had been cycled at rate 0.1C. Other than the four cathodes mentioned here, no cathode showed similar first charge values. For the batteries cycled at 0.1C there usually was an approximate decrease in capacity of 30 % between initial discharge and first charge.

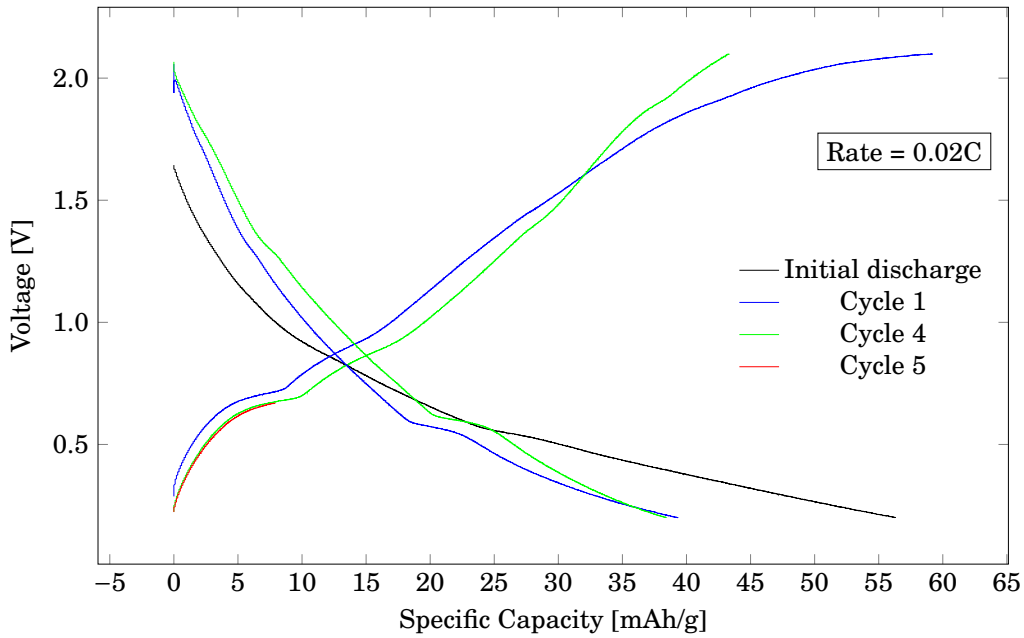

Figure 4.24: Charge-discharge curves for cathode of milled Mn_3O_4 cycled at 0.02C, showing an unusually high first charge capacity being 5 % larger than the initial discharge. Active mass of the cathode was 1.2 mg.

4.3 Investigations of charge-discharge mechanism

In order to investigate, and attempt to reveal, the working mechanism of the Mn_3O_4 cathode, several ex situ studies were performed. These were XRD scanning, SEM imaging with EDS analysis and TEM imaging with element analysis. The cathodes were prepared by galvanostatic cycling. Through individual cycling programs, described in the experimental section, the cathodes were cycled to different stages. To ensure as much reaction during each cycle as possible, a slow charge-discharge rate was used, i.e. 0.02C. Initially, six cathodes, A - F, were prepared for XRD analysis as described in the experimental section. Cathode A was a fresh cathode which had not been in a battery at all. Cathode B was removed from the battery after the initial discharge. Cathode C completed the initial discharge and the first charge, and cathode D completed the first cycle. For cathode E the cycling was stopped when the battery was at the charging plateau of cycle five. Lastly, for cathode F the cycling

was stopped when the battery was at the discharge plateau of cycle five. In order to verify results two extra cathodes were cycled, one to the charge and one to discharge of cycle 1. These were labeled G and H respectively. Results from the different studies are given in the following sections.

4.3.1 Ex situ XRD

The six cathodes A - F where first analyzed by XRD. Each cathode sample was scanned for two hours, with a step size of 0.02° using 2.3 seconds per step. The resulting X-ray diffractograms are given in Figure 4.25. The upper most, black, diagram corresponds to cathode A, and the following diagrams downwards are of cathode B - F respectively. The blue tics close to the x-axis is the standard pattern for Mn_3O_4.

From cathode A to B a decrease in peak hight can be seen. From cathode B to C a new peak can be observed at $2\boldsymbol{\theta}$ equal to 55, between the two small peaks. The peak is obvious in all the following plots. This corresponds however not to another phase, but to carbon, or graphite. Both this small peak and the large one at $2\boldsymbol{\theta}$ equal to 26 corresponds to carbon, which was in the samples due to the active material being scraped off the carbon paper.

From cathode B to C there is an increase in peak height again, and the peaks become larger than for cathode A. Cathode D show even smaller peaks than cathode B. Then, cathode E clearly has the smallest peaks, and compared to the peak heights there are quite a lot of noise in the diagram. For cathode F the peaks increase again, but not to the same height as for cathode D.

For cathodes C and D, a small peak can be seen at $2\boldsymbol{\theta}$ equal to 23. The peak is not observed in any of the other diagrams, and it is not particularly high compared to the noise around. These two experiments were therefore repeated for verification. Cathode G and H, which were cycled to charge and discharge of cycle 1 like cathode C and D, were used. XRD scans were conducted on these cathodes with a scan time of six hours per sample with a step size of 0.02° using 6.8 seconds per step. Increasing the scan time should reduce the noise in the diffractograms. The result of the scan is given in Figure 4.26.

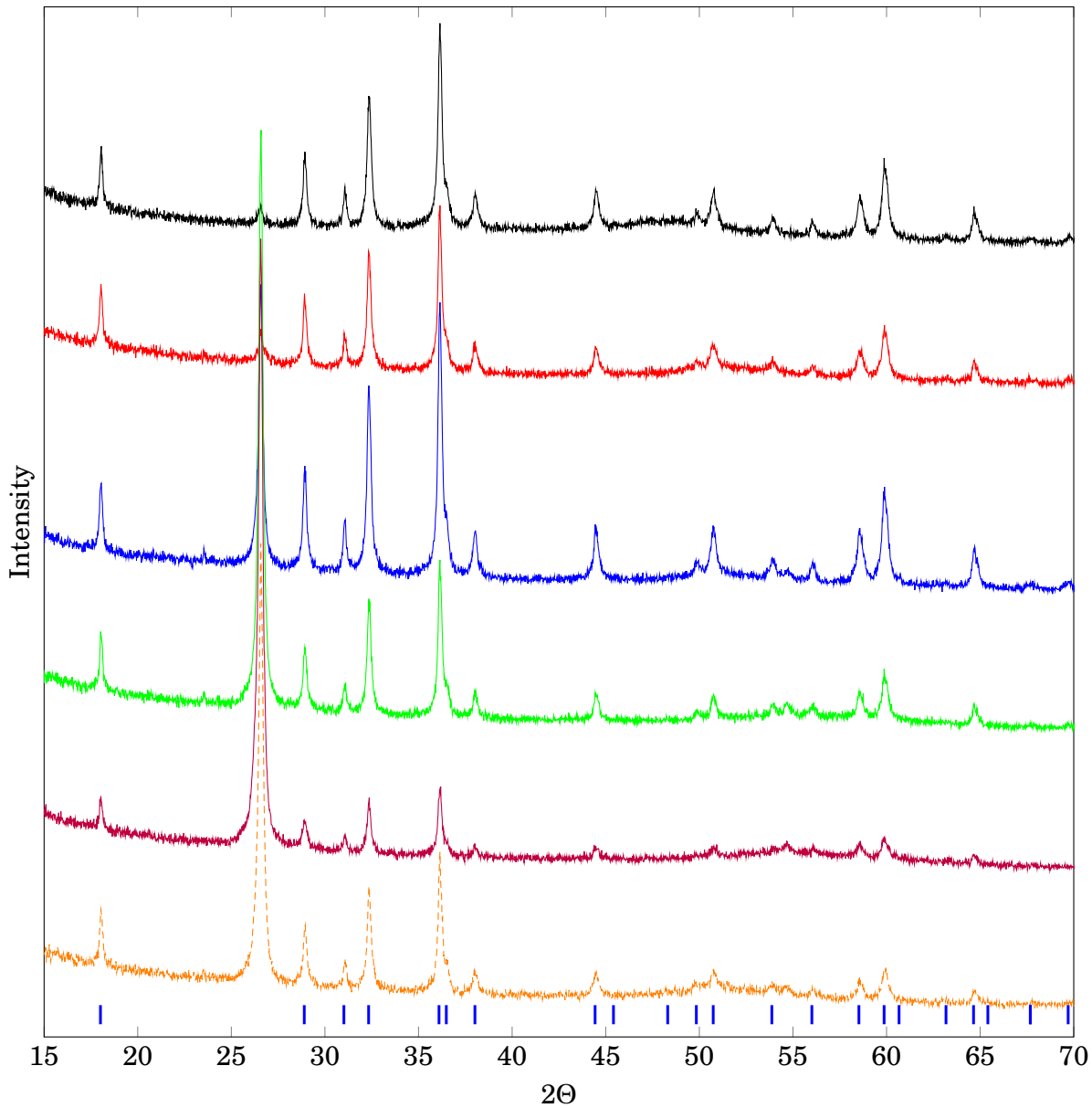

Figure 4.25: X-ray diffractograms from top to bottom, black to orange, for the cathodes A - F respectively. Cathode A was a fresh, not cycled cathode, cathode B completed initial discharge, cathode C completed first charge, cathode D completed cycle 1, cathode E was stopped at the charging plateau of cycle five and cathode F was stopped at the discharge plateau of cycle five. The standard pattern for hausmannite, Mn_3O_4, is given as the small, blue tics at the bottom of the figure. The scan time for each sample was two hours.

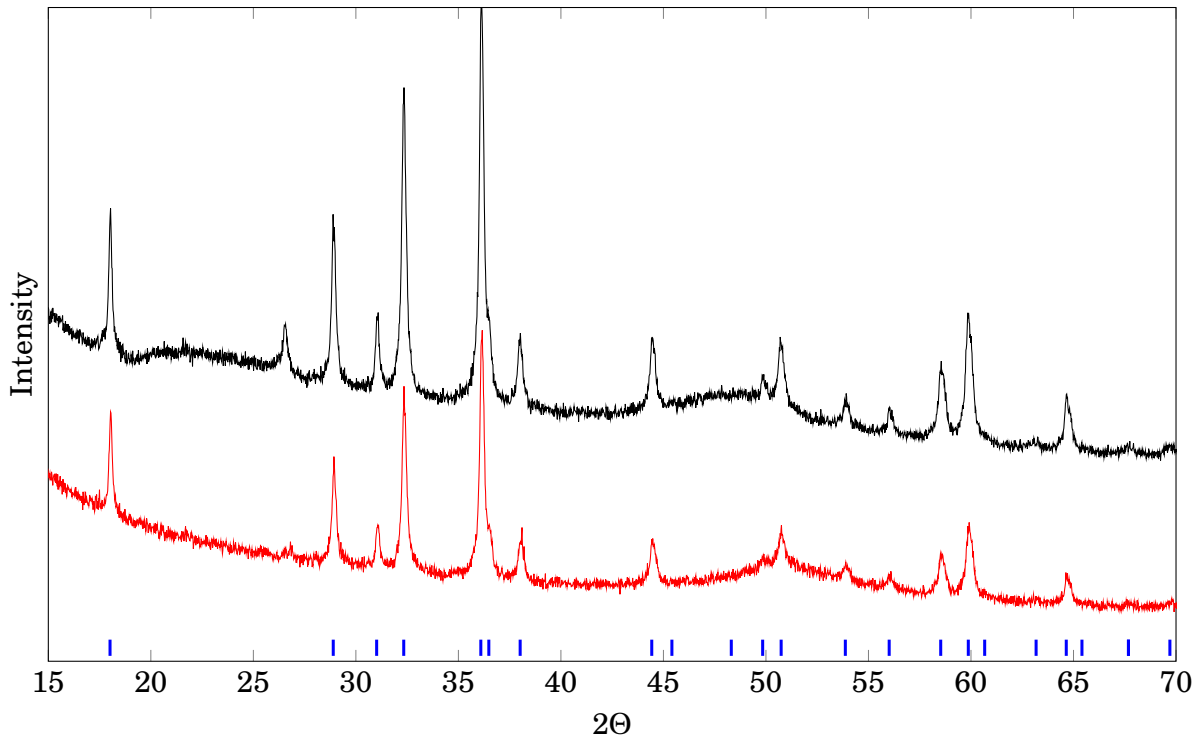

Figure 4.26: X-ray diffractograms of cathodes G (black) and H (red), these having been cycled to charge and discharge of cycle 1, respectively. The XRD scan time was six hours per cathode and the blue tics at the bottom of the figure is the hausmannite pattern.

Studying Figure 4.26, the peak observed at 2θ equal to 23 in Figure 4.25 is not found any more. This implies that the peak was not there to begin with and no structural changes have occurred in the cathode material during cycling. However, it is still very evident that the peak height is lower for discharged cathodes compared to charged. This indicate that a surface reaction occurred during discharge.

4.3.2 Ex situ SEM and EDS

After XRD measurements, the first four cathodes, A - D, were imaged in SEM and preformed EDS analysis on. Here it was the cathode surfaces that were analyzed. The cathodes were the fresh one, A, the one that completed the initial discharge, B, the one cycled to the first charge, C, and the one cycled to discharge of cycle 1, D. The SEM images and the EDS analysis of each of these are presented in the following sections.

Surface morphology

One SEM image of each of the four cathodes are presented in Figure 4.27. Image 4.27b is taken using the in lens SE detector, while the three others are taken using the out of lens

SE detector. There is little difference to be seen in the images. Each cathode surface seem to consist of agglomerates of different sizes randomly distributed. The agglomerates look quite densely packed with particles, suggesting there is small chance of electrolyte penetrating in. However, the overall surface seem porous due to the open spaces between the agglomerates. Since it is the cathode surface, as it would be in a battery, that is imaged, this should imply that the electrolyte would be able to soak through the outermost particle layer. How deep into the active material the electrolyte penetrates can not be determined by these images. However, it is clear that the electrolyte goes beyond the surface particles and comes into contact with the particles below, to some unknown depth.

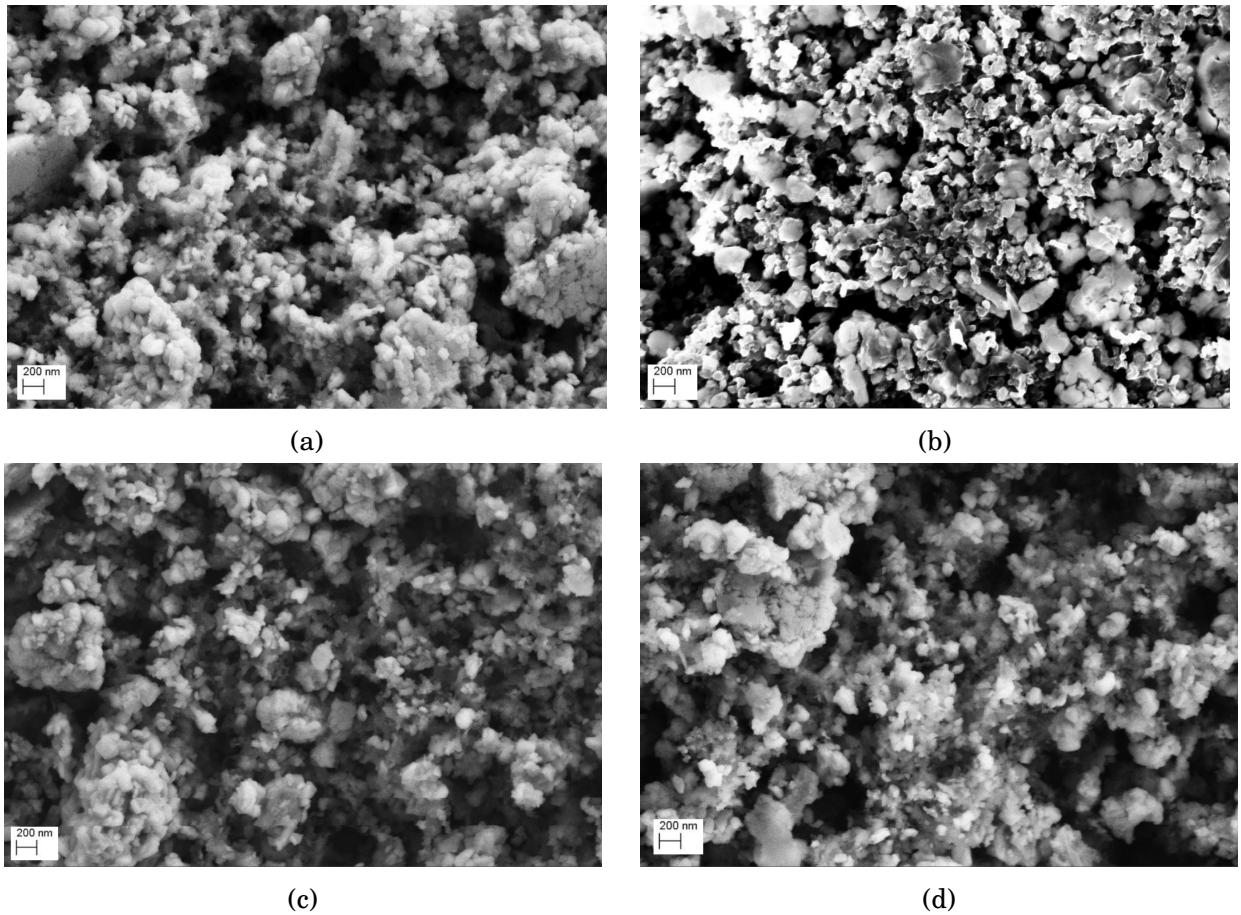

Figure 4.27: SEM images of (a) cathode A, (b) cathode B, (c) cathode C and (d) cathode D.

Surface composition

Resulting EDS analysis of the four cathodes are given in Table 4.2. At each cathode several areas were scanned, and the average atom% values from these scans are given in the table below. Table 4.2 show that the elements present in the fresh cathode were, as expected, manganese, oxygen and carbon. The three other cathodes had in addition chloride, magnesium and aluminum due to contact with the electrolyte. The raw data, including SEM images and EDS spectra are given in Appendix D. For cathode A, only one image was taken and in this two squares were scanned. For cathode B, four areas were scanned, cathode C had five scans and cathode D was scanned six times. Details of the EDS analysis for each cathode can be found in Appendix D.1, D.2, D.3 and D.4 respectively.

	Cathode A	Cathode B	Cathode C	Cathode D
Element	Atom%	Atom%	Atom%	Atom%
Mn	34	36	20	21
O	32	32	42	40
C	35	29	34	38
Cl		1.3	1.9	0.9
Mg		1.3	1.5	1.2
Al		0.4	0.3	0.2

Table 4.2: Table of the average atom% values for each of the elements detected on the surface of the cathodes using EDS.

From the table, it can be seen that for cathode A, carbon had the highest atom% value while oxygen had the lowest. The difference is very small though, and each element constitute approximately one third of the total. For cathode B, there is still mostly manganese, oxygen and carbon, but also a small amount of chloride, magnesium and aluminum was detected. The amount for these last three elements increases for cathode C, which is the charged cathode, and decreases again for cathode D. Also for cathode C and D, a quite noticeable decrease in the amount of manganese can be seen. It should be mentioned that the EDS measurements are not very accurate, the error margin being 2 - 3 %.

4.3.3 Ex situ TEM

In order to observe possible differences between charged and discharged cathode, two samples were prepared for TEM imaging and element analysis. The samples were one cathode cycled to charge and one cycled to discharge of cycle 1. The discharged sample was first imaged to look for a surface layer. After, both samples were subject to element analysis to determine the amount of magnesium. The results from these examinations are presented in the two following sections.

Surface layer assessment

Since the XRD analysis showed decreased peak heights for discharged compared to charged cathode, the surface of a discharged particle were examined using TEM. In order to determine if there was a surface layer formed on the particles, a straight edge was found and carefully studied. Figure 4.28 show four images, the first one, Figure 4.28a, shows the evaluated edge. Figure 4.28b shows the single crystal structure of the [111] plane for the particle. Then, Figure 4.28c and 4.28d show that there is no surface layer and that the entire particle is crystalline.

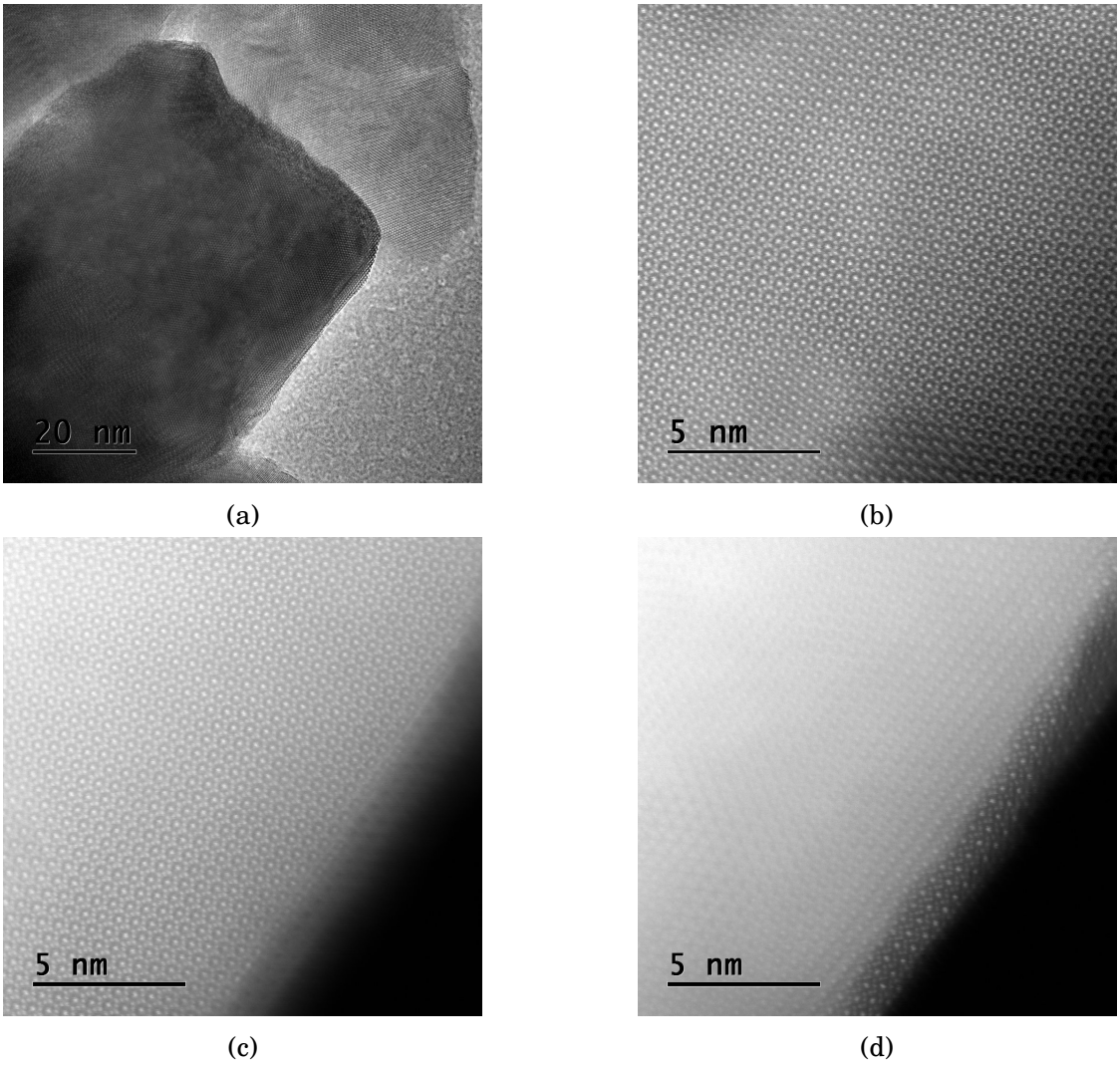

Figure 4.28: TEM images of (a) the edge of a discharged particle to be evaluated for existence of surface layer, (b) the particle's single crystal structure, (c) area approaching the edge being crystalline and (d) the edge itself being crystalline.

Element analysis

Element analysis was performed on both the samples of charged and discharged particles. This in order to determine how much magnesium the samples contained and where it was located.

Starting with the discharged sample, the element mapping is illustrated with four images in Figure 4.29. First the entire agglomerate shown in Figure 4.29a was scanned. The mapping of manganese, green, and magnesium, red, is shown in Figure 4.29b. The entire agglomerate was found to contain 0.9 atom% magnesium. From the mapping image, Figure 4.29b, it was seen that the magnesium primarily was found on particle edges and in grooves between particles. In order to see the Mg more clearly, the yellow square in Figure 4.29b was mapped, illustrated in Figure 4.29c. The image show an especially thick layer of magnesium on one side of the particle in focus. There is a clear difference in amount of magnesium at the bulk part of the particle and the edges, especially the left side edge. To evaluate the difference between these two areas, element spectra from each of the two red squares in Figure 4.29d were obtained. This image show the total amount of magnesium as white dots, and is also a good illustration of the surface preference. By normalizing based on the amount of manganese, both spectra were collected in the same diagram, which is presented in Appendix E.1. From the spectra it can be seen that there is a large difference in the amount of magnesium in the two areas. The bulk was found to contain 0.6 atom% magnesium while the surface layer contained 10 atom%.

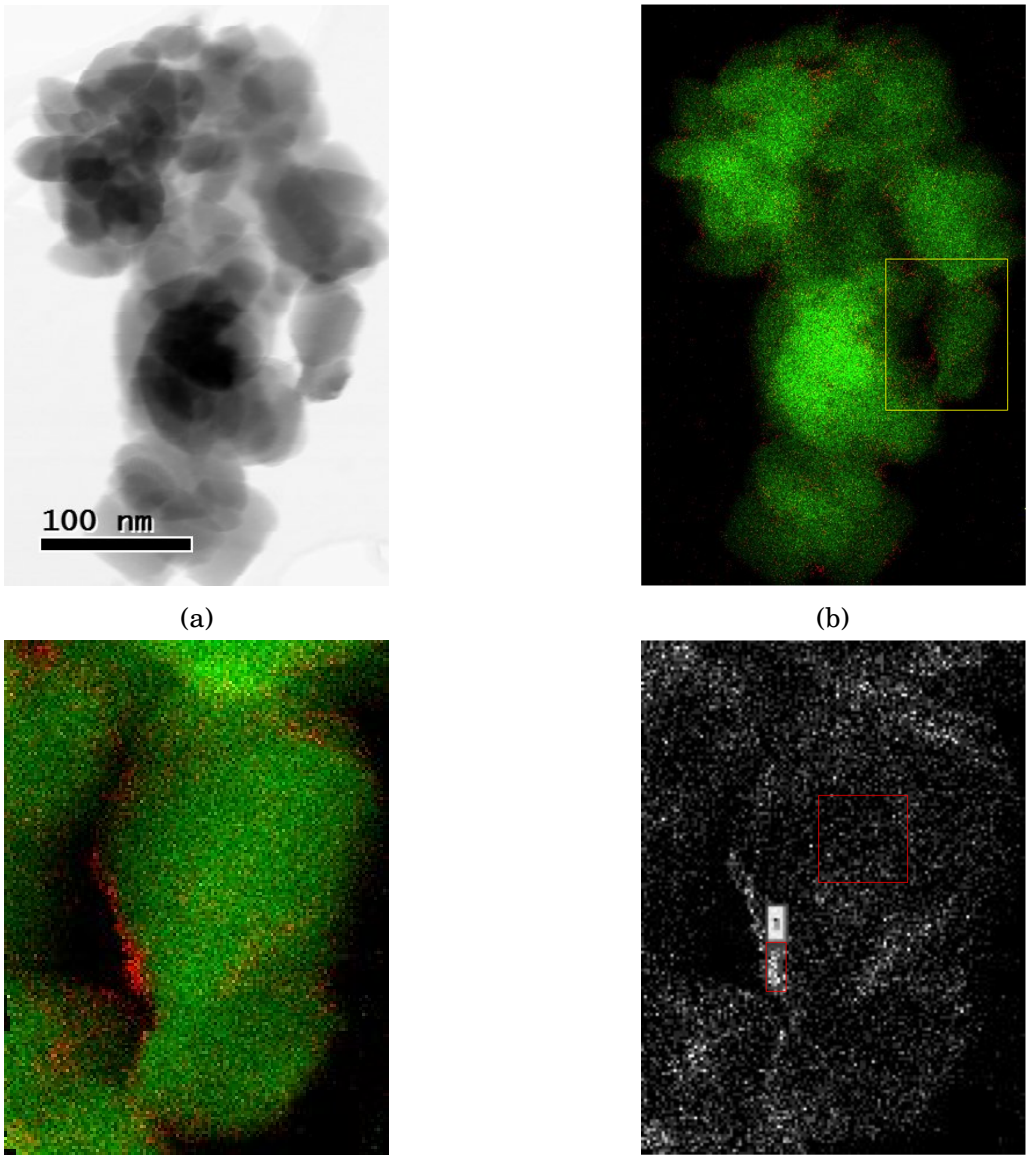

(a) (b) (c) (d)

Figure 4.29: STEM images from element analysis of discharged agglomerate showing (a) the scanned agglomerate, (b) mapping of manganese (green) and magnesium (red) on the agglomerate, (c) mapping of manganese and magnesium within the yellow square in image (b) and (d) the total amount of magnesium and the two areas spectra were obtained from.

Mapping of the charged sample is illustrated in Figure 4.30. The agglomerate mapped, which can be seen in Figure 4.30a, was much smaller than the one for the discharged sample above. Figure 4.30b shows the mapping of manganese, green, and magnesium, red. Also here it is clear that magnesium mostly can be found deposited on edge surfaces of the particles. Figure 4.30c, showing the total amount of magnesium on the agglomerate illustrates this surface preference even better. Spectra from the two red squares in that image, plus one spectra for the entire agglomerate, were obtained in order to determine the difference in amount of magnesium. Again the spectra were normalized based on the amount of manganese and included in the same diagram. This can be found in Appendix E.1. The total average amount of magnesium for the entire agglomerate was 1.2 atom%, the square in the bulk region contained 0.4 atom% while the square at the edge contained 5 atom%.

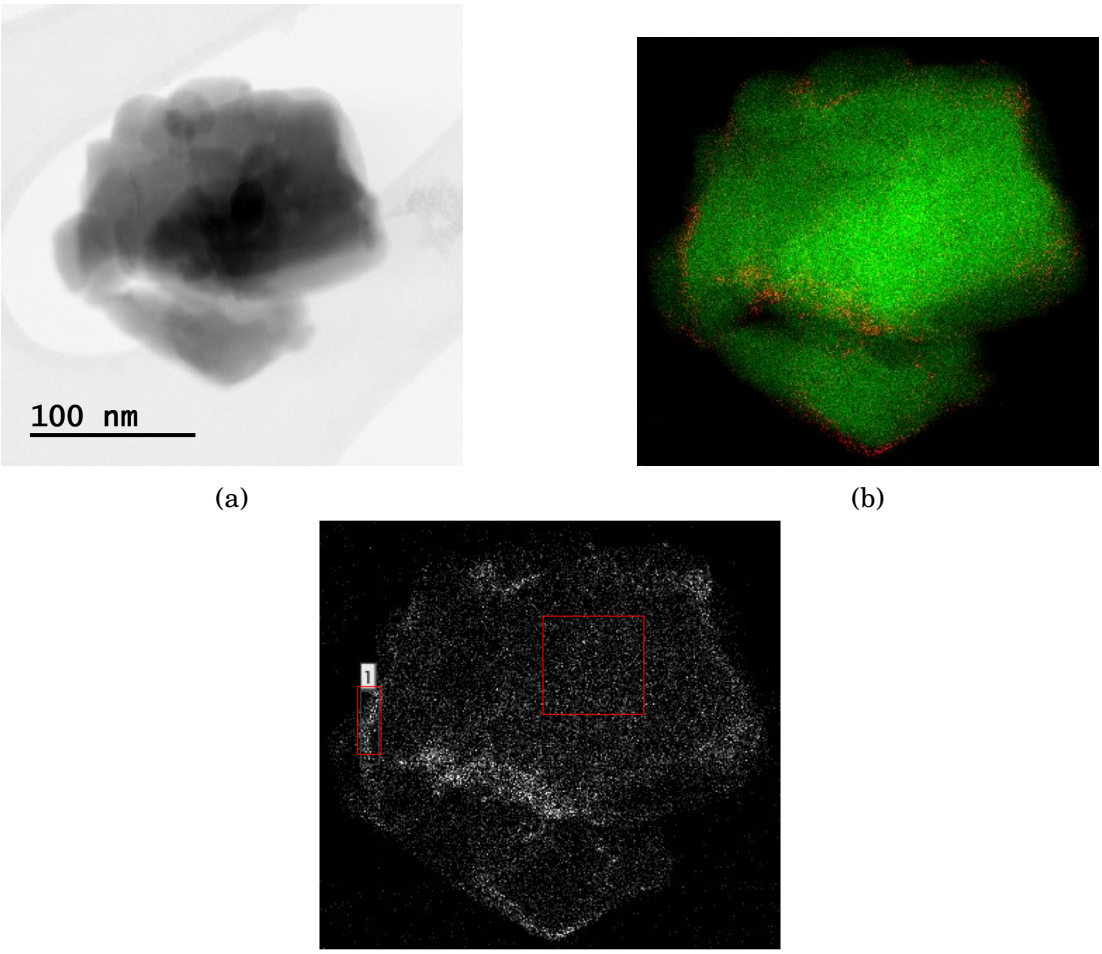

(a) (b)

(c)

Figure 4.30: STEM images from element analysis of charged sample showing (a) the scanned agglomerate, (b) mapping of manganese (green) and magnesium (red) on the agglomerate and (c) the total amount of magnesium on the agglomerate and the two squares spectra were obtained from.

Chapter 5

Discussion

In this chapter the obtained results will be discussed based on the theory presented earlier. The results will be discussed in the same order as they were presented in the results chapter.

5.1 Effect of surface area

The commercial Mn_3O_4 powder was milled with the intention of increasing the surface area. The increase was, after measurements, found to be 15 %, i.e. from 9.6 to 11.3 $m^2 g^{-1}$. Only a very small amount of this was micropore area, hence most would be accessible for the electrolyte. From SEM images, Figure 4.2, the degree of agglomeration seemed lowered for the milled powder. However, all the particles were still agglomerated, which means that much potential surface is inaccessible. Hence, even though the particles are less densely packed into smaller agglomerates after milling, the commercial Mn_3O_4 powder still contain particles that prefer to agglomerate, causing a low active surface area. Milling is however a relatively gentle method to increase the surface area. There are many other rougher methods that could have been used to break the agglomerates apart.

From the TEM images, it was found that the agglomerates are quite different from one another. They vary both in size and density of particle packing. It was also seen that the particle size distribution in the powder is wide. The larger particles have a clear rectangular shape where the length is about twice the size of the width. Also, most of the smaller particles show an elongation in one direction. The largest particles seen had a length of around 150 nm and a width between 50 and 100 nm. The smallest particles on the other hand had size around 20 nm. Knowing this, the equation used to calculate approximate particle size in results section 4.1, assumes the wrong particle shape and the value 113 nm can not be correct. However, this value is in the particle size range observed for the TEM images and is thus possibly not a bad estimation. The density of particle packing in the agglomerates will largely affect the total active surface area. Particles completely boxed in between other particles will not come into contact with electrolyte and hence not contribute to the capacity output of the material. Also, pores in between densely packed particles will

probably be too small for the electrolyte complexes to fit into. After all, it has been found for LIB systems that micropores are too small for the electrolyte complexes, theory section 2.3.1. Hence, if the complexes in the MIB electrolyte is of similar size, these pores can not be utilized here either. Thus, less densely packed agglomerates are desired. With regard to the measured surface area though, these are probably not in excess in this powder, milled or not.

Even though the milling did not have a large effect on the surface area, the milled powder seemed to have a more successful mixing with reduced graphene oxide compared to the not milled powder, seen in Figure 4.4. It would appear that the less agglomerated Mn_3O_4 powder was easier to disperse among the reduced graphene oxide sheets. For the not milled powder there was a quite obvious degree of the sheets wrapping the agglomerates. In the SEM images for the milled powder on the other hand, the sheets looked to be more intertwined in between the smaller agglomerates. This creates possibly a better network for electron transport. Also, in the images of the not milled powder, the graphene oxide sheets looked thicker as if there were several sheets on top of each other. If that is the case, the milled powder should have a better exploitation of the advantages with including graphene oxide since the sheets are more distributed.

The poor effect of the milling can however be due to the choice of milling medium. Aceton was used, which is not the most suitable solvent for such a treatment. Aceton will leave an organic coating on the particle surfaces, which can only be removed by heat treatment at a couple of hundred degrees Celsius. Such a surface layer can reduce the conductivity and hence the performance of the particles. This was however not discovered until it was too late to redo the milling. The results obtained can thus be compromised by this unfortunate experimental mistake.

5.2 Electrochemical performance

5.2.1 Short term performance

For all four types of cathode presented in the results section 4.2.1, all the poorest cathodes were shown to have very stable capacity throughout the cycling. This is owed to the fact that they all had active mass from 2.0 mg and upwards. Cycling was found to take longer time the less active mass the cathodes contained. Results section 4.2.2 showing the long term performance of the cathode illustrates this well. When the cycling is done in a shorter amount of time, the cathodes are less exposed to environment changes. Temperature, for example, will vary depending on how much activity goes on in the room where the battery tester is located. During nights and weekends there will be much less activity than during daytime in the weekdays. Compared to one another, the poorest cathode of each type showed decreasing capacity with increasing active mass, though not a linear decrease.

The best cathode of each type on the other hand are more different from one another when

it comes to the capacity development during the 50 cycles. The best cathode of untreated Mn_3O_4 showed an increasing difference between the charge and discharge capacities with cycling. Meaning that while the charge capacities slowly increased with cycling, the discharge capacities slowly decreased. The same was not seen for the best cathode of milled Mn_3O_4. There the charge and discharge capacities followed a trend more similar to one another, though with charge capacities constantly a few $mAh\,g^{-1}$ higher than the discharge. The capacity was thus more stable for this cathode, though a dip in the capacity curves were seen around cycle 25. A temperature difference could explain this, for example could the decrease correspond to a weekend with less activity in the room where the batteries were tested.

A temperature difference alone can however not explain the increasing difference between charge and discharge values for the best cathode of not milled Mn_3O_4. Remembering the discovery of oxidizing THF molecules in electrolyte systems for MIBs, presented in theory section 2.5, that feature is interesting here. Oxidizing THF would contribute to the charge capacity, hence this can be an explanation to why the charge capacities are higher than discharge. In addition, THF has a boiling point around 65 °C, so variations in temperature can have quite an effect on the activity of the THF molecules. The room where the battery tester is located do not have any temperature control, so there is no way of knowing how this varies. The room contains much equipment and on sunny days the sun shines into the room increasing the temperature. Trapping was introduced in the theory section as a reason for poor solid state diffusion of Mg^{2+}-ions. This feature will be described more thoroughly in the discussion of the charge-discharge mechanism later. Though it can be mentioned that if magnesium ions are trapped during the initial discharge in such a way that it is possible to extract some during later charges, that could explain the slow increase with cycling. If the same process causes a slight decrease in possible sites for Mg at the cathode with cycling, the decrease in discharge capacities have an explanation as well.

The best cathode of not milled Mn_3O_4 with RGO had, compared to all other cathodes, a remarkable high specific capacity. The active mass of the cathode was 1.09 mg, so it was not the cathode with the lowest active mass tested and yet it achieved 78 $mAh\,g^{-1}$. The cathodes closest in capacity were still more than 10 $mAh\,g^{-1}$ lower. Strangely, the best performing cathode of milled Mn_3O_4 with RGO showed a much lower capacity than the not milled Mn_3O_4 with RGO. The difference in capacity between those two was 18 $mAh\,g^{-1}$, while they had the same active mass. Here it could be the effect of using poor milling solvent that is visible. However, such an effect was not seen for the cathodes of pure Mn_3O_4. For the cathode with RGO it is not possible to know the true ratio between Mn_3O_4 and RGO. If there is a higher percentage of RGO on the cathode of not milled Mn_3O_4, this might have increased the electronic conductivity so that the capacity increased. It is also not possible to know the distribution between large and small Mn_3O_4 agglomerates on the cathode. Active surface area play an important role in determining the performance of the cathodes, hence variations would cause different capacities.

The capacity development during the cycling had a bit more uneven trend for the best cathode of not milled Mn_3O_4 with RGO than for the cathodes without RGO. The charge and discharge capacities follow each other quite well though, with the charge slightly above the discharge, and the variations in capacity are merely a few $mAh\,g^{-1}$. The overall cycling stability was quite good. For the best cathode of milled Mn_3O_4 with RGO on the other hand, the charge and discharge capacities had the same values. Hence, this cathode was the only one not showing higher capacity values for charge than for discharge. Regarding the possible reasons why the other cathodes show higher charge capacity values, it might be that THF oxidation do not provide the same effect here, that the temperature generally was lower during the cycling or that trapped magnesium was not accessible for extraction. There is quite a decrease in capacity from the initial discharge to the remaining cycling where the capacity is extremely stable, but all the cathodes show such a drop with the same size.

In addition, most of the cathodes shown in the results section did not have a proper discharge plateau for cycle 1. Some of the poorest cathodes did not even show a bend in the curves. The best cathodes had a slight tendency of a plateau, but non showed an actual plateau until cycle 5. Hence, the cathodes need a few cycles for the plateaus to become fully established. Most of the poorest cathodes did not show a proper discharge plateau for the fifth cycle either, suggesting that the poorer performing cathodes need more cycles until the plateaus are completely established. Also, most of the cathodes showed a shift in the charge and discharge plateaus, towards more equal voltage. This could, according to theory section 2.1.1, indicate faster kinetics during cycling. The shifts are not large though, and could merely be a decrease in the polarization of the material.

5.2.2 Long term performance

Both cathodes presented in results section 4.2.2, showed very stable performance with high efficiency. There was no sign of failure during the 500 cycles. Hence, even though the capacity is not very high, the performance is proved to be steady and have a long duration. The charge-discharge curves showed a clear shift in the plateau just like the cathodes only cycled 50 times. This being an indication of slightly improved kinetics, or decrease in polarization, during cycling. The cathode of milled Mn_3O_4 with RGO showed a higher capacity than the cathode of not milled Mn_3O_4 with RGO, but the active mass of the milled one is also lower. Except from the first cathode presented in the long term performance result section, the cycling time was found to increase with decreasing active mass. Hence, each charge and discharge took longer time the less active mass there were the on the cathodes.

5.2.3 Active mass dependency

In the results section 4.2.3, both a figure and a table is given, summing up the obtained capacities during the short term performance test. The cathodes of untreated Mn_3O_4 was the only type that did not achieve highest capacity for the cathode with the lowest, but the

second lowest, active mass. The difference in capacity was however only 1 $mAh\,g^{-1}$ and just 0.16 mg separated the two cathodes. For the cathodes of milled Mn_3O_4 there is a constant increase in capacity with decreasing active mass. For the cathodes of untreated Mn_3O_4 this could simply be a case of variation in experimental data.

In Table 4.1, the cathodes of not milled Mn_3O_4 with RGO were also found to have two cathodes that seemed to have switched places with regard to the performance. A cathode with active mass 1.36 mg obtained a capacity 1 $mAh\,g^{-1}$ lower than a cathode with active mass 1.5 mg. Also, for the cathodes of milled Mn_3O_4 with RGO there are strangely little difference in the achieved capacity between the two cathodes with lowest active mass. Though the difference in mass was 0.27 mg, the difference in capacity was only 1 $mAh\,g^{-1}$. For the cathodes with RGO it is not possible to know the true ratio of Mn_3O_4 and RGO on the cathodes. Differences in this ratio might be the cause for this irregularity. However, this ratio would not explain why the same is seen for the untreated Mn_3O_4 as well. All in all only 3 of 32 batteries showed this irregularity, hence it is most likely not an issue.

Apart from those three batteries, there is a clear trend suggesting that the amount of active mass on a cathode takes part in determining the resulting specific capacity. A rather small difference in mass, about 1 mg, results in quite a large variation in capacity, up to 46 $mAh\,g^{-1}$. If there is a limit to how deep into the cathode material the electrolyte can soak, a thicker layer of material would then only act as dead weight. Adding more material would decrease the specific capacity since the mass increases while the capacity output is the same. The soaking limitation could be due to all the particles being agglomerated, creating few routes the electrolyte can take through the material. Also, the larger the agglomerates are, the less surface area they offer per gram active material. Size of agglomerate could explain the irregularity mentioned above because there is no way of knowing the ratio between large and small agglomerates on each cathode. The cathodes showing unusually low capacity could have unusually many large agglomerates compared to smaller ones, which offer more surface per gram.

5.2.4 Rate dependency

The figures presented in results section 4.2.4 showed two cathodes who's rate capability were tested, the current rate varying from 0.05C to 5C, and one cathode having been cycled four times at rate 0.02C. Staring with the cathodes subjected to the rate capability test, they showed decreasing capacity with increasing rate. When switching to slow rate again, both cathodes regained their initial capacity. Just like the cathodes cycled 50 times at rate 0.1C, the rate capability test showed that the charge capacities generally were higher than the discharge. This was especially seen for the cycles run at low rates, i.e. 0.05C. The extreme version of charge capacity higher than discharge was seen for the cathode cycled at 0.02C. There the first charge capacity was actually 5 % larger than the initial discharge. Hence, there were more oxidation than reduction occurring. The batteries rate capability tested had a decreasing difference between charge and discharge capacities with increasing rate.

When the rate was switched back to the originally low value, 0.05C, the difference increased again, becoming slightly larger than initially.

The same trend with decreasing difference between the charge and discharge capacities was seen for both the cathode of pure, milled Mn_3O_4 and the cathode of milled Mn_3O_4 with RGO. This suggests that there is a reaction, or extent of a reaction, that only occurs when the rate is slow enough and which is independent of the electronic conductivity. It was seen in the figures that the initial discharge, when the first Mg^{2+}-ions comes to the cathode, had a much larger capacity than all other charges and discharges. In the theory section 2.3.1, Mg trapping was presented as one of the causes for slow Mg solid state diffusion. It could be that magnesiation of the Mn_3O_4 cathode during the initial discharge occur in such a way that some of the Mg^{2+}-ions are difficult to release from the cathode again. A slow rate would provide longer charge time, and might increase the possibility for extracting potentially trapped ions. Extraction of trapped ions does however not necessarily imply that the trapping sites are available for new insertion during the next discharge. The initial trapping can be due to the polarization effect by intercalating Mg^{2+} which has such a high charge/radius ratio. Also, local deformations in the material can occur when manganese reduces to compensate for insertion of Mg^{2+}. In Mn_3O_4 it must be Mn^{3+} that reduces to Mn^{2+}, which means a decrease in Jahn-Teller active ions. However, it could be that a size increase accompanies the reduction seeing as Mn-ions are known to increase with a factor of 1.75 when reducing from 4+ to 2+. The increase should be less when going from 3+ to 2+, but can still be enough to block both the diffusion path further into the material and the extraction path. Thus, the trapping sites after extraction would probably be blocked for new insertion by deformations. In the following discharges, the Mg-ions would then have to attach to the cathode surface. Hence, there are less active sites during discharge compared to charge, causing higher charge capacities compared to discharge.

Extra charge capacity could also be due to oxidation of electrolyte. In which case that reaction can not happen at higher rates either. Oxidation of THF can explain how the first charge capacity of the battery cycled at 0.02C was higher than the discharge capacity. The extra 5 % capacity, and probably more than that, could come from THF oxidation, seeing as it is not likely that if magnesium is trapped, that all those Mg-ions would be released again during the first charge. For the cathode cycled at 0.02C, the large reduction in capacity from first charge to discharge of cycle 1 could be explained by Mg only attaching to the cathode surface, not intercalating, during the second discharge. Seeing as the active surface area of the material is low, there would be fewer active sites.

Studying the CV curve for pure Mn_3O_4 given in theory section 2.4, the charge curve, or upper half of the CV curve, is seen to have two oxidation peaks. The discharge curve on the other hand only has one peak. One explanation to this could simply be that oxidizing manganese is a two step process while the reduction goes over one step. However, knowing that THF is found to oxidize as well, a more logic explanation can be that the second

oxidation peak in the CV curves is owed to this reaction. The larger charge peak and the discharge peak are almost at the same voltage value, indicating a reversible reaction. Both this and the fact that it was generally found higher charge capacities than discharge during cycling also supports the explanation about oxidizing THF. After all, there can not constantly be more oxidation of manganese occurring compared to reduction. Remembering the rate capability plots, it was seen that the difference between charge and discharge capacities decreased with increasing rate. This suggesting that the extra oxidation occurring only can happen at low current rates. The CV curve for the pure Mn_3O_4 was obtained using a sweep rate of 0.2 $mV s^{-1}$. Comparing this CV curve with the one for an electrochemical capacitor presented in theory section 2.1.1, similarities can be seen. If the peaks in the CV curves for the pure Mn_3O_4 are disregarded, the curves look very much like the ones obtained at the lower rates for the capacitor. It could be possible that with increasing rate, the performance of the Mg batteries with Mn_3O_4 cathode become more equal to that of a capacitor. This suggesting that the redox reactions only will occur when the rate is slow enough. After all, the rate capability showed a large decrease in capacity, relative to the initial value, when going from 0.05C to 5C. In addition, even though the sweep rate was low during the cyclic voltammetry, the area under the peaks is small compared to the total area between the curves. This suggesting that more capacity comes from charge separation than from reduction and oxidation reactions.

5.3 Charge-discharge mechanism

Crystallinity

XRD analysis of the cathodes, results section 4.3.1, showed that for discharged cathode the height of all peaks were decreased compared to fresh or charged cathode. There were no change in peak position or new peaks appearing for the cycled cathodes, suggesting that intercalation did not happen. Intercalation would have changed the cathode material and would thus have been apparent in the diffractograms. The decrease in peak height does however imply that something has occurred at the material's surface. In theory section 2.3.2, $\alpha-MnO_2$ was presented as a cathode material for MIBs which formed a core-shell structure as discharge product. The particle cores were pristine $\alpha-MnO_2$, while the shell was an amorphous layer of MnO and MgO. Due to the stability of MgO, this conversion reaction is thermodynamically favorable. XRD analysis for this material also showed decreased peak heights for discharged cathodes compared to fresh. Hence, the surface reaction occurring during discharge for Mn_3O_4 could also be formation of amorphous MnO and MgO.

In results section 4.3.3, TEM images of a discharged cathode were presented. Here it was found that there was no surface layer on the particles. The entire particle studied in the discharged sample was crystalline. Hence, the surface reaction causing decreasing peak heights in the X-ray diffractogram can not be formation of amorphous MnO and MgO. In the theory section 2.3.2, $\gamma-MnO_2$ was described as an intercalation cathode for MIBs. $\gamma-MnO_2$

have the spinel structure like Mn_3O_4, and Mg^{2+} was found to most likely intercalate in tetrahedral sites. A tetrahedral site would be equally large in the $\gamma-MnO_2$ and Mn_3O_4. A difference between the two though, is that Mn_3O_4 already have some Mn^{2+}-ions occupying tetrahedral sites. From the calculation of tetrahedral and octahedral sites in theory section 2.4 and the known size of Mg^{2+}-ions, the ions are in theory too large to fit in a tetrahedral site. Seeing as $\gamma-MnO_2$ have manganese ions only in octahedral sites, this structure might have less problem accommodating the Mg^{2+}-ions. It is possible that intercalating Mg^{2+}-ions into Mn_3O_4 is more difficult due to cation repulsion, since there are more cations per unit cell in this structure. However, the STEM image of Mg intercalated $\gamma-MnO_2$ is very similar to the STEM image of discharged Mn_3O_4 presented in the results section. As mentioned though, Mn_3O_4 have Mn^{2+}-ions occupying tetrahedral sites, so this can be the reason the two materials look so similar in the STEM images.

With regard to the XRD results and the theory about $\gamma-MnO_2$, a possible explanation could be that intercalation can occur in the outermost few nanometers of the particles. There must then be enough intercalation to alter the surface so that the XRD peaks are decreased, but not an amount that would create a new surface structure. Also $\alpha-MnO_2$ was in the theory section said to be able to intercalate a limited amount of Mg. This occurred due to a kinetic barrier against direct conversion. Hence, both example materials show some degree of intercalation of Mg^{2+}. Like discussed for the rate dependency, it could be that the Mg-ions managing to intercalate in the outermost nanometers are trapped. Trapping should block further intercalation, forcing attachment of Mg by a surface reaction instead of intercalation during the following discharge. This can explain the decrease in capacity between the initial discharge and cycle 1 for cathodes cycled at 0.1C. Hence, it is suggested that intercalation occur during initial discharge while only attachment through a surface reaction happens in the following discharges. One week spot in this suggestion though, is that if XRD could not detect the potentially trapped magnesium, there should probably not be enough in the material to cause such a large capacity drop from the initial discharge to cycle 1 as seen for the cathodes.

Both characterization methods, XRD and TEM, used here utilize a strong electron beam. The strength of the beam is such that it penetrates into the material instead of only analyzing the surface. Hence, these two methods are not the best for surface analysis. Another characterization method more suitable is X-ray photoelectron spectroscopy (XPS). It can be that there is in fact a surface layer, but so thin that the electron beam goes through it without detecting the composition. Formation of amorphous MgO is after all thermodynamically favorable.

Morphology and surface composition

The SEM images of the cathode surfaces, results section 4.3.2, showed no difference in surface morphology between the fresh cathode and those cycled to different stages. There were nothing distinct separating any of the four cathodes imaged. One feature the images did

show though, was the distribution of the agglomerates. Openings between the differently sized agglomerates were seen, hence the electrolyte should be able to soak through the top layer of particles and down to the underlying agglomerates. How deep into the cathode material the electrolyte will soak is however not possible to determine from the images. It is clear, though, that the packing density of the agglomerates will affect the degree of soaking here. Areas with densely packed agglomerates that are closely spaced can work as blockage for the electrolyte, as opposed to less densely packed agglomerates where the electrolyte can go through, in between the particles, if it can not get around.

The EDS data showed that the charged cathode had more magnesium at the surface than the discharged cathodes. Since Mg^{2+} is transferred to the cathode during discharge and from the cathode during charge, the resulting data is the opposite of expectations. Hence it must be mentioned that this method for element analysis has an error margin of 2 - 3 %. Seeing as the highest value obtained for amount of magnesium was 1.5 atom%, the values are quite inaccurate. The values can be regarded as an indication of element amounts relative to each other, but they alone are not good enough grounds to conclude that there is more magnesium on charged cathode compared to discharged. In any case, there is very little difference between the values for the three cycled cathodes, hence more data is needed.

The element analysis performed with STEM, which is much more accurate, indicated opposite result compared to the EDS analysis when using SEM. For the agglomerates analyzed, presented in Figure 4.29 and 4.30, the discharged particles showed thicker layers with a higher content of magnesium than the charged particles. The content values of magnesium for discharged sample was twice that for charged sample, both at bulk and edge areas. For the total amount of magnesium on the entire agglomerates on the other hand, the charged sample had a higher value than the discharged. However, the size of the agglomerates were different. The discharged agglomerate was much larger than the charged, while the content values only differed by 0.3 atom%. It should be mentioned that there is no way of knowing where in the cathode material the different agglomerates were positioned during operation. Though it is certain that both have been in contact with electrolyte since traces of magnesium is seen all around both agglomerates. This indicate that the results are representative for the samples.

It was also seen from the images that the magnesium to a large degree was found on particle edges. The images showing the mapping of manganese and magnesium, clearly show surface areas with relatively thick layers of magnesium. In addition it did not seem to be a uniform distribution of magnesium on the different surfaces, indicating preferential deposition. Edges were seen to have more accumulation of magnesium than the large, uniform surfaces. This can be due to both difference in surface energy and difference in current density, as both of these usually are higher at edges than flat surfaces. Hence, the results indicate more magnesium at the discharged particles compared to the charged, and suggests a charge-discharge mechanism involving attachment and de-attachment of magnesium on

the cathode surface.

5.4 Further work

For further work, a new attempt should be made on investigating the effect of active surface area on the performance of the cathodes. Rougher methods should be implemented to break the agglomerates in the commercial Mn_3O_4 powder apart. In addition, the ball milling can be attempted again, this time with a more suitable solvent such as ethanol.

In order to obtain more insight into the charge-discharge mechanism, cyclic voltammetry should be run at higher sweep rates than 0.2 $mV s^{-1}$. More specifically rates corresponding to the current rates used when testing rate capability of the cathodes in this work. If the peak corresponding to THF oxidation disappears from the CV curves at higher rates, the difference between charge and discharge capacities seen for low current rates were due to oxidation of THF. In addition, CV testing at higher rates would reveal if the batteries with Mn_3O_4 cathode starts showing capacitor-like behavior at higher rates.

Lastly, to truly observe what occurs at the cathode surface during operation, XPS should be used as a characterization technique. TEM and XRD have strong electron beams penetrating into particles instead of analyzing the surface. A characterization of only the surface should reveal the reactions occurring during charge and discharge.

Chapter 6

Conclusion

It has been found that as a simple treatment mixing with reduced graphene oxide has a larger effect on the cathode performance of Mn_3O_4 than ball milling the powder. The highest capacity achieved after mixing with reduced graphene oxide was 78 $mAhg^{-1}$. The best performance obtained after milling was 65 $mAhg^{-1}$. From testing of 32 batteries, an active mass dependency was verified, suggesting that a limited amount of the cathode material is used during operation. Still, the batteries with Mn_3O_4 cathode were found to have a long duration, at least 500 cycles, indicating good reversibility. During charge-discharge cycling, it was generally measured higher capacities for charge than discharge at low current rates. The difference is suggested to be owed to oxidation of THF. When it comes to the charge-discharge mechanism, it is suggested, based on ex situ characterization of cathodes, that magnesium attaches on the cathode through a surface reaction.

References

[1] K. Asheim. New materials for Mg-ion batteries. Department for Materials Science and Engineering, NTNU, 2015.

[2] J. Song, E. Sahadeo, M. Noked, and S. B. Lee. Mapping the challenges of magnesium battery. *The Journal of Physical Chemistry Letters*, 7(9):1736–1749, 05 2016.

[3] H. D. Yoo, I. Shterenberg, Y. Gofer, G. Gershinsky, N. Pour, and D. Aurbach. Mg rechargeable batteries: an on-going challenge. *Energy & Environmental Science*, 6(8):2265–2279, 2013.

[4] Q. Wang, P. Ping, X. Zhao, G. Chu, J. Sun, and C. Chen. Thermal runaway caused fire and explosion of lithium ion battery. *Journal of Power Sources*, 208:210–224, 6 2012.

[5] P. Saha, M. K. Datta, O. I. Velikokhatnyi, A. Manivannan, D. Alman, and P. N. Kumta. Rechargeable magnesium battery: Current status and key challenges for the future. *Progress in Materials Science*, 66:1–86, 10 2014.

[6] M. Matsui. Study on electrochemically deposited Mg metal. *Journal of Power Sources*, 196(16):7048–7055, 8 2011.

[7] M-S. Park, J-G. Kim, Y-J. Kim, N-S. Choi, and J-S. Kim. Recent advances in rechargeable magnesium battery technology: A review of the field's current status and prospects. *Israel Journal of Chemistry*, 55(5):570–585, 2015.

[8] M. M. Thackeray. Manganese oxides for lithium batteries. *Progress in Solid State Chemistry*, 25(1–2):1–71, 1997.

[9] David Linden and Thomas B. Reddy. *Handbook of Batteries*. McGraw-Hill, 3rd edition, 2002. Pages 1.3-1.4, 2.20-2.24, 35.1-35.5, 35.9-35.11.

[10] R. S. Nicholson. Theory and application of cyclic voltammetry for measurement of electrode reaction kinetics. *Analytical Chemistry*, 37(11):1351–1355, 10 1965.

[11] A. Burke. Ultracapacitors: why, how, and where is the technology. *Journal of Power Sources*, 91(1):37–50, 11 2000.

[12] G. Yu, L. Hu, N. Liu, H. Wang, M. Vosgueritchian, Y. Yang, Y. Cui, and Z. Bao. Enhancing the supercapacitor performance of graphene/MnO_2 nanostructured electrodes by conductive wrapping. *Nano Letters*, 11(10):4438–4442, 10 2011.

[13] T. D. Gregory, R. J. Hoffman, and R. C. Winterton. Nonaqueous electrochemistry of magnesium: Applications to energy storage. *Journal of The Electrochemical Society*, 137(3):775–780, 1990.

[14] A. P. Syvetsen. Alloys as anode materials in magnesium ion batteries. Master's thesis, Norwegian University of Science and Technology, 2012.

[15] I. Yoshimatsu, T. Hirai, and J. Yamaki. Lithium electrode morphology during cycling in lithium cells. *Journal of The Electrochemical Society*, 135(10):2422–2427, 10 1988.

[16] H. Kim, G. Jeong, Y-U. Kim, J-H. Kim, C-M. Park, and H-J. Sohn. Metallic anodes for next generation secondary batteries. *Chemical Society Reviews*, 42(23):9011–9034, 2013.

[17] C. Ling, D. Banerjee, and M. Matsui. Study of the electrochemical deposition of Mg in the atomic level: Why it prefers the non-dendritic morphology. *Electrochimica Acta*, 76:270–274, 8 2012.

[18] D. Aurbach, Z. Lu, A. Schechter, Y. Gofer, H. Gizbar, R. Turgeman, Y. Cohen, M. Moshkovich, and E. Levi. Prototype systems for rechargeable magnesium batteries. *Nature*, 407(6805):724–727, 10 2000.

[19] D. Aurbach, G. S. Suresh, E. Levi, A. Mitelman, O. Mizrahi, O. Chusid, and M. Brunelli. Progress in rechargeable magnesium battery technology. *Advanced Materials*, 19(23):4260 – 4267, 2007.

[20] P. Canepa, G. S. Gautam, R. Malik, S. Jayaraman, Z. Rong, K. R. Zavadil, K. Persson, and G. Ceder. Understanding the initial stages of reversible Mg deposition and stripping in inorganic nonaqueous electrolytes. *Chemistry of Materials*, 27(9):3317–3325, 2015.

[21] Sigma aldrich. http://www.sigmaaldrich.com/catalog/product/sial/401757?lang=en&region=NO, June 2016.

[22] J. Muldoon, C. B. Bucur, A. G. Oliver, J. Zajicek, G. D. Allred, and W. C. Boggess. Corrosion of magnesium electrolytes: chlorides - the culprit. *Energy & Environmental Science*, 6(2):482–487, 2013.

[23] Y.-s. Guo, F. Zhang, J. Yang, F.-f. Wang, Y. NuLi, and S.-i. Hirano. Boron-based electrolyte solutions with wide electrochemical windows for rechargeable magnesium batteries. *Energy & Environmental Science*, 5(10):9100–9106, 2012.

[24] D. Lv, T. Xu, P. Saha, M. K. Datta, M. L. Gordin, A. Manivannan, P. N. Kumta, and D. Wang. A scientific study of current collectors for Mg batteries in $Mg(AlCl_2EtBu)_{2/}THF$ electrolyte. *Journal of The Electrochemical Society*, 160(2):A351–A355, 2013.

[25] L. Wang, K. Asheim, A. M. Svensson, P. E. Vullum, and F. Vullum-Bruer. Sponge-like porous manganese(ll,lll) oxide as a highly efficient cathode material for rechargeable magnesium ion batteries. Depertment of Materials Science and Engineering, Norwegian University of Science and Technology, NO-7491 Trondheim, Norway.

[26] R. Shannon. Revised effective ionic radii and systematic studies of interatomic distances in halides and chalcogenides. 32(5):751–767, 1976.

[27] T. Aylward, G. Findlay. *SI Chemical Data*. John Wiley & Sons Australia, Ltd, 6th edition, 2008.

[28] E. Levi, Y Gofer, and D. Aurbach. On the way to rechargeable Mg batteries: The challenge of new cathode materials. *Chemistry of Materials*, 22(3):860–868, 02 2010.

[29] Y. Zheng, Y. NuLi, Q. Chen, Y. Wang, J. Yang, and J. Wang. Magnesium cobalt silicate materials for reversible magnesium ion storage. *Electrochimica Acta*, 66:75–81, 4 2012.

[30] H. Zhou, M.-A. Einarsrud, and F. Vullum-Bruer. High capacity nanostructured $Li_2Fe_xSiO_{4/}C$ with Fe hyperstoichiometry for Li-ion batteries. *Journal of Power Sources*, 235:234–242, 8 2013.

[31] E. Levi, M. D. Levi, O. Chasid, and D. Aurbach. A review on the problems of the solid state ions diffusion in cathodes for rechargeable mg batteries. *Journal of Electroceramics*, 22(1):13–19, 2009.

[32] A. R. West. *Solid State Chemistry and its applications*. Wiley, 2 edition, 2014. Pages 66-68, 183-184.

[33] A. Yamada, M. Tanaka, K. Tanaka, and K. Sekai. Jahn-teller instability in spinel Li−Mn−O. *Journal of Power Sources*, 81–82:73–78, 9 1999.

[34] C. S. Johnson. Development and utility of manganese oxides as cathodes in lithium batteries. *Journal of Power Sources*, 165(2):559–565, 3 2007.

[35] R. Zhang, X. Yu, K.-W. Nam, C. Ling, T. S. Arthur, W. Song, A. M. Knapp, S. N. Ehrlich, X.-Q. Yang, and M. Matsui. $\alpha-MnO_2$ as a cathode material for rechargeable Mg batteries. *Electrochemistry Communications*, 23:110–113, 9 2012.

[36] T. S. Arthur, R. Zhang, C. Ling, P.-A. Glans, X. Fan, J. Guo, and F. Mizuno. Understanding the electrochemical mechanism of $K-\alpha MnO_2$ for magnesium battery cathodes. *ACS Applied Materials & Interfaces*, 6(10):7004–7008, 05 2014.

[37] C. Ling, R. Zhang, and F. Mizuno. Quantitatively predict the potential of MnO_2 polymorphs as magnesium battery cathodes. *ACS Applied Materials & Interfaces*, 8(7):4508–4515, 02 2016.

[38] C. Ling, R. G. Zhang, T. S. Arthur, and F. Mizuno. How general is the conversion reaction in Mg ion battery cathode: A case study of the magnesiation of $\boldsymbol{\alpha}$-MnO_2. *Chemistry of Materials*, 27(16):5799–5807, 2015.

[39] R. Zhang, T. S. Arthur, C. Ling, and F. Mizuno. Manganese dioxides as rechargeable magnesium battery cathode; synthetic approach to understand magnesiation process. *Journal of Power Sources*, 282:630–638, 5 2015.

[40] C. Yuan, Y. Zhang, Y. Pan, X. Liu, G. Wang, and D. Cao. Investigation of the intercalation of polyvalent cations (Mg^{2+}, Zn^{2+}) into $\boldsymbol{\gamma}$-MnO_2 for rechargeable aqueous battery. *Electrochimica Acta*, 116:404–412, 1 2014.

[41] R. J. D. Tilley. *Understanding Solids - The Science of Materials*. Wiley, 2 edition, 2013. Pages 125-126.

[42] C. Kim, P. J. Phillips, B. Key, T. Yi, D. Nordlund, Y.-S. Yu, R. D. Bayliss, S.-D. Han, M. He, Z. Zhang, A. K. Burrell, R. F. Klie, and J. Cabana. Direct observation of reversible magnesium ion intercalation into a spinel oxide host. *Advanced Materials*, 27(22):3377–3384, 2015.

[43] L. Ben Said, T. Larbi, A. Yumak, K. Boubaker, and M. Amlouk. Pure and zirconium-doped manganese(ll,lll) oxide: Investigations on structural and conduction-related properties within the lattice compatibility theory scope. *Materials Science in Semiconductor Processing*, 40:224–229, 12 2015.

[44] P. Atkins, T. Overton, J. Rourke, M. Weller, and F. Armstrong. *Shriver & Atkins' Inorganic Chemistry*. Oxford University Press, 5 edition, 2010. Pages 70-71.

[45] ZS. Wu, CW. Wang, W. Ren, J. Zhao, G. Zhou, F. Li, and HM. Cheng. Anchoring hydrous RuO_2 on graphene sheets for high-performance electrochemical capacitors. *Advanced functional materials*, 20(20):3595–3602, 2010.

[46] W. Zhang, F. Liu, Q. Li, Q. Shou, J. Cheng, L. Zhang, B. J. Nelson, and X. Zhang. Transition metal oxide and graphene nanocomposites for high-performance electrochemical capacitors. *Physical Chemistry Chemical Physics*, 14(47):16331–16337, 2012.

[47] G. Jin, X. Xiao, S. Li, K. Zhao, Y. Wu, D. Sun, and F. Wang. Strongly coupled graphene/Mn_3O_4 composite with enhanced electrochemical performance for supercapacitor electrode. *Electrochimica Acta*, 178:689–698, 10 2015.

[48] R. E. Doe, R. Han, J. Hwang, A. J. Gmitter, I. Shterenberg, H. D. Yoo, N. Pour, and D. Aurbach. Novel, electrolyte solutions comprising fully inorganic salts with high

anodic stability for rechargeable magnesium batteries. *Chemical Communications*, 50(2):243–245, 2014.

[49] T. Liu, Y. Shao, G. Li, M. Gu, J. Hu, S. Xu, Z. Nie, X. Chen, C. Wang, and J. Liu. A facile approach using $MgCl_2$ to formulate high performance Mg^{2+} electrolytes for rechargeable mg batteries. *Journal of Materials Chemistry A*, 2(10):3430–3438, 2014.

[50] C. J. Barile, E. C. Barile, K. R. Zavadil, R. G. Nuzzo, and A. A. Gewirth. Electrolytic conditioning of a magnesium aluminum chloride complex for reversible magnesium deposition. *The Journal of Physical Chemistry C*, 118(48):27623–27630, 12 2014.

[51] K. A. See, K. W. Chapman, L. Zhu, K. M. Wiaderek, O. J. Borkiewicz, C. J. Barile, P. J. Chupas, and A. A. Gewirth. The interplay of Al and Mg speciation in advanced Mg battery electrolyte solutions. *Journal of the American Chemical Society*, 138(1):328–337, 01 2016.

[52] C. J. Barile, R. Spatney, K. R. Zavadil, and A. A. Gewirth. Investigating the reversibility of in situ generated magnesium organohaloaluminates for magnesium deposition and dissolution. *The Journal of Physical Chemistry C*, 118(20):10694–10699, 05 2014.

[53] D. W. Richerson. *Modern Ceramic Engineering - Properties, Processing and Use in Design*. CRC Press, Taylor & Francis Group, 3rd edition, 2006. Page 380.

[54] Ø. Gullbrekken. Thermal characterisation of anode materials for Li-ion batteries. Master's thesis, Norwegian University of Science and Technology, 2012.

[55] S. Lowell, J. E. Shields, M. A. Thomas, and M. Thommes. *Characterization of Porous Solids and Powders: Surface Area, Pore Size and Density*. Kluwer Academic Publishers, 2004. Pages 11-13.

Appendix A

Charge-discharge

A.1 Not milled Mn_3O_4

Charge-discharge curves for the cathodes of not milled Mn_3O_4 cycled at 0.1C that were not presented in the results section are given here. Hence, these cathodes have capacities between 50 and 24 $mAh\,g^{-1}$, and they are presented here with decreasing capacity in Figure A.1 - A.7.

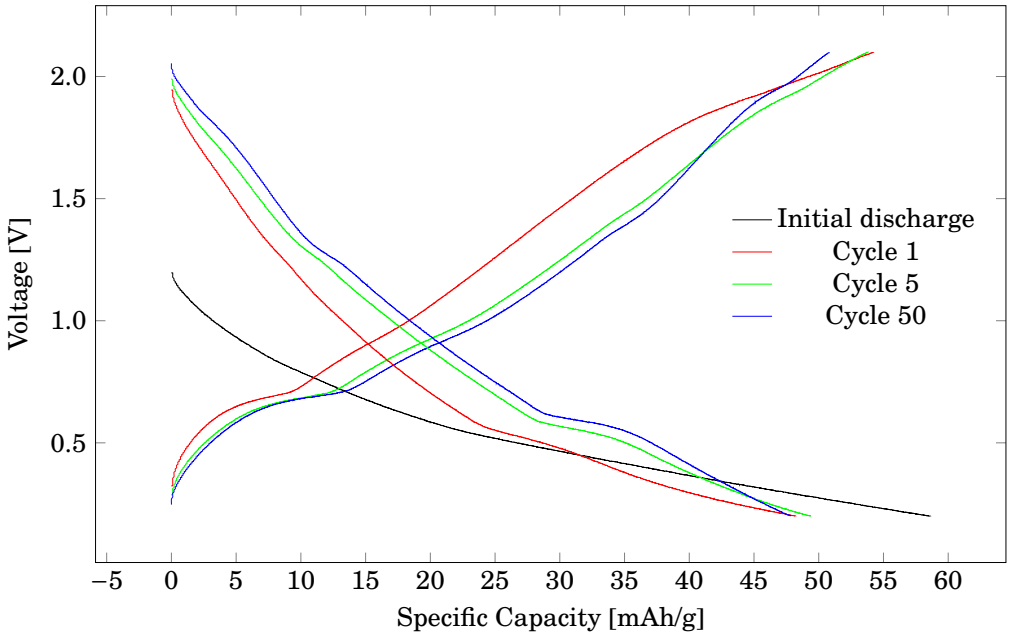

Figure A.1: Charge-discharge curves for cathode of not milled Mn_3O_4, showing the initial discharge (black line), cycle 1 (red lines), cycle 5 (green lines) and cycle 50 (blue lines). The average specific capacity obtained was 49 $mAh\,g^{-1}$, and the cathode's active mass was 1.2 mg. 7 % decrease in capacity from initial discharge to first charge.

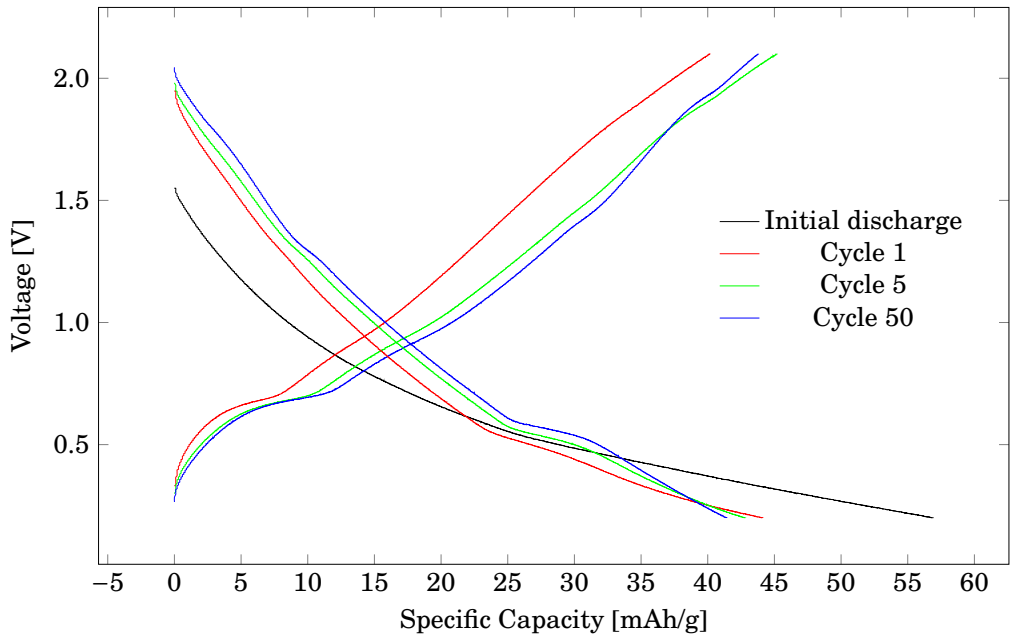

Figure A.2: Charge-discharge curves for cathode of not milled Mn_3O_4. The average specific capacity obtained was 43 $mAh\,g^{-1}$, and the cathode's active mass was 1.44 mg.

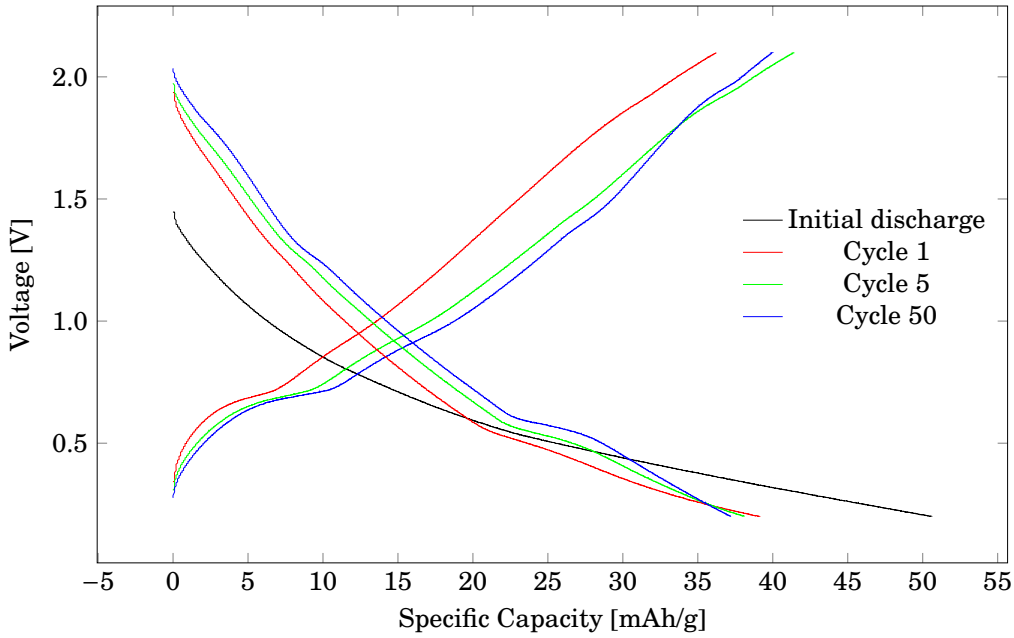

Figure A.3: Charge-discharge curves for cathode of not milled Mn_3O_4. The average specific capacity obtained was 38 $mAh\,g^{-1}$, and the cathode's active mass was 1.76 mg.

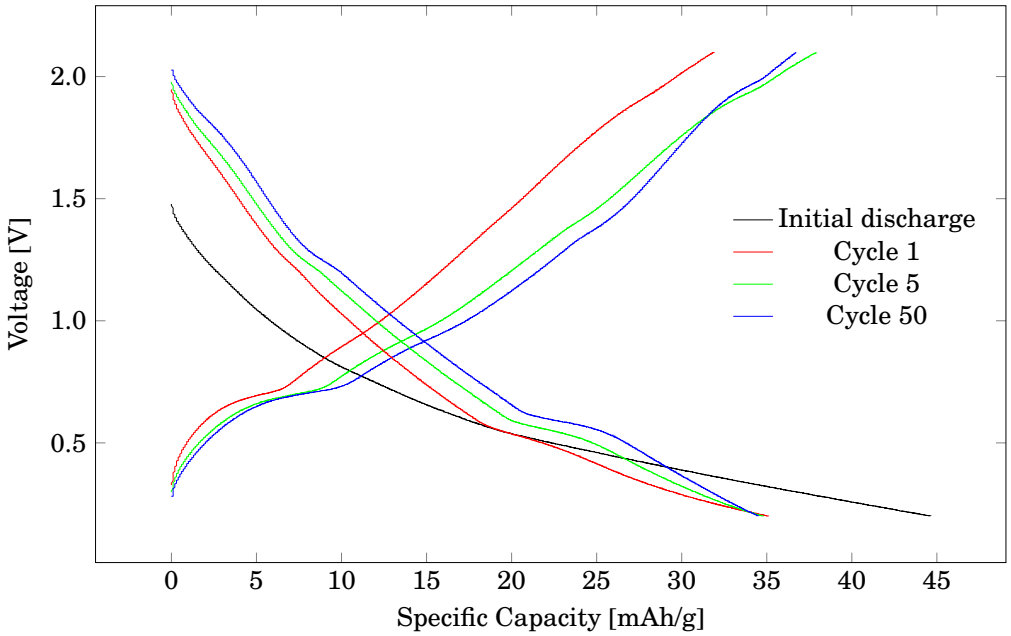

Figure A.4: Charge-discharge curves for cathode of not milled Mn_3O_4. The average specific capacity obtained was 36 $mAh\,g^{-1}$, and the cathode's active mass was 1.52 mg.

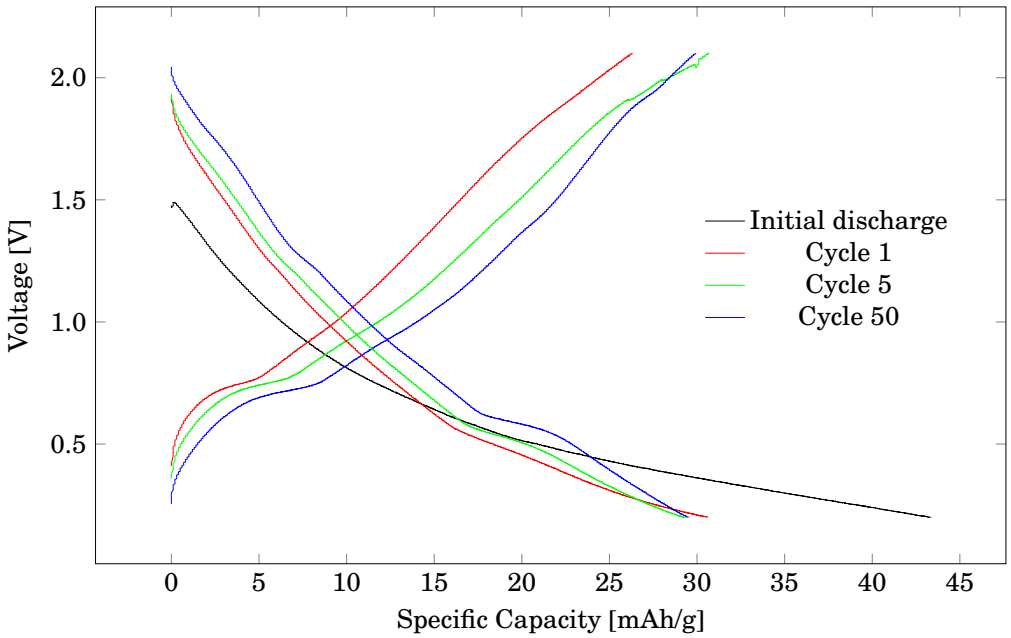

Figure A.5: Charge-discharge curves for cathode of not milled Mn_3O_4. The average specific capacity obtained was 30 $mAh\,g^{-1}$, and the cathode's active mass was 2.16 mg. Collected from [1].

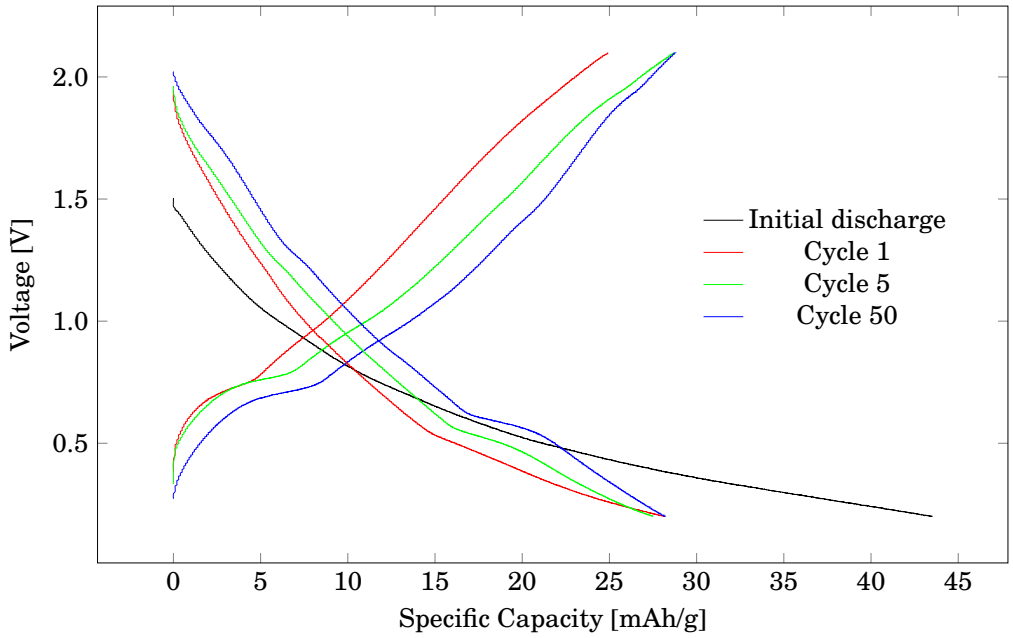

Figure A.6: Charge-discharge curves for cathode of not milled Mn_3O_4. The average specific capacity was 28 $mAh\,g^{-1}$, and the cathode's active mass was 2.48 mg. Collected from [1].

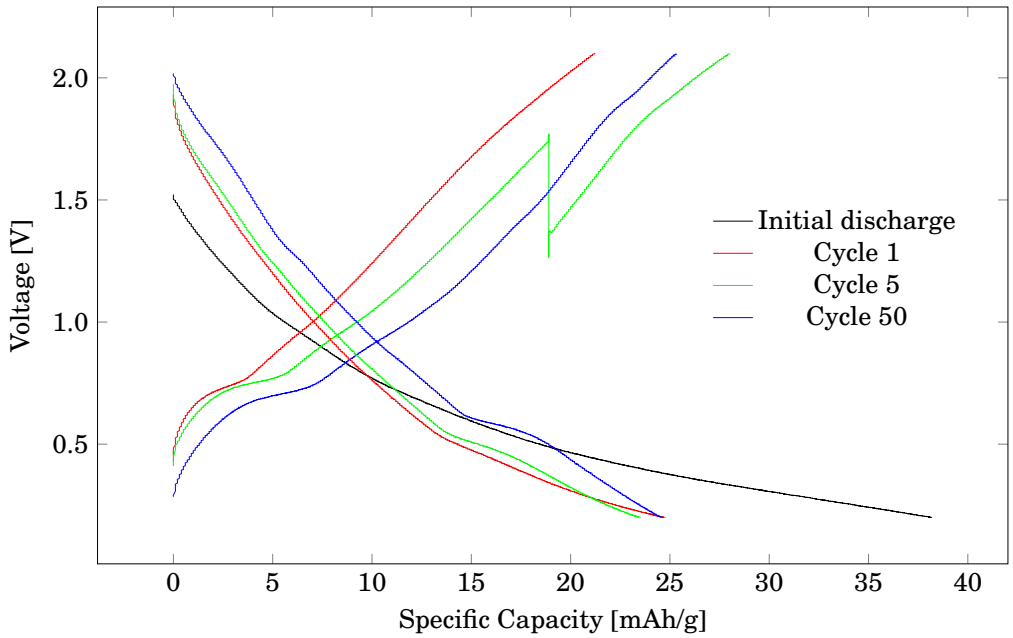

Figure A.7: Charge-discharge curves for cathode of not milled Mn_3O_4. The average specific capacity obtained was 25 $mAh\,g^{-1}$, and the cathode's active mass was 2.72 mg. The sudden drop in voltage during charge in cycle 5 is owed to the test machine turning itself off and not being started again until hours later. Collected from [1].

A.2 Milled Mn_3O_4

Charge-discharge curves for the cathodes of milled Mn_3O_4 cycled at 0.1C not presented in the results section are given in the following Figures A.8 - A.13. Their obtained capacities are between 65 and 33 $mAh\,g^{-1}$, and they are presented in the order of decreasing capacity.

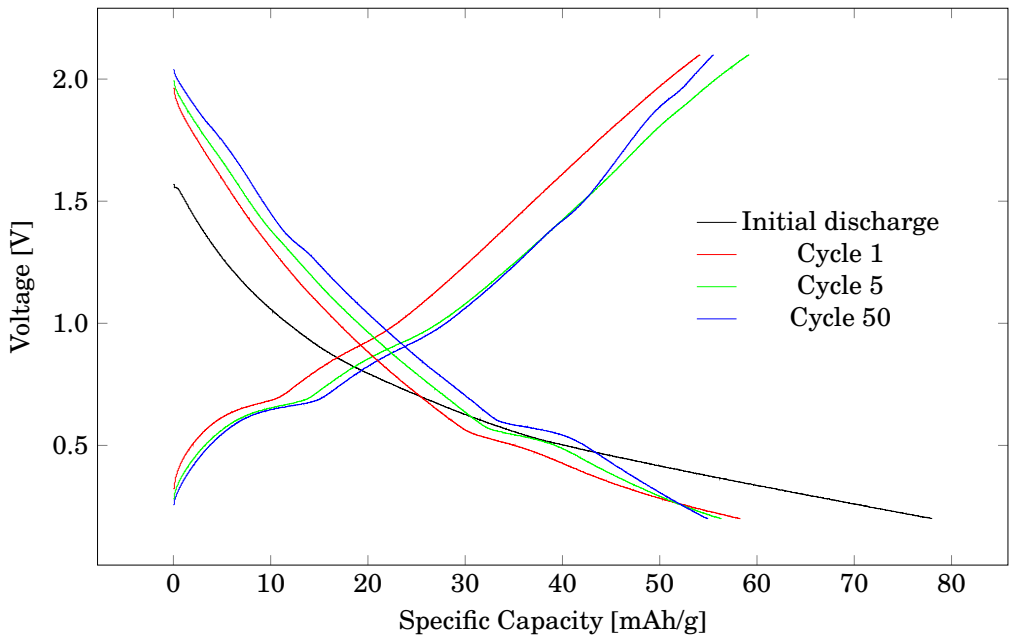

Figure A.8: Charge-discharge curves for cathode of milled Mn_3O_4. The average specific capacity obtained was 56 $mAh\,g^{-1}$, and the cathode's active mass was 1.12 mg.

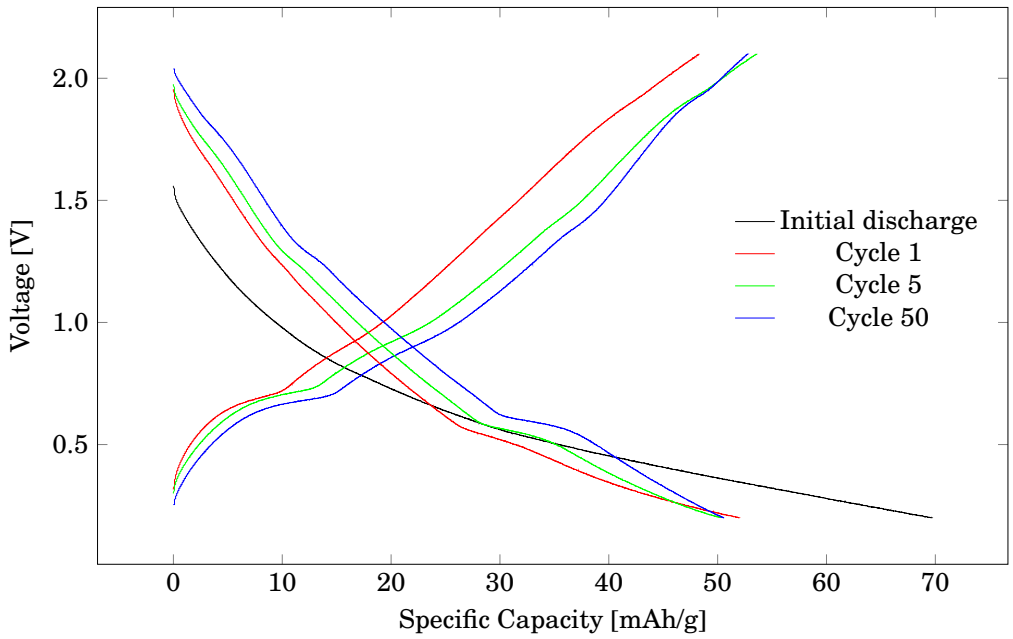

Figure A.9: Charge-discharge curves for cathode of milled Mn_3O_4. The average specific capacity obtained was 51 $mAh\,g^{-1}$, and the cathode's active mass was 1.28 mg.

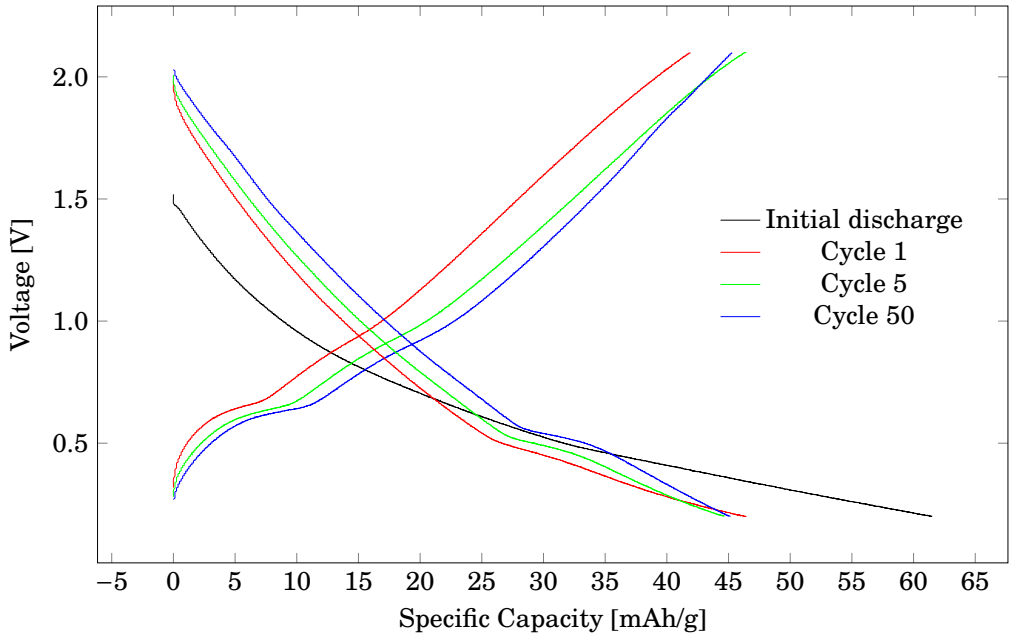

Figure A.10: Charge-discharge curves for cathode of milled Mn_3O_4. The average specific capacity obtained was 45 $mAh\,g^{-1}$, and the cathode's active mass was 1.36 mg.

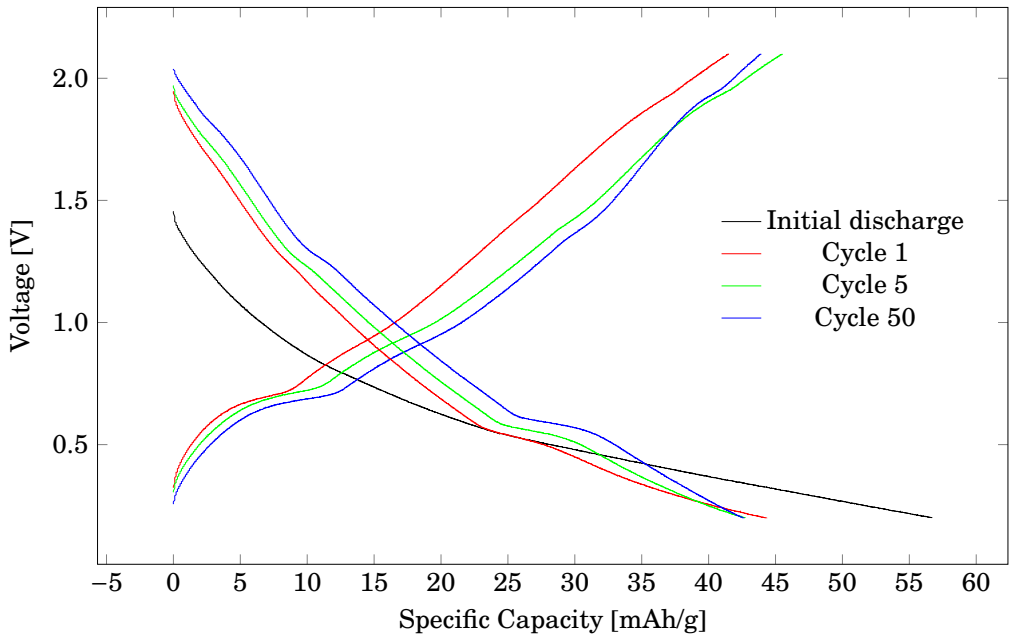

Figure A.11: Charge-discharge curves for cathode of milled Mn_3O_4. The average specific capacity obtained was 43 $mAh\,g^{-1}$, and the cathode's active mass was 1.44 mg.

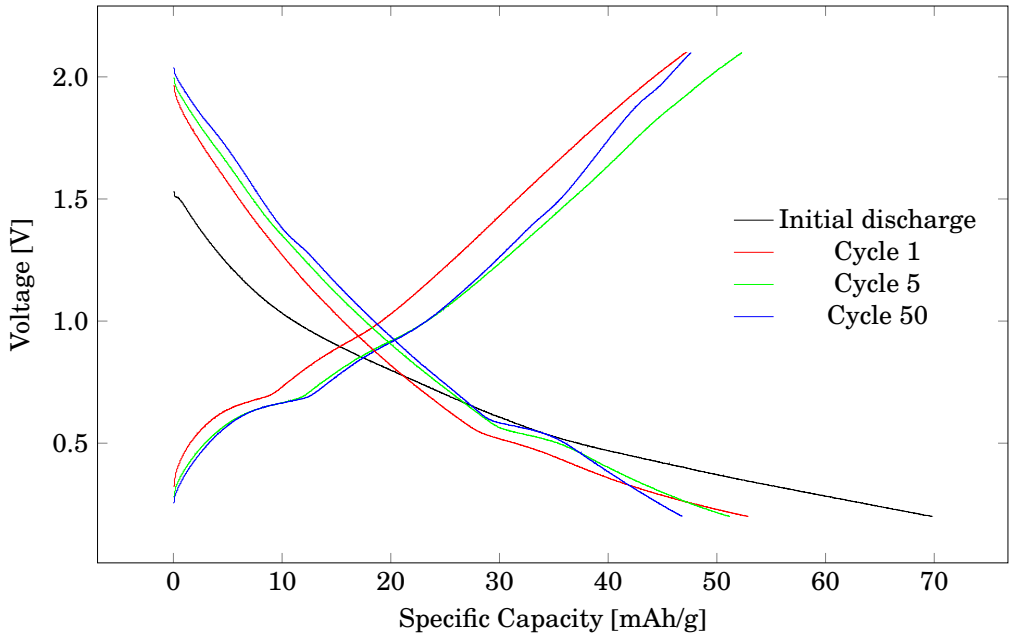

Figure A.12: Charge-discharge curves for cathode of milled Mn_3O_4. The average specific capacity obtained was 42 $mAh\,g^{-1}$, and the cathode's active mass was 1.52 mg.

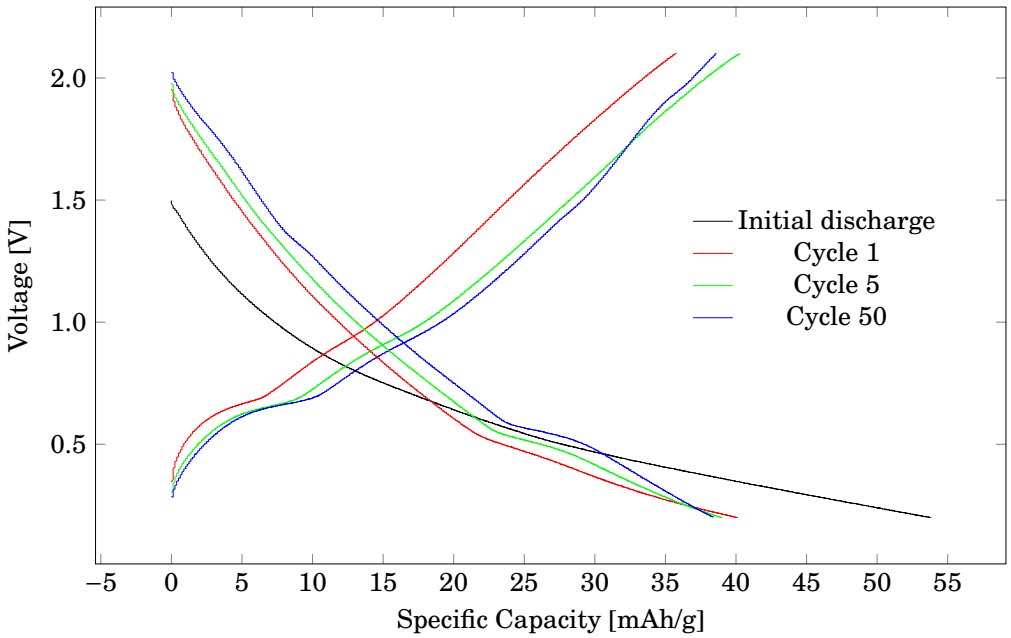

Figure A.13: Charge-discharge curves for cathode of milled Mn_3O_4. The average specific capacity obtained was 39 $mAh\,g^{-1}$, and the cathode's active mass was 1.6 mg.

A.3 Not milled Mn_3O_4 with RGO

Charge-discharge curves for the cathodes of not milled Mn_3O_4 with RGO cycled at 0.1C not presented in the results section are given below. Their obtained capacities are between 77 and 32 $mAh\,g^{-1}$. The cathodes will be presented in the order of decreasing capacity in Figure A.14 - A.18.

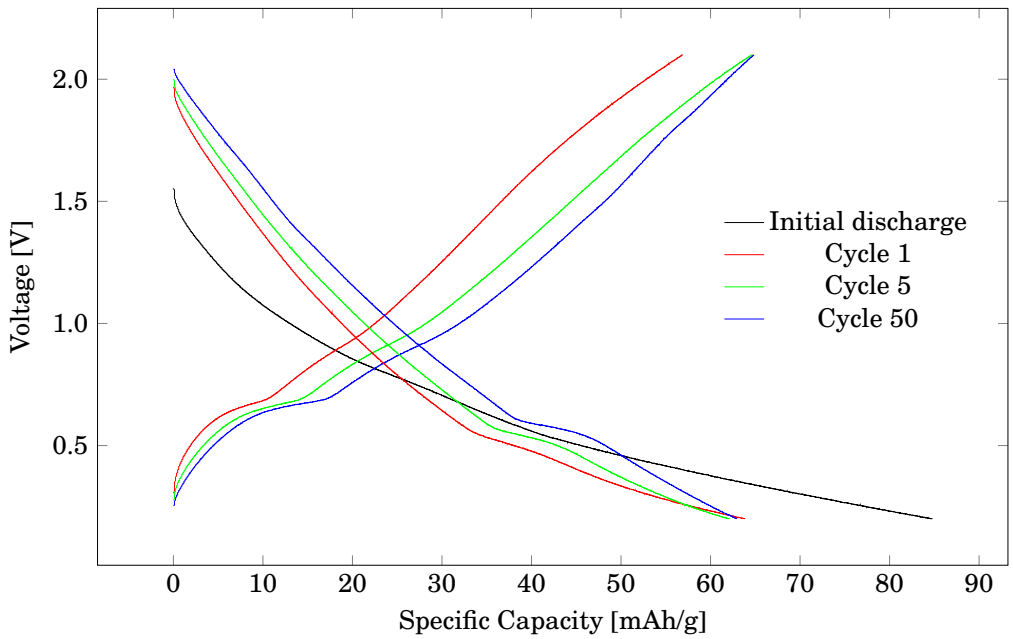

Figure A.14: Charge-discharge curves for cathode of not milled Mn_3O_4 with RGO. The average specific capacity obtained was 62 $mAh\,g^{-1}$, and the cathode's active mass was 1.22 mg. Modified from [1].

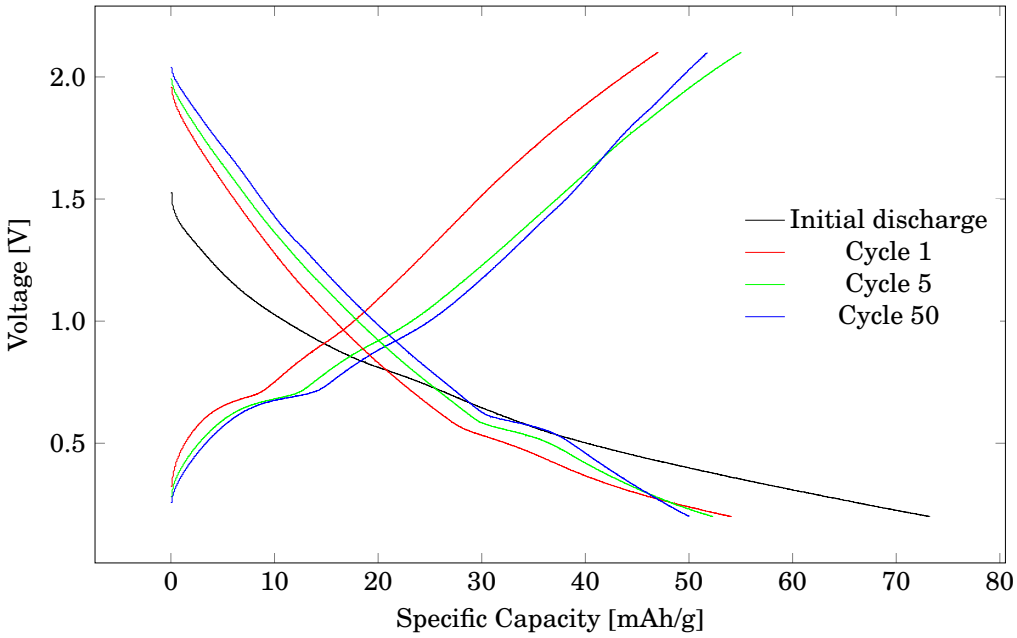

Figure A.15: Charge-discharge curves for cathode of not milled Mn_3O_4 with RGO. The average specific capacity obtained was 53 $mAh\,g^{-1}$, and the cathode's active mass was 1.5 mg. Modified from [1].

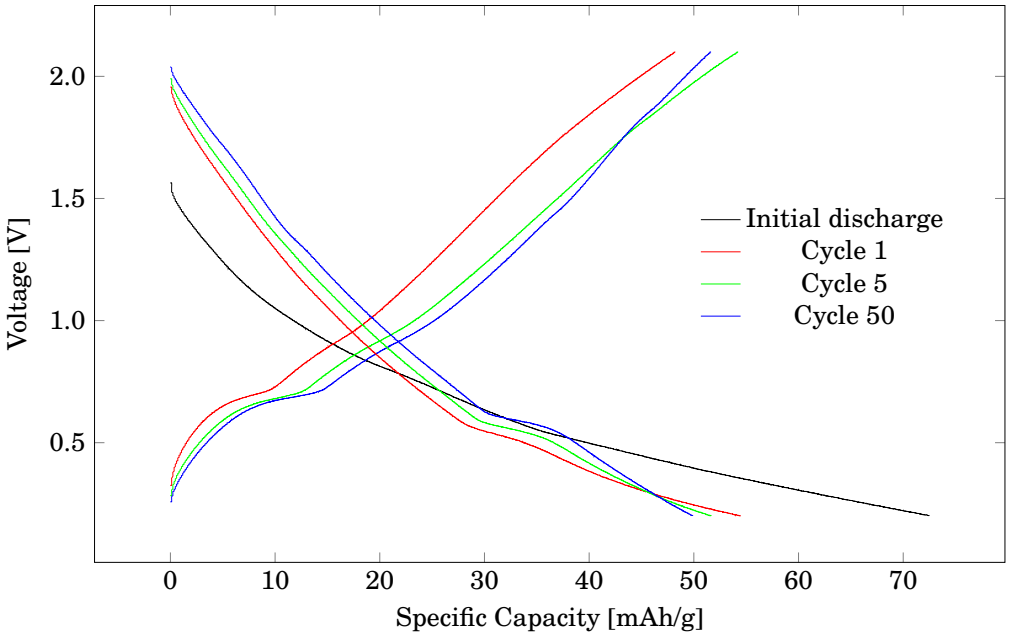

Figure A.16: Charge-discharge curves for cathode of not milled Mn_3O_4 with RGO. The average specific capacity obtained was 52 $mAh\,g^{-1}$, and the cathode's active mass was 1.36 mg. Modified from [1].

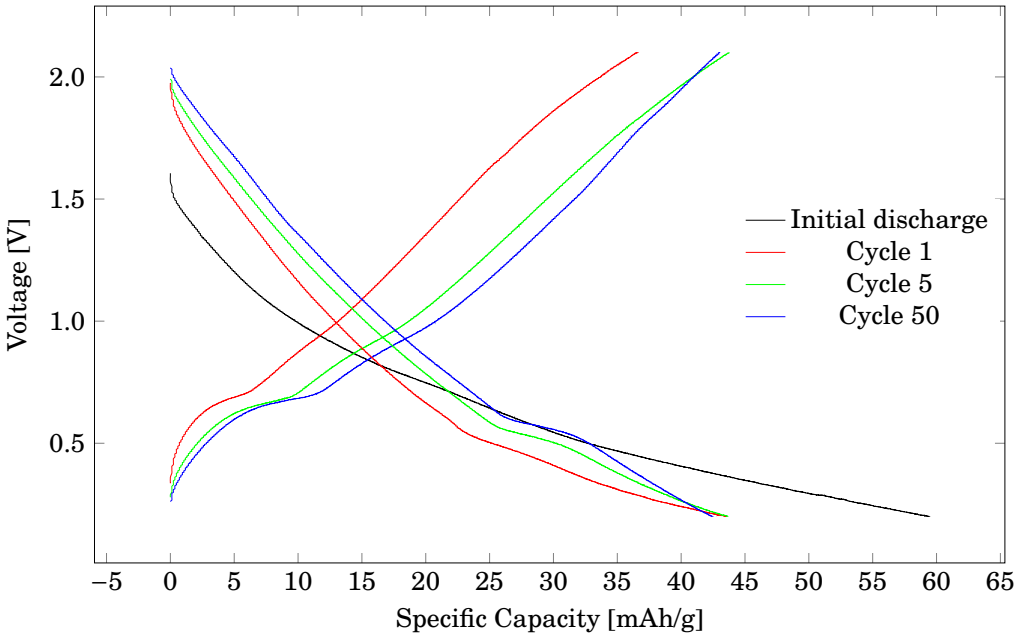

Figure A.17: Charge-discharge curves for cathode of not milled Mn_3O_4 with RGO. The average specific capacity obtained was 42 $mAh\,g^{-1}$, and the cathode's active mass was 1.7 mg. Modified from [1].

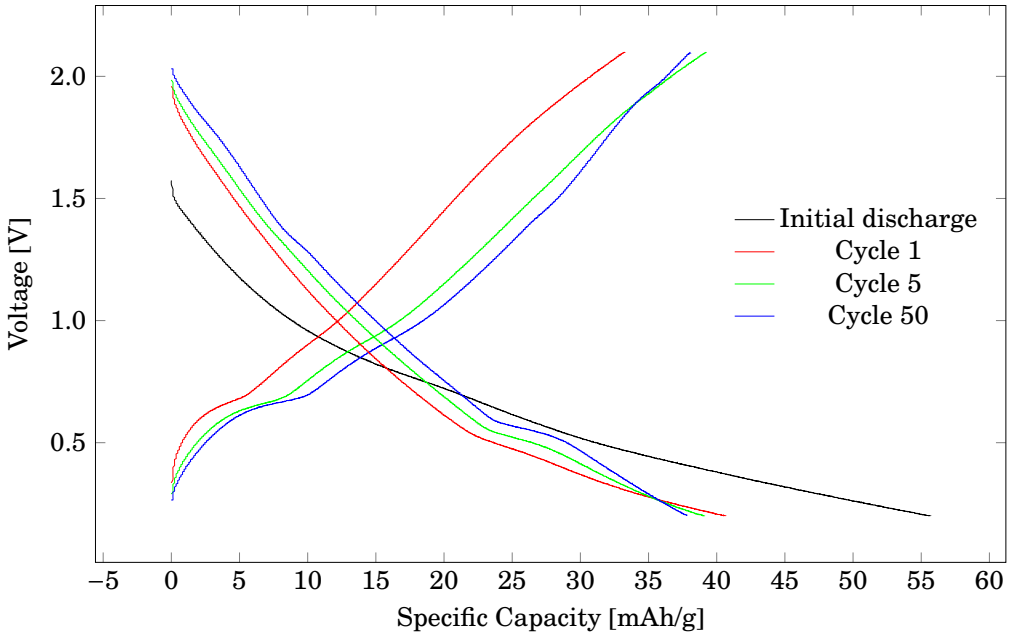

Figure A.18: Charge-discharge curves for cathode of not milled Mn_3O_4 with RGO. The average specific capacity obtained was 39 $mAh\,g^{-1}$, and the cathode's active mass was 1.84 mg.

A.4 Milled Mn_3O_4 with RGO

Charge-discharge curves for cathodes of milled Mn_3O_4 with RGO cycled at 0.1C not presented in the results section are given here. These cathodes achieved capacities between 60 and 26 $mAh\,g^{-1}$, and are presented in the order of decreasing capacity in Figure A.19 - A.24.

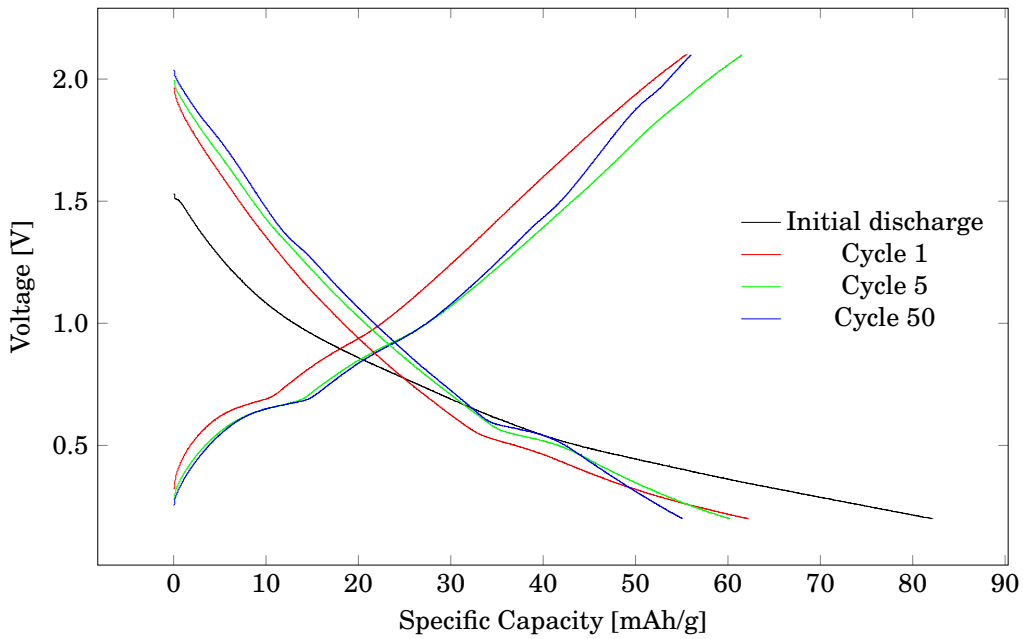

Figure A.19: Charge-discharge curves for cathode of milled Mn_3O_4 with RGO. The average specific capacity obtained was 59 $mAh\,g^{-1}$, and the cathode's active mass was 1.36 mg.

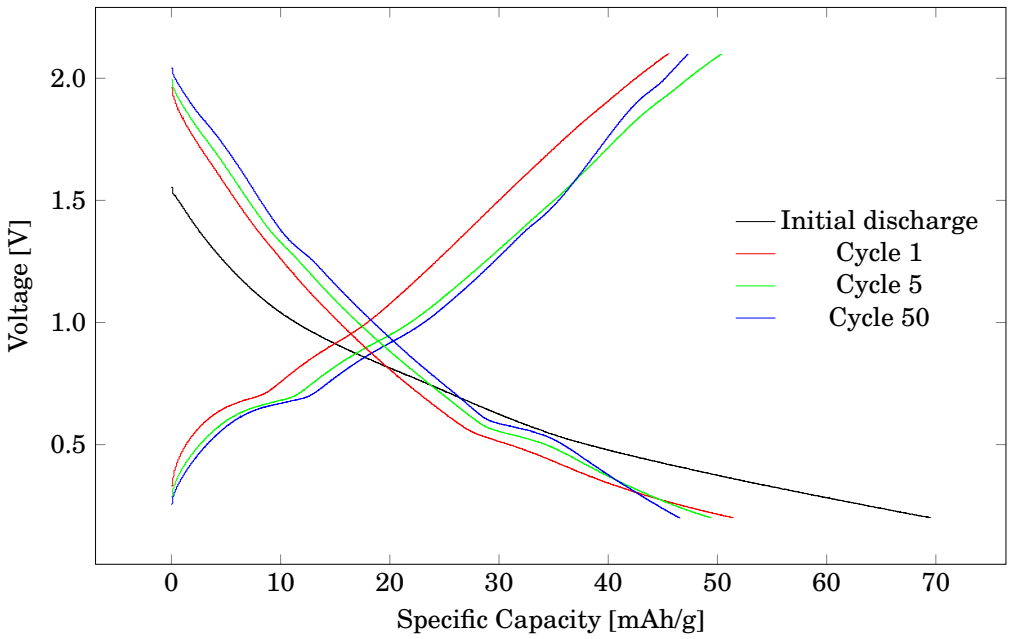

Figure A.20: Charge-discharge curves for cathode of milled Mn_3O_4 with RGO. The average specific capacity obtained was 49 $mAh\,g^{-1}$, and the cathode's active mass was 1.56 mg.

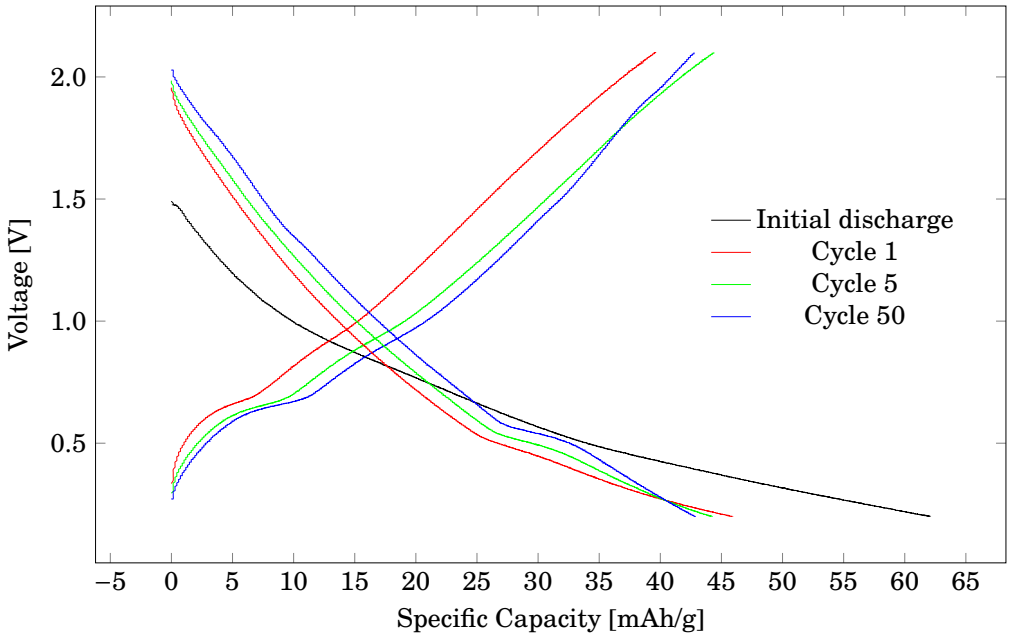

Figure A.21: Charge-discharge curves for cathode of milled Mn_3O_4 with RGO. The average specific capacity obtained was 44 $mAh\,g^{-1}$, and the cathode's active mass was 1.56 mg.

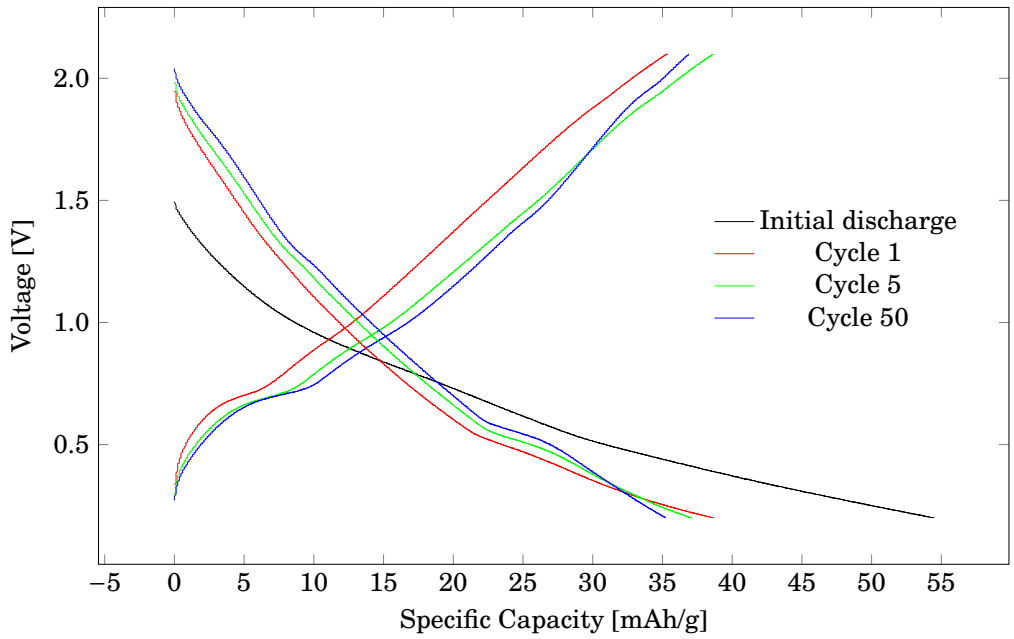

Figure A.22: Charge-discharge curves for cathode of milled Mn_3O_4 with RGO. The average specific capacity obtained was 37 $mAh\,g^{-1}$, and the cathode's active mass was 1.97 mg.

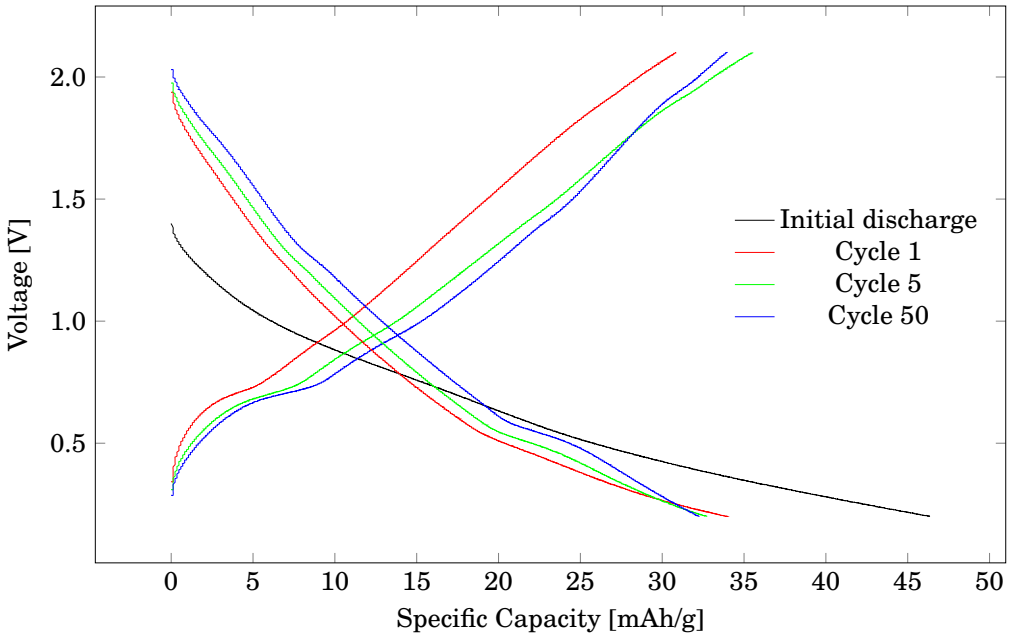

Figure A.23: Charge-discharge curves for cathode of milled Mn_3O_4 with RGO. The average specific capacity obtained was 33 $mAh\,g^{-1}$, and the cathode's active mass was 2.04 mg.

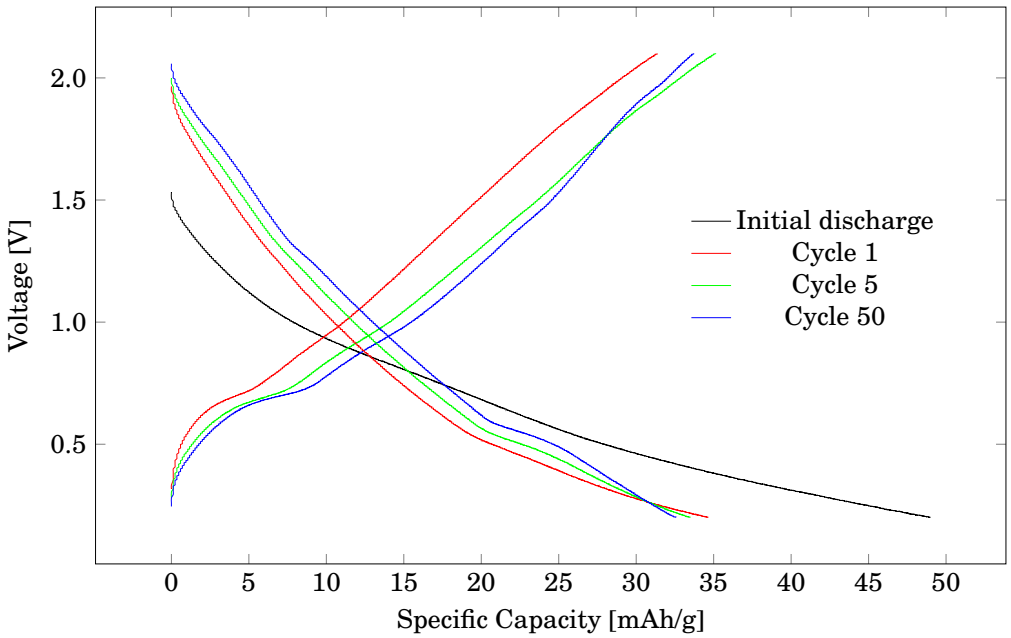

Figure A.24: Charge-discharge curves for cathode of milled Mn_3O_4 with RGO. The average specific capacity obtained was 33 $mA\,h\,g^{-1}$, and the cathode's active mass was 2.18 mg.

Appendix B

Long term performance

The two cathodes long term cycled to less than 500 cycles at 0.1C are presented here instead of in the results section. The first of these cathodes was of milled Mn_3O_4 with RGO and was cycled 400 times. The second cathodes was of pure, milled Mn_3O_4 and was cycled 300 times. The cathodes are given with charge-discharge curves and capacity development during cycling in Figures B.1 - B.4.

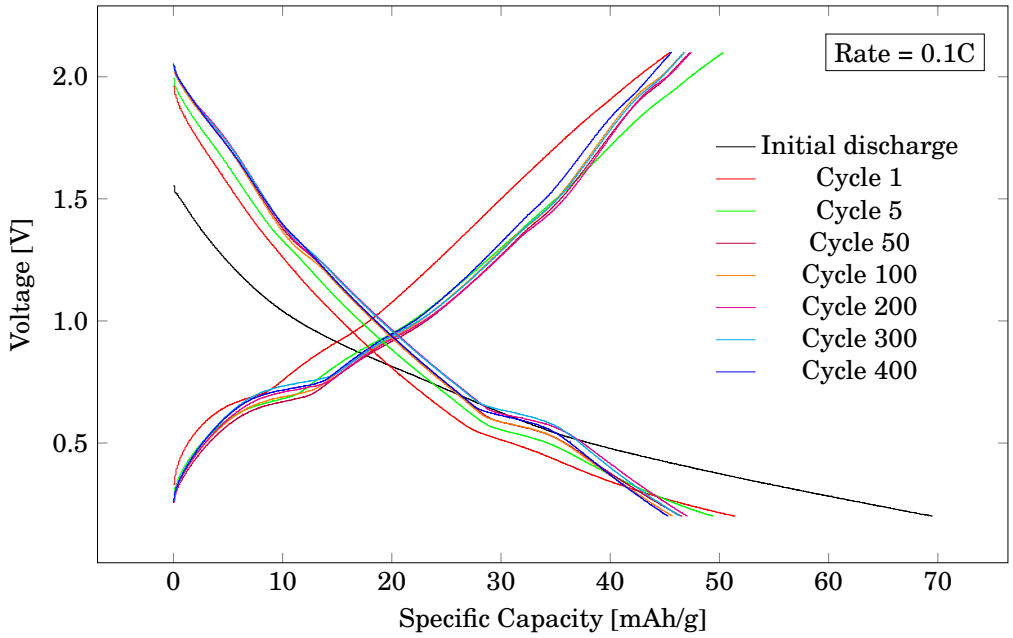

Figure B.1: Charge-discharge curves for cathode of milled Mn_3O_4 with RGO cycled 400 times. The average specific capacity obtained was 46 $mAh\,g^{-1}$, and the cathode's active mass was 1.56 mg. Total cycling time was approximately 83 days.

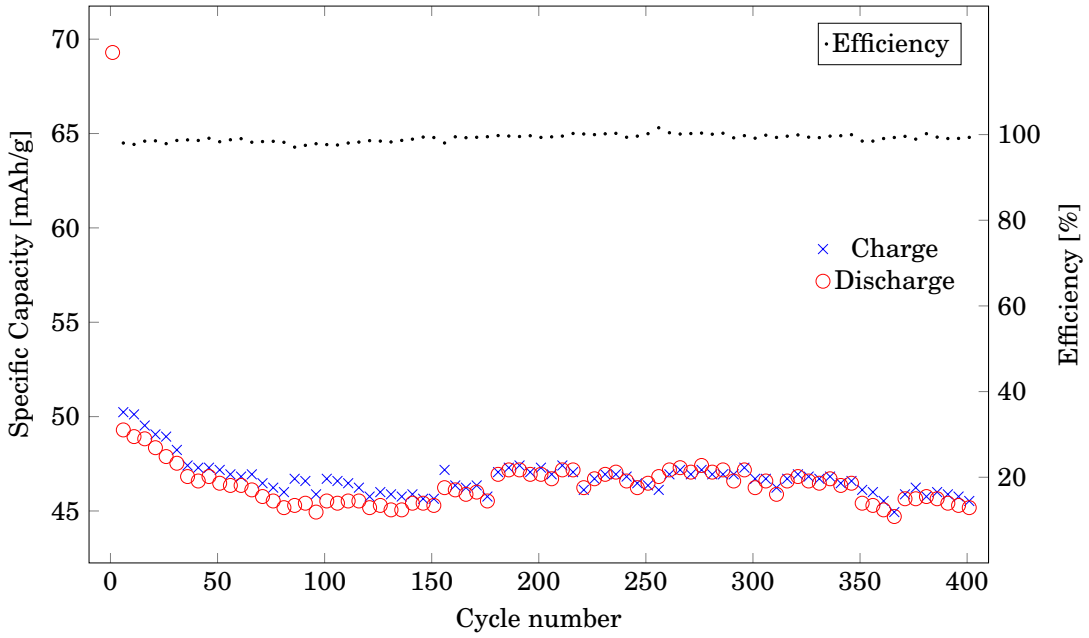

Figure B.2: Charge and discharge capacities for cathode of milled Mn_3O_4 with RGO cycled 400 times. The average specific capacity during the 400 cycles was 46 $mAh\,g^{-1}$, and the cathode's active mass was 1.56 mg.

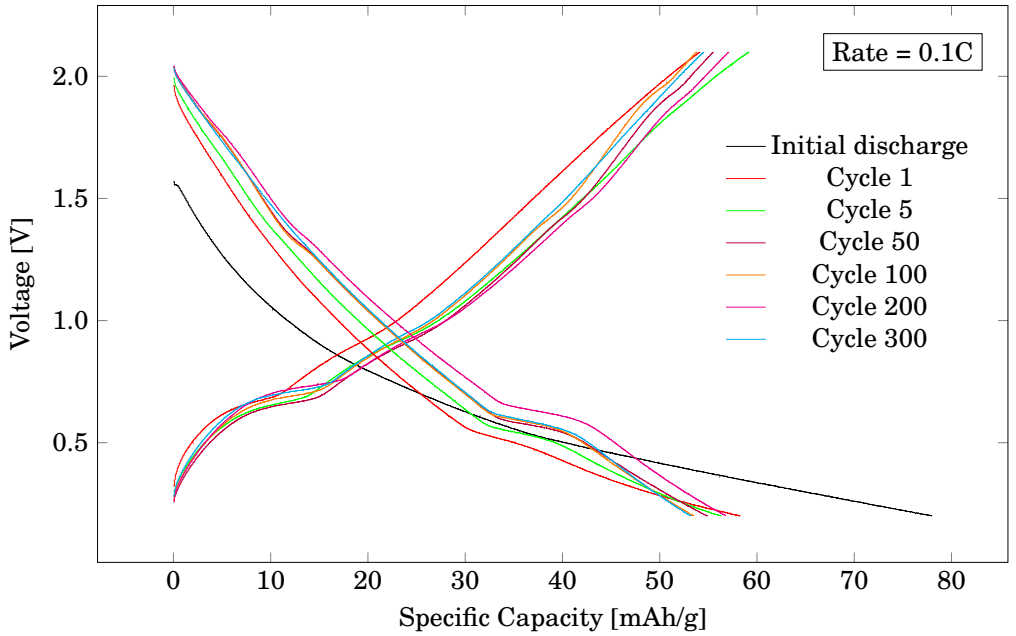

Figure B.3: Charge-discharge curves for cathode of pure, milled Mn_3O_4 cycled 300 times. The average specific capacity obtained was 56 $mAh\,g^{-1}$, and the cathode's active mass was 1.12 mg. Total cycling time was approximately 88 days.

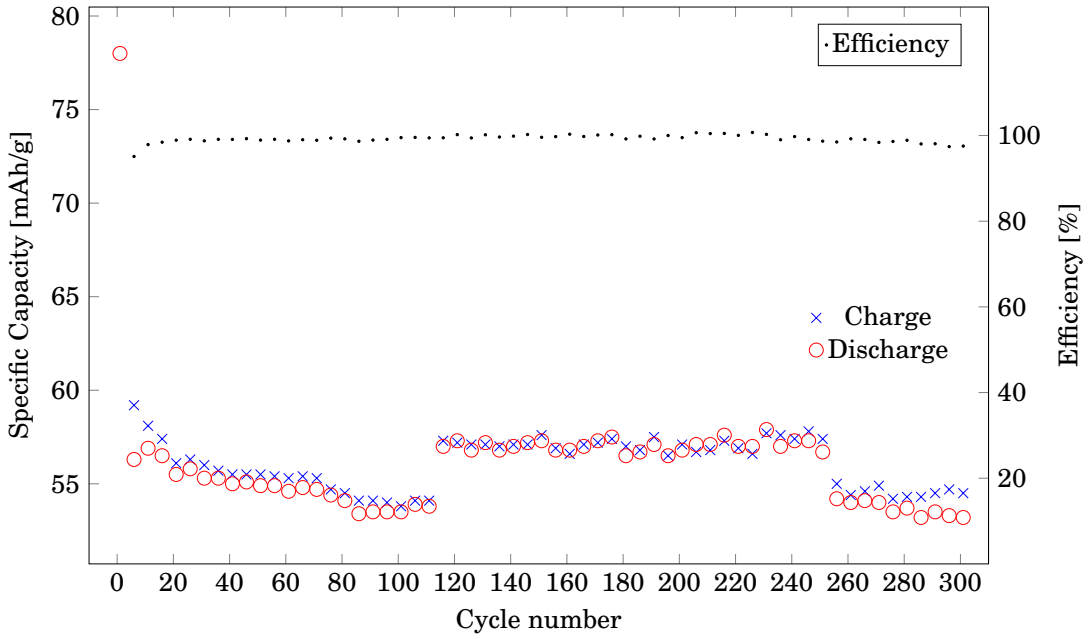

Figure B.4: Charge and discharge capacities for cathode of pure, milled Mn_3O_4 cycled 300 times. The average specific capacity obtained was 56 $mAh\,g^{-1}$, and the cathode's active mass was 1.12 mg.

Appendix C

Rate capability

The three cathodes that had their rate cyclic performance tested, but was not presented in the results section, are given here. One of these was a cathode of pure, milled Mn_3O_4 and other two were of milled Mn_3O_4 with RGO. The cathode of pure, milled Mn_3O_4 are presented first in Figure C.1, followed by the two of milled Mn_3O_4 with RGO in the order of decreasing capacity in Figures C.2 and C.3.

C.1 Milled Mn_3O_4

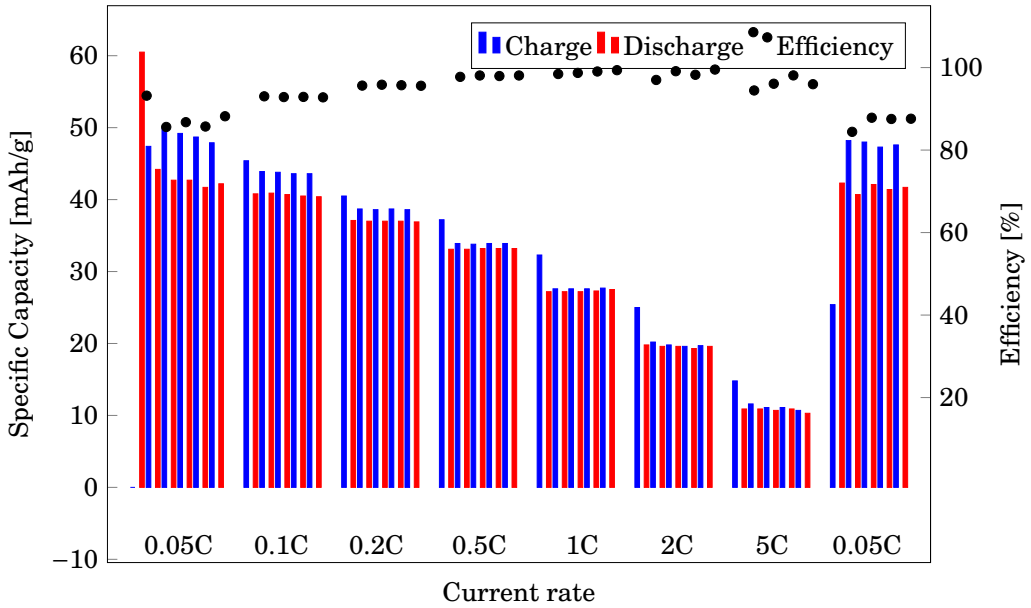

Figure C.1: Rate capability for cathode of milled Mn_3O_4. The cathode's active mass was 1.6 mg.

C.2 Milled Mn_3O_4 with RGO

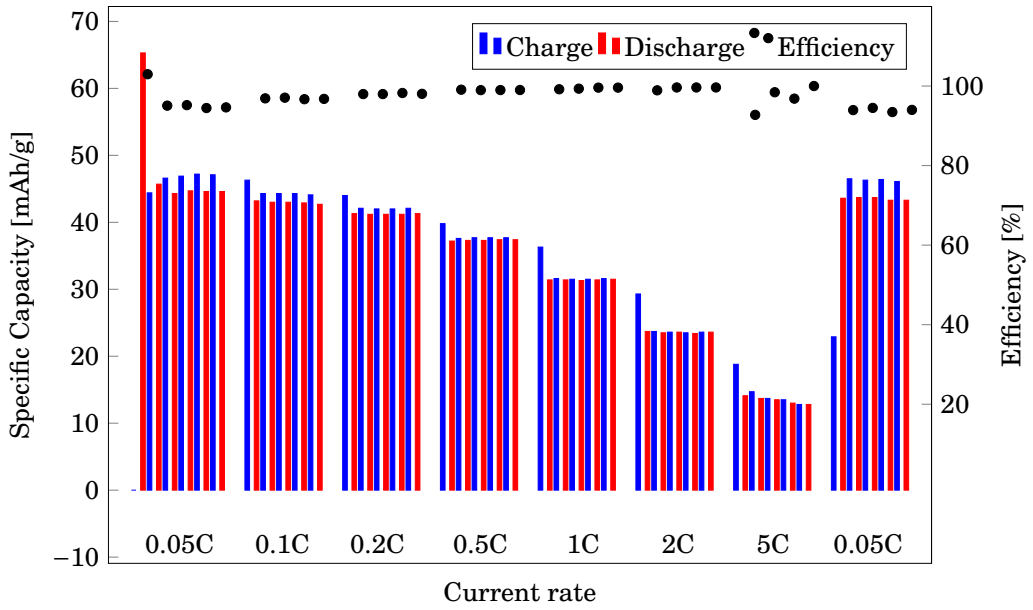

Figure C.2: Rate capability for cathode of milled Mn_3O_4 with RGO. The cathode's active mass was 1.7 mg.

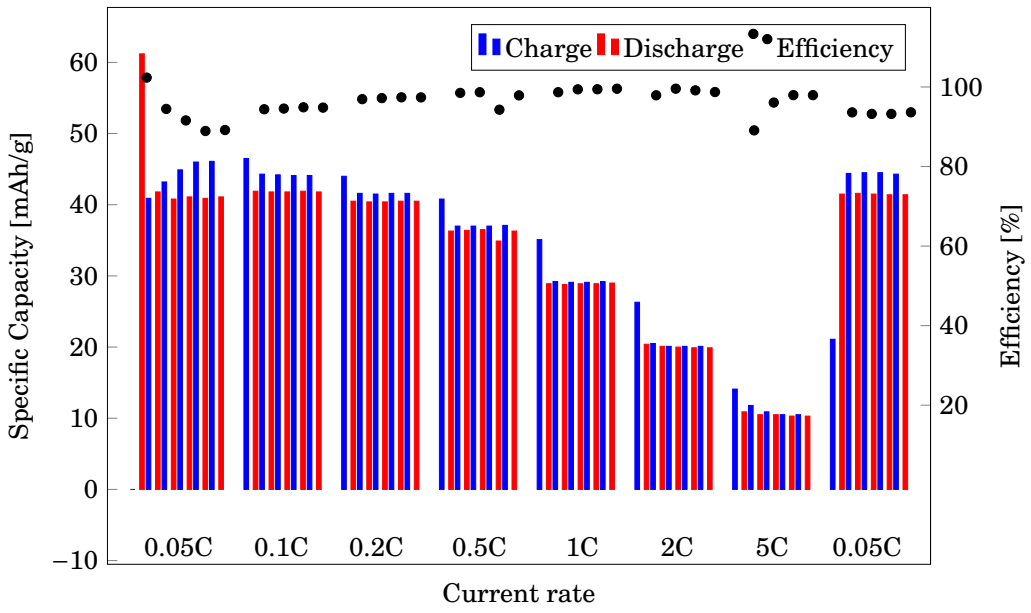

Figure C.3: Rate capability for cathode of milled Mn_3O_4 with RGO. The cathode's active mass was 1.77 mg.

C.3 Cycling at rate 0.02C

The two cathodes cycled at 0.02C achieving first charge capacity very close to the initial discharge are presented in Figure C.4 and C.5. The cathodes were cycled at 0.02C as part of the preparation for ex situ study.

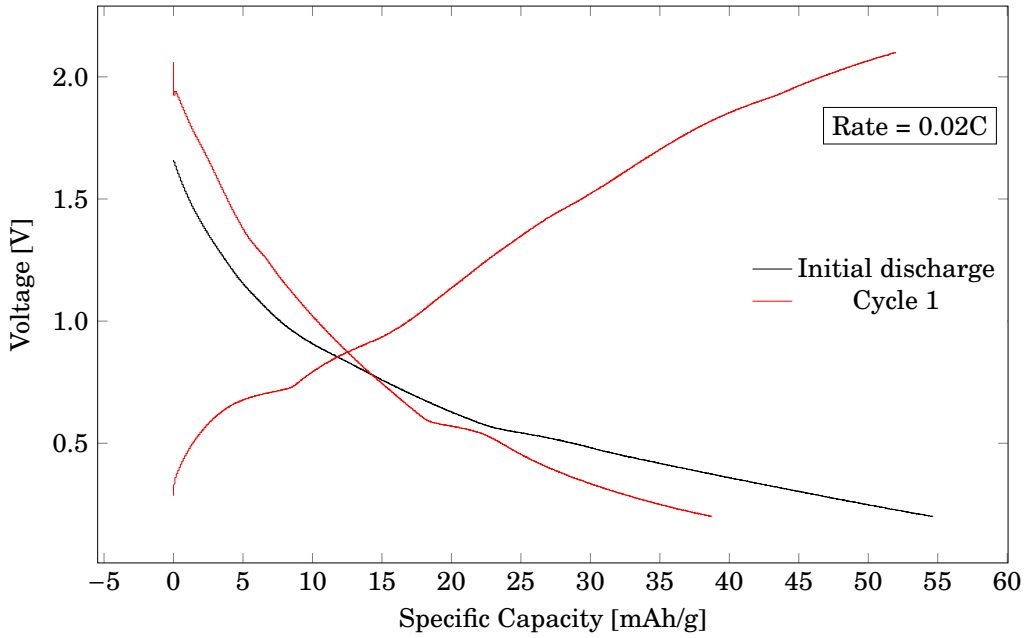

Figure C.4: Charge-discharge curves for cathode of pure, milled Mn_3O_4 cycled at 0.02C during preparation for ex situ study. The plot also show a quite high first charge capacity, only 5 % lower than the initial discharge. Active mass of the cathode was 1.2 mg.

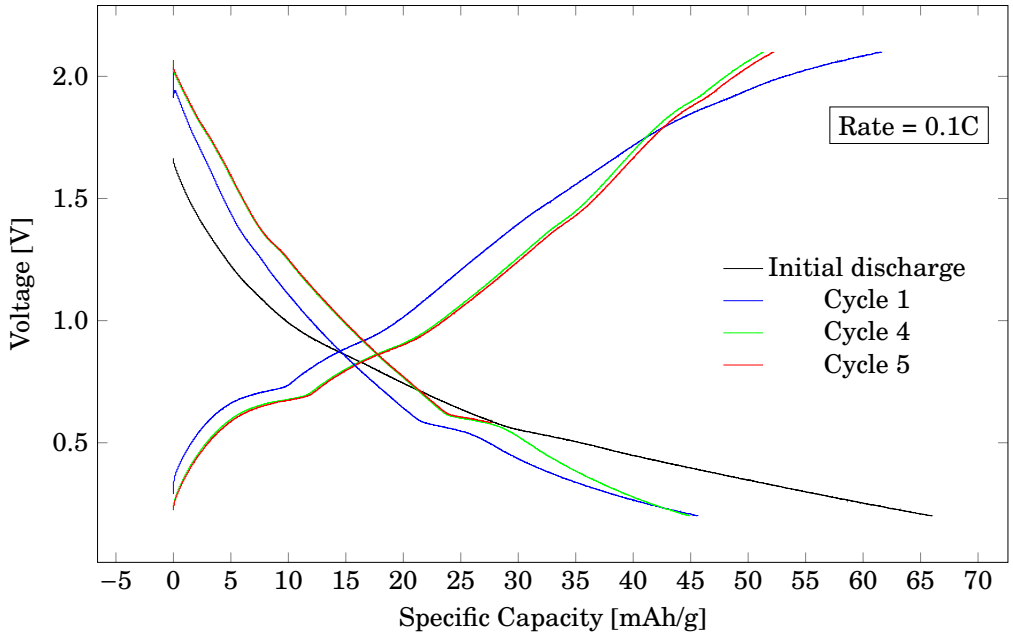

Figure C.5: Charge-discharge curves for cathode of pure, milled Mn_3O_4 cycled at 0.02C during preparation for ex situ study. The plot also show a quite high first charge capacity, only 7 % lower than the initial discharge. Active mass of the cathode was 1.44 mg.

Appendix D

EDS analysis

In this chapter, the EDS results summarized in the results section 4.3.2 are given in detail. These results include SEM images, EDS spectra and the accurate analysis data.

D.1 Cathode A

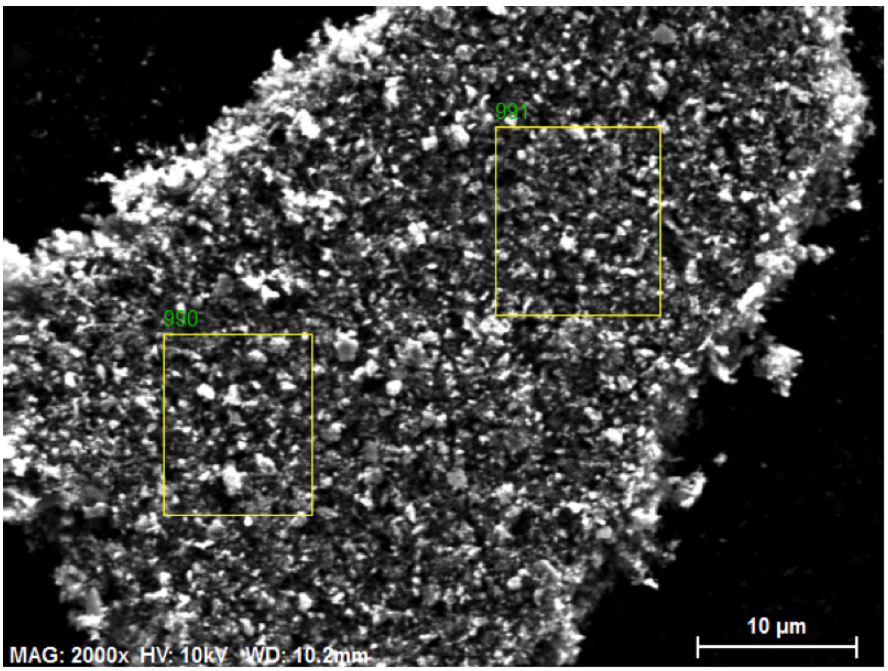

Figure D.1: SEM image showing the scanned areas of cathode A, i.e. the two yellow squares in the figure.

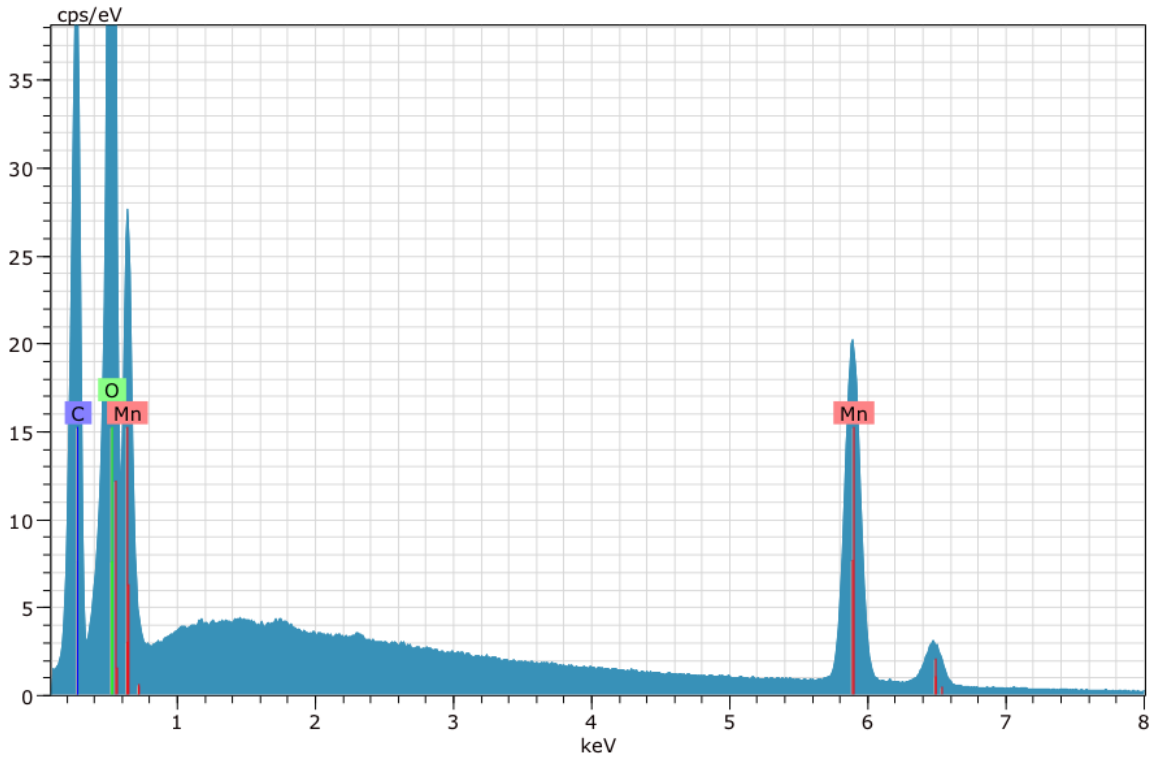

Figure D.2: EDS spectra of the left square in the SEM image above.

Spectrum: 990

El	AN	Series	Net	unn. C [wt.%]	norm. C [wt.%]	Atom. C [at.%]	Error (1 Sigma) [wt.%]
Mn	25	K-series	176544	67.12	67.29	34.30	2.69
O	8	K-series	260267	18.11	18.16	31.78	1.98
C	6	K-series	126817	14.51	14.55	33.92	1.64
		Total:		99.75	100.00	100.00	

Figure D.3: Accurate amount values obtained from the scanned area.

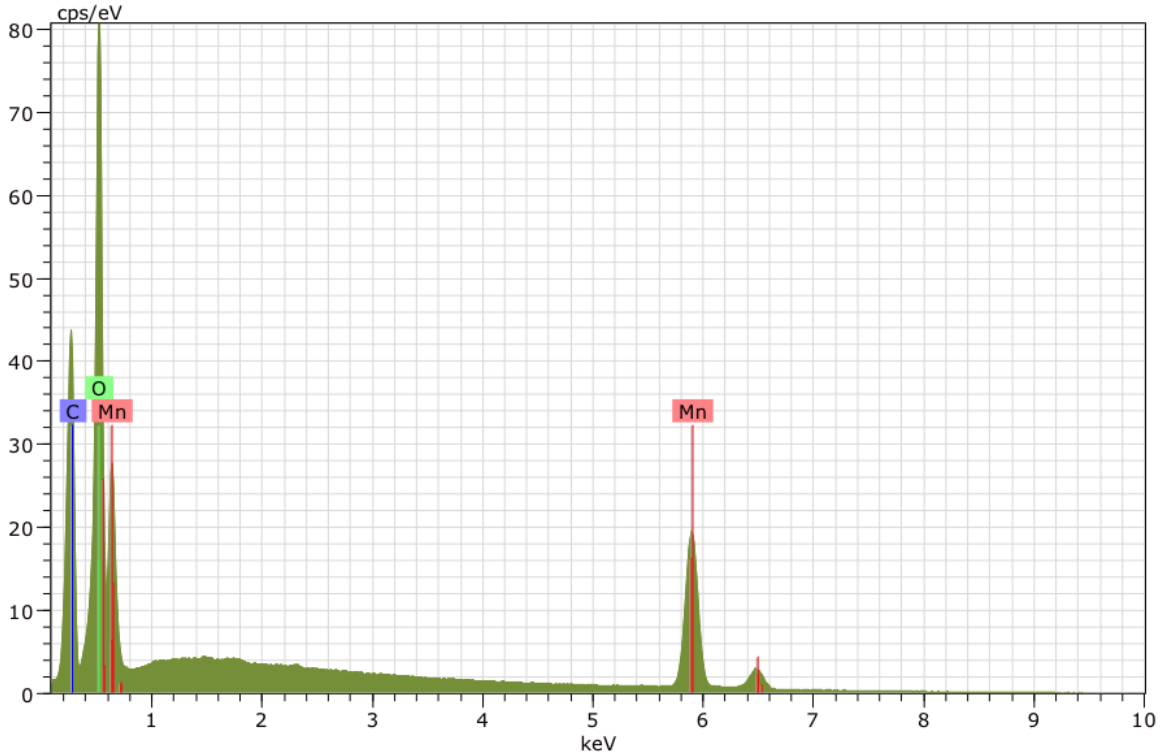

Figure D.4: EDS spectra of the right square in the SEM image above.

Spectrum: 991

El	AN	Series	Net	unn. C [wt.%]	norm. C [wt.%]	Atom. C [at.%]	Error (1 Sigma) [wt.%]
Mn	25	K-series	170562	59.79	66.57	33.47	2.40
O	8	K-series	250073	16.23	18.07	31.20	1.78
C	6	K-series	131378	13.80	15.36	35.33	1.56
		Total:		89.82	100.00	100.00	

Figure D.5: Accurate amount values obtained from the scanned area.

D.2 Cathode B

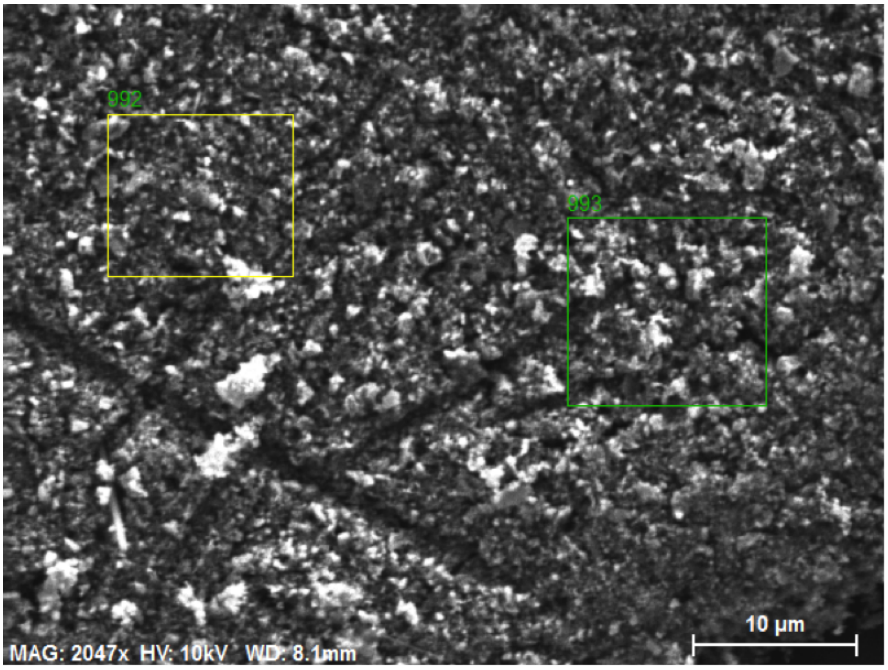

Figure D.6: SEM image showing the two first scanned areas of cathode B, i.e. the two yellow and green squares in the figure.

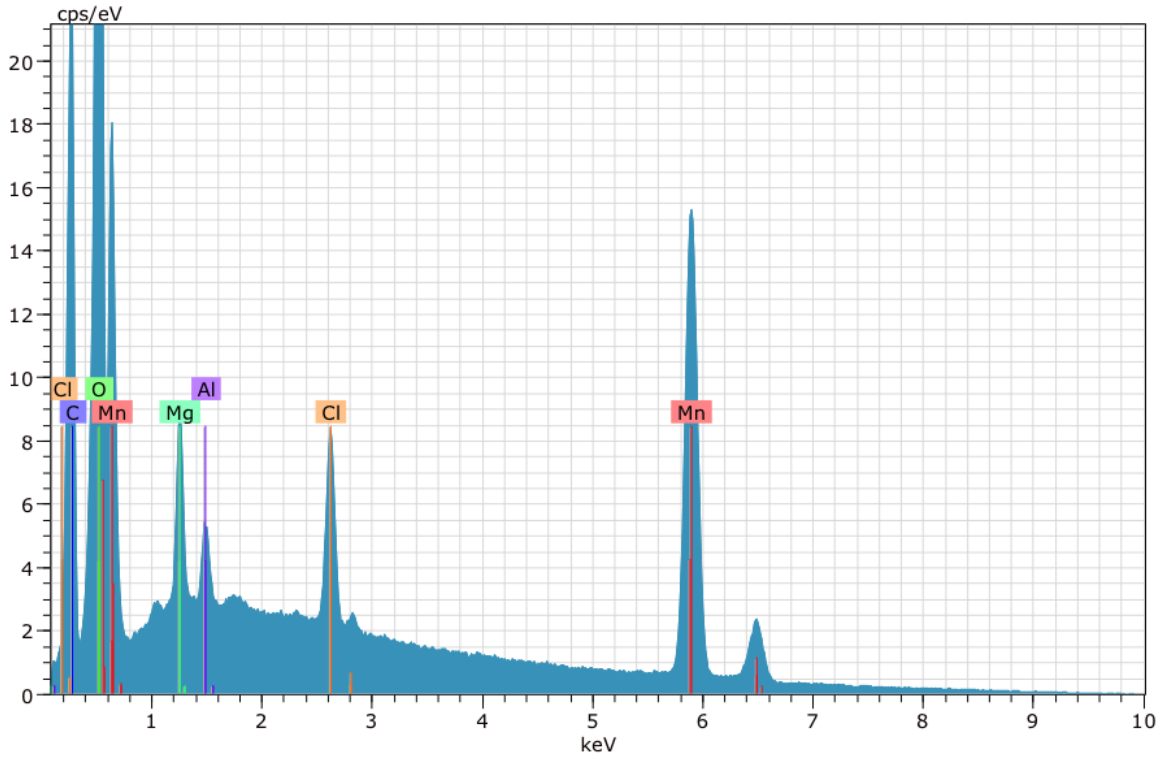

Figure D.7: EDS spectra of the left square in the SEM image above.

Spectrum: 992

El	AN	Series	Net	unn. C [wt.%]	norm. C [wt.%]	Atom. C [at.%]	Error (1 Sigma) [wt.%]
Mn	25	K-series	134369	67.36	67.38	36.01	2.71
O	8	K-series	186734	17.11	17.12	31.41	1.89
C	6	K-series	67722	11.86	11.87	29.01	1.39
Cl	17	K-series	36051	2.00	2.00	1.66	0.09
Mg	12	K-series	23931	1.22	1.22	1.48	0.09
Al	13	K-series	9022	0.41	0.41	0.45	0.04
		Total:		99.96	100.00	100.00	

Figure D.8: Accurate amount values obtained from the scanned area.

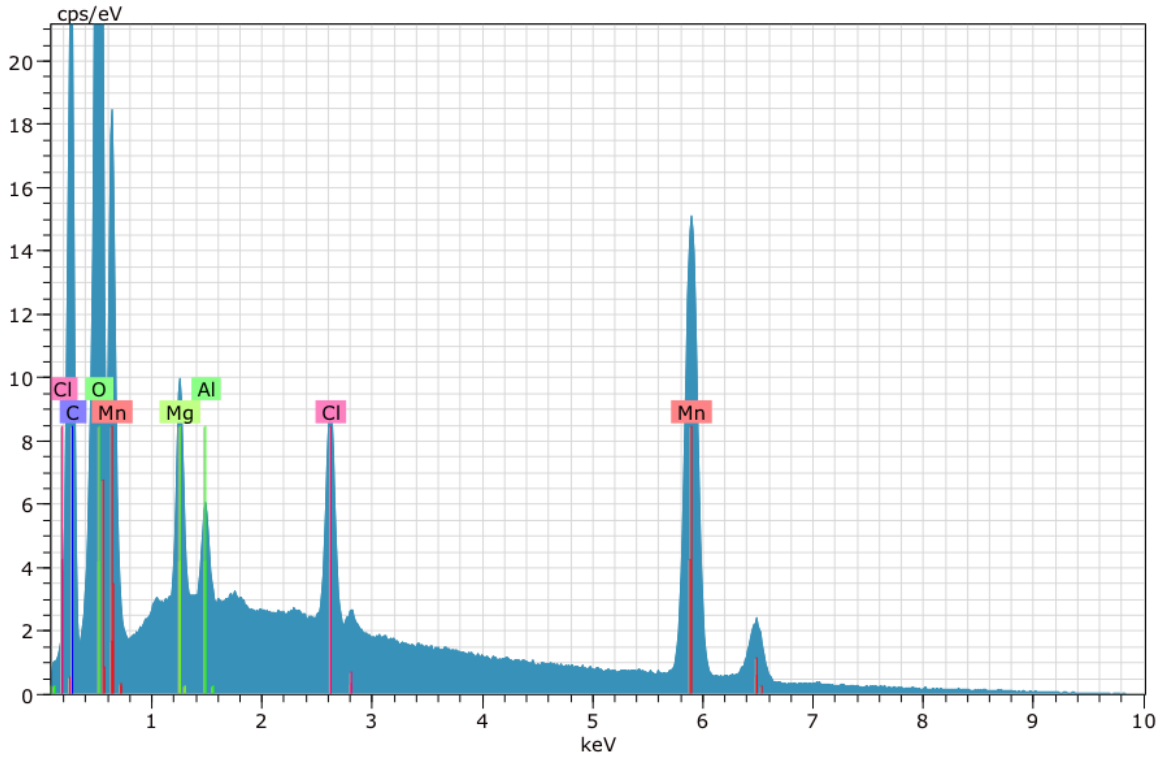

Figure D.9: EDS spectra of the right square in the SEM image above.

Spectrum: 993

El	AN	Series	Net	unn. C [wt.%]	norm. C [wt.%]	Atom. C [at.%]	Error (1 Sigma) [wt.%]
Mn	25	K-series	132768	65.60	66.20	34.97	2.64
O	8	K-series	191629	17.37	17.53	31.80	1.92
C	6	K-series	68273	11.94	12.05	29.12	1.40
Cl	17	K-series	41458	2.26	2.28	1.87	0.10
Mg	12	K-series	28325	1.41	1.43	1.70	0.10
Al	13	K-series	11285	0.50	0.51	0.55	0.05
		Total:		99.09	100.00	100.00	

Figure D.10: Accurate amount values obtained from the scanned area.

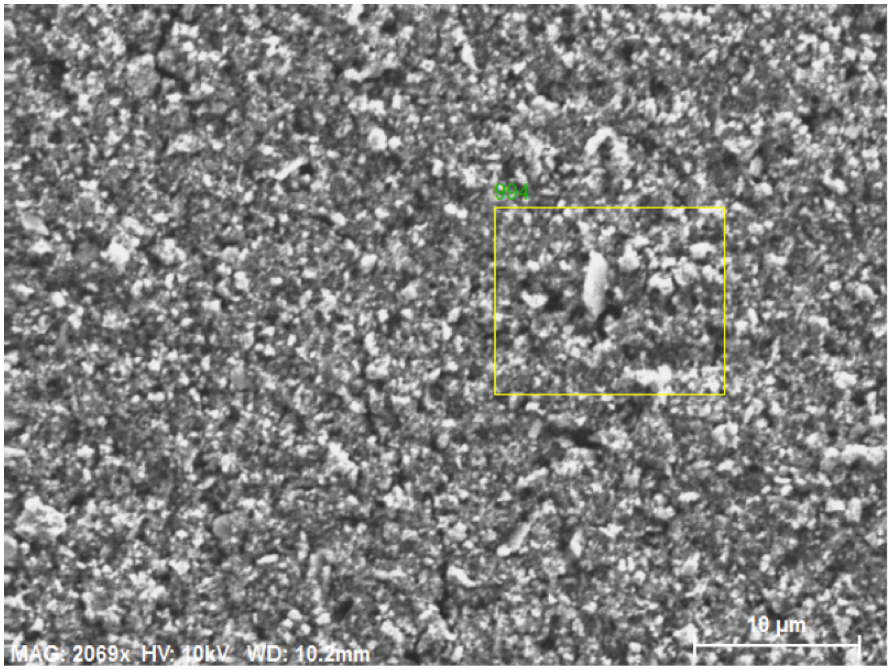

Figure D.11: SEM image showing the third scanned area of cathode B, i.e. the yellow square in the figure.

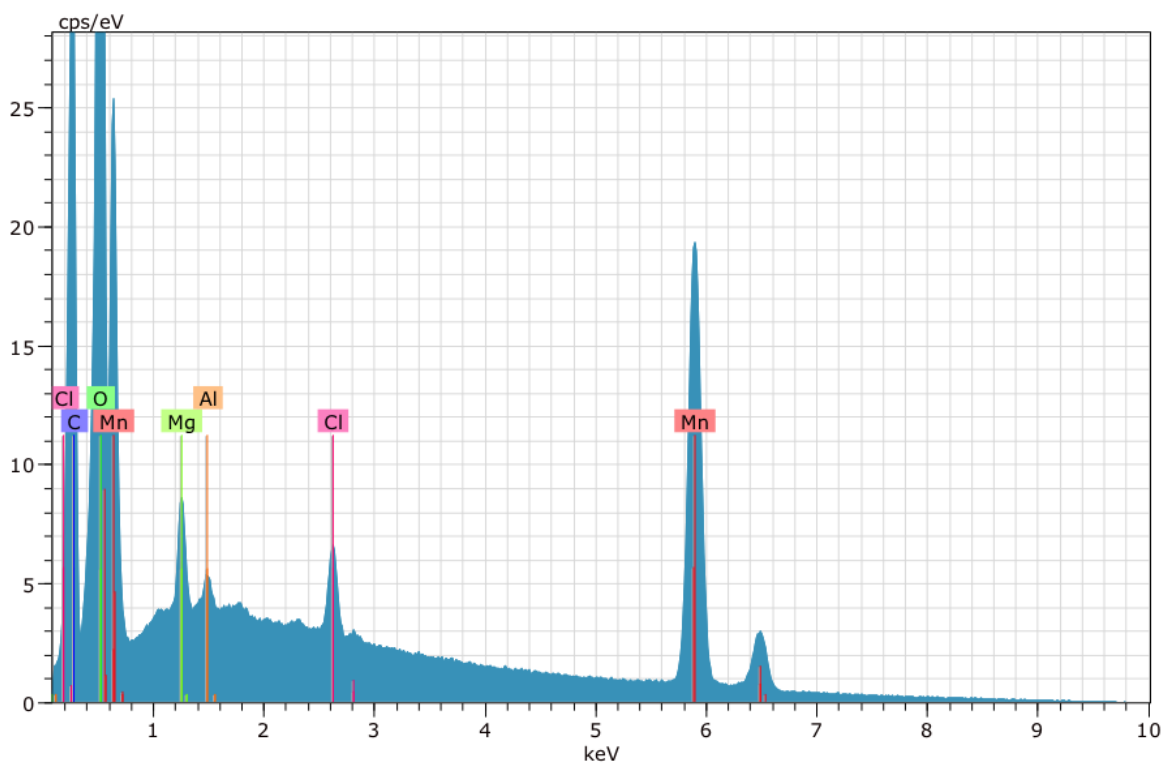

Figure D.12: EDS spectra of the square in the SEM image above.

Spectrum: 994

El	AN	Series	Net	unn. C [wt.%]	norm. C [wt.%]	Atom. C [at.%]	Error (1 Sigma) [wt.%]
Mn	25	K-series	171344	65.57	67.49	35.40	2.63
O	8	K-series	251935	17.48	17.99	32.40	1.91
C	6	K-series	98733	12.29	12.65	30.36	1.41
Cl	17	K-series	21730	0.92	0.94	0.77	0.06
Mg	12	K-series	19412	0.76	0.78	0.92	0.06
Al	13	K-series	4240	0.15	0.15	0.16	0.03
		Total:		97.16	100.00	100.00	

Figure D.13: Accurate amount values obtained from the scanned area.

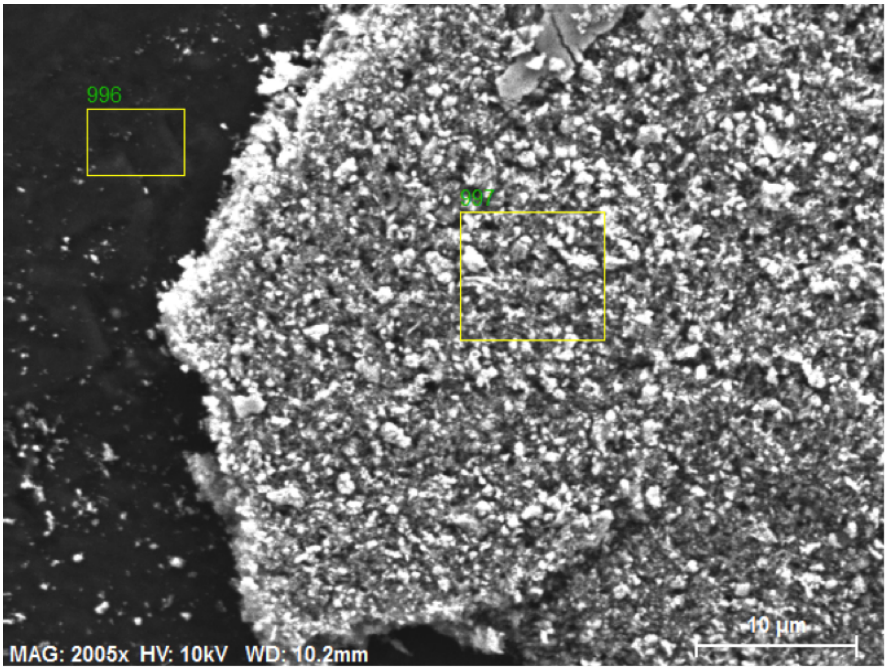

Figure D.14: SEM image showing the fourth scanned area of cathode B, i.e. the yellow square on the particle surface in the figure.

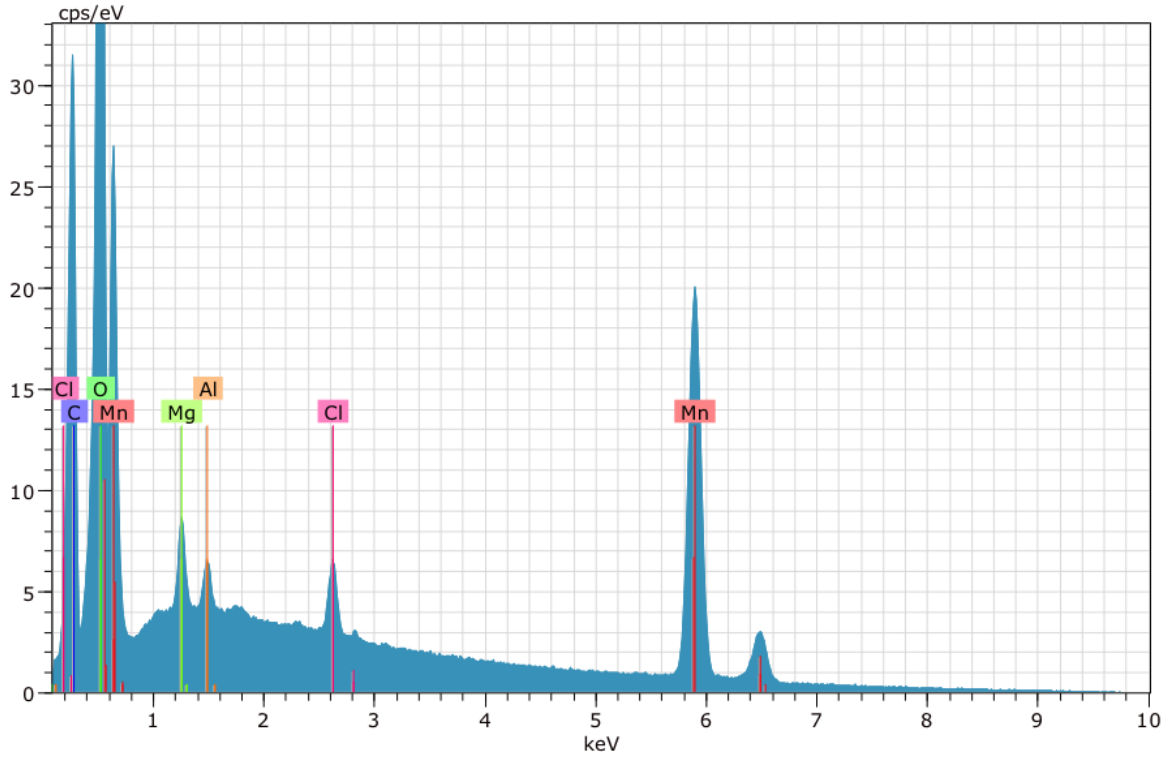

Figure D.15: EDS spectra of the right hand square in the SEM image above.

Spectrum: 997

El	AN	Series	Net	unn. C [wt.%]	norm. C [wt.%]	Atom. C [at.%]	Error (1 Sigma) [wt.%]
Mn	25	K-series	174827	65.87	67.50	35.55	2.64
O	8	K-series	266784	18.05	18.50	33.46	1.97
C	6	K-series	95777	11.76	12.05	29.04	1.35
Cl	17	K-series	20535	0.85	0.88	0.71	0.06
Mg	12	K-series	18958	0.73	0.75	0.89	0.06
Al	13	K-series	9398	0.32	0.33	0.35	0.04
		Total:		97.59	100.00	100.00	

Figure D.16: Accurate amount values obtained from the scanned area.

D.3 Cathode C

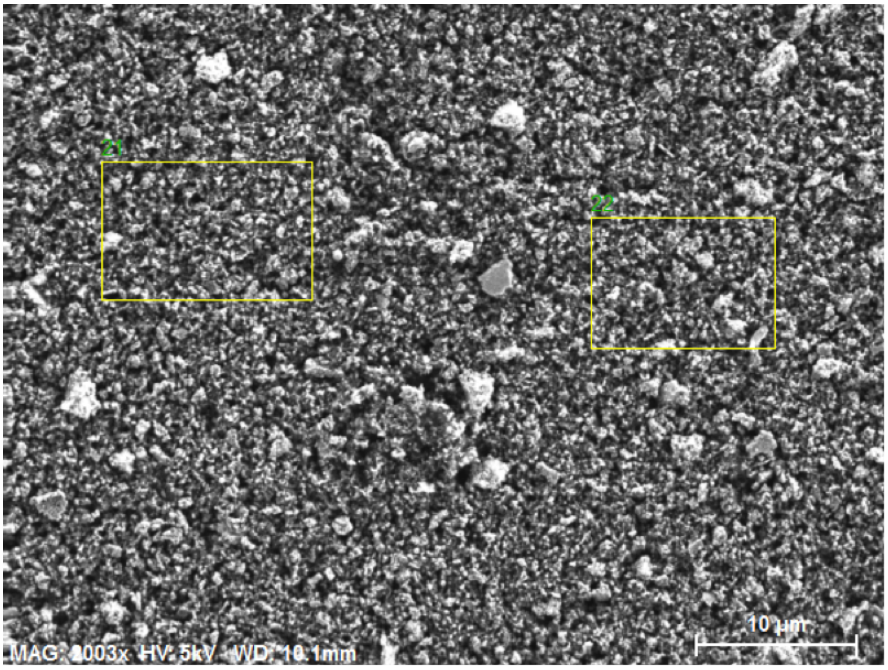

Figure D.17: SEM image showing the two first scanned areas of cathode C, i.e. the two yellow squares in the figure.

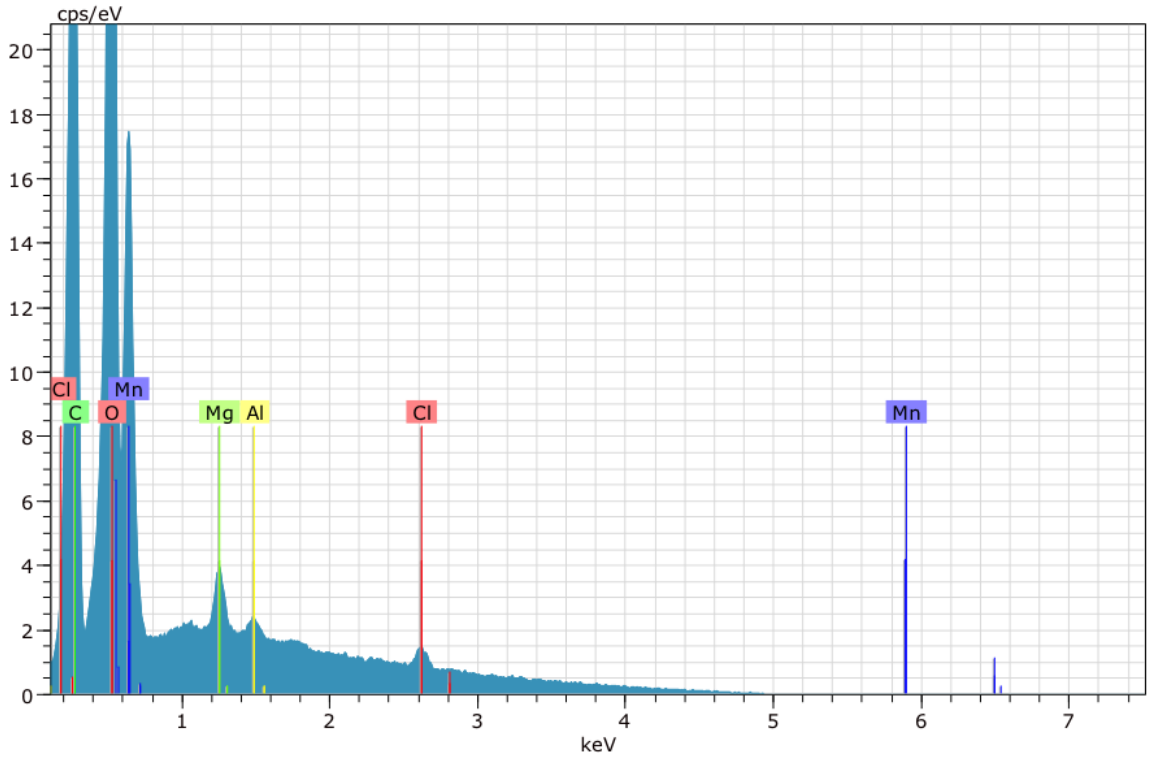

Figure D.18: EDS spectra of the left square in the SEM image above.

Spectrum: 21

El	AN	Series	Net	unn. C [wt.%]	norm. C [wt.%]	Atom. C [at.%]	Error (1 Sigma) [wt.%]
Mn	25	L-series	84459	47.91	47.91	19.80	5.48
O	8	K-series	134080	28.30	28.30	40.15	3.16
C	6	K-series	87295	19.49	19.49	36.82	2.24
Cl	17	K-series	4020	2.57	2.57	1.64	0.17
Mg	12	K-series	7159	1.37	1.37	1.27	0.10
Al	13	K-series	1732	0.37	0.37	0.31	0.05
		Total:		100.00	100.00	100.00	

Figure D.19: Accurate amount values obtained from the scanned area.

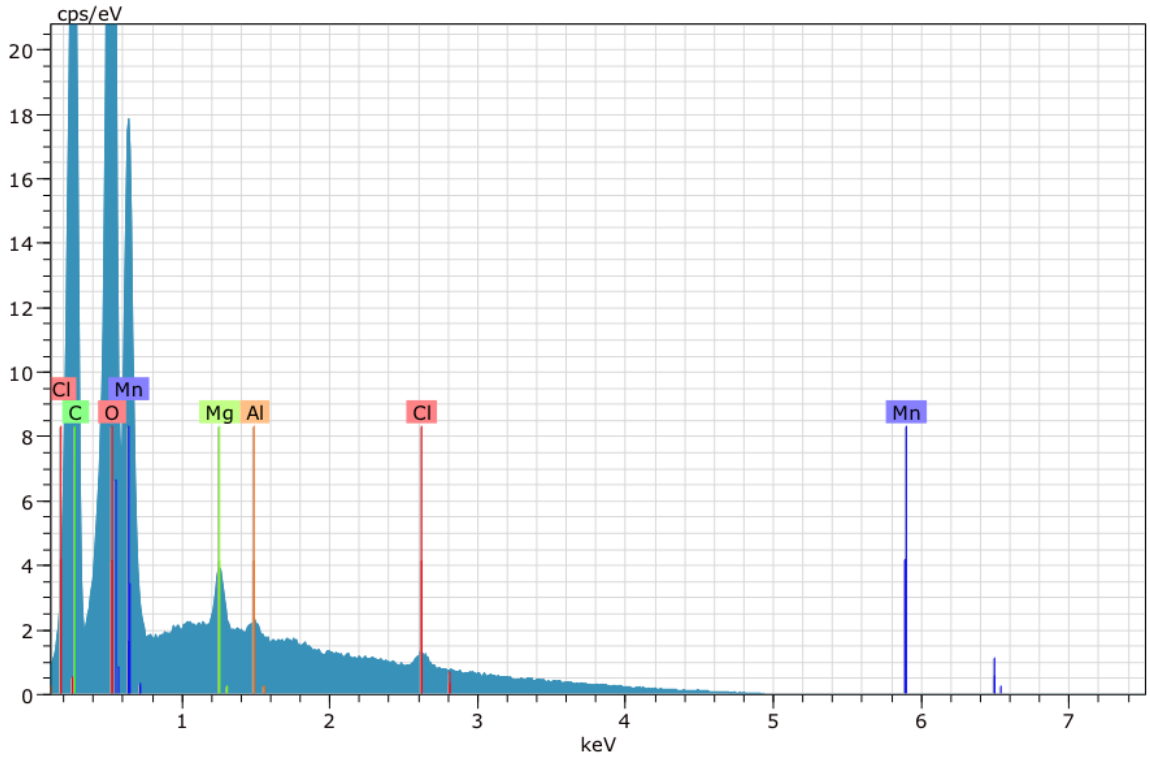

Figure D.20: EDS spectra of the right square in the SEM image above.

Spectrum: 22

El	AN	Series	Net	unn. C [wt.%]	norm. C [wt.%]	Atom. C [at.%]	Error (1 Sigma) [wt.%]
Mn	25	L-series	86989	49.14	49.14	20.56	5.61
O	8	K-series	138444	28.85	28.85	41.46	3.22
C	6	K-series	83398	18.37	18.37	35.17	2.12
Cl	17	K-series	3201	2.02	2.02	1.31	0.14
Mg	12	K-series	7088	1.35	1.35	1.27	0.10
Al	13	K-series	1272	0.27	0.27	0.23	0.04
		Total:		100.00	100.00	100.00	

Figure D.21: Accurate amount values obtained from the scanned area.

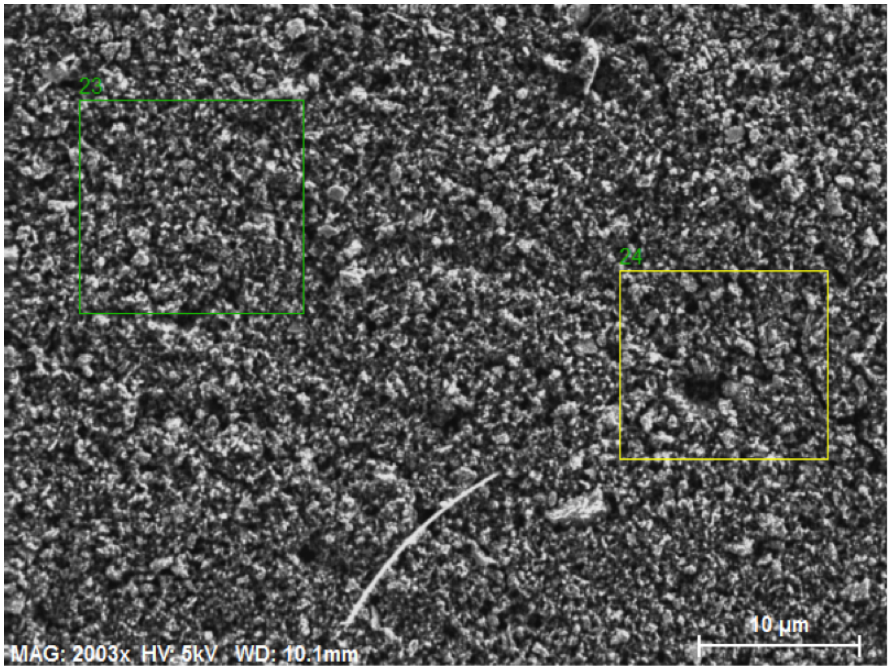

Figure D.22: SEM image showing the third scanned area of cathode C, i.e. the yellow square in the figure.

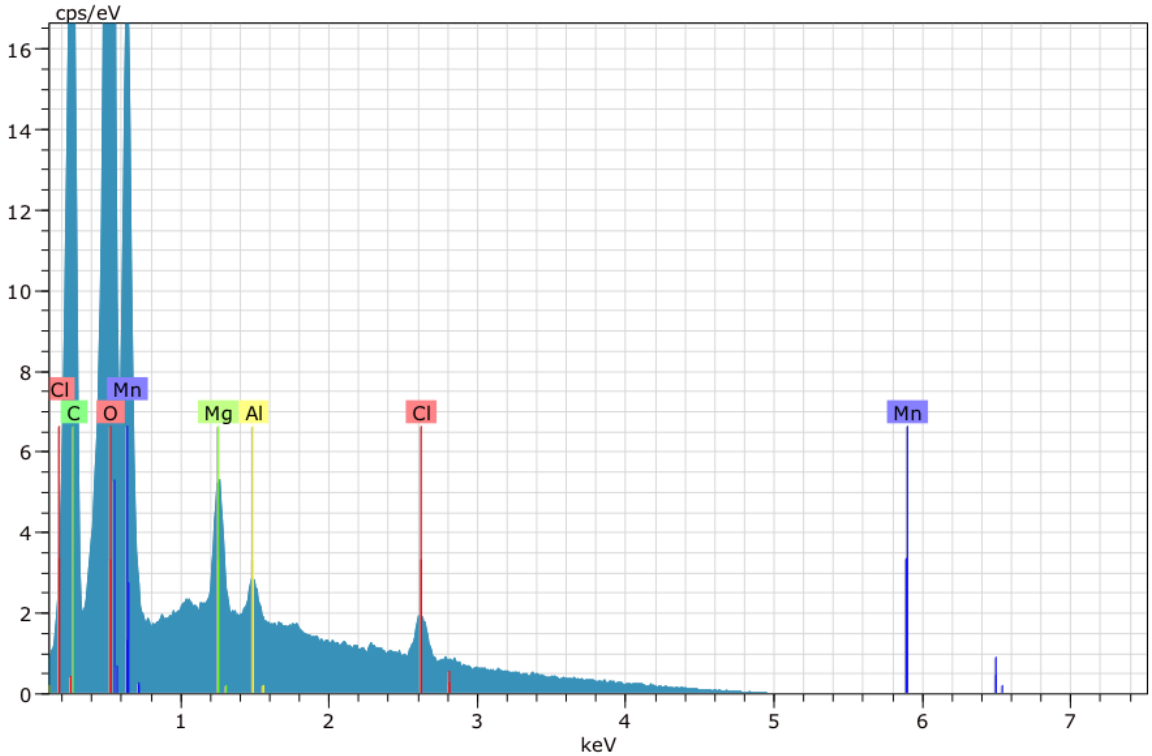

Figure D.23: EDS spectra of the yellow square in the SEM image above.

Spectrum: 24

El	AN	Series	Net	unn. C [wt.%]	norm. C [wt.%]	Atom. C [at.%]	Error (1 Sigma) [wt.%]
Mn	25	L-series	82024	47.58	47.58	20.42	5.45
O	8	K-series	142757	30.23	30.23	44.55	3.37
C	6	K-series	62176	14.97	14.97	29.39	1.76
Cl	17	K-series	6586	4.26	4.26	2.83	0.26
Mg	12	K-series	12107	2.35	2.35	2.28	0.15
Al	13	K-series	2800	0.61	0.61	0.53	0.06
		Total:		100.00	100.00	100.00	

Figure D.24: Accurate amount values obtained from the scanned area.

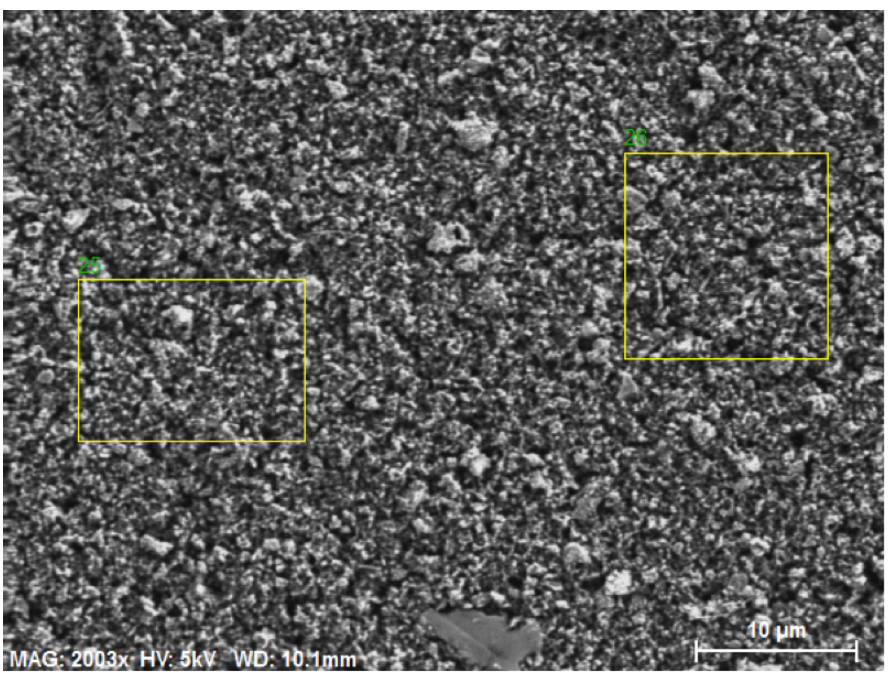

Figure D.25: SEM image showing the fourth and fifth scanned areas of cathode C, i.e. the two yellow squares in the figure.

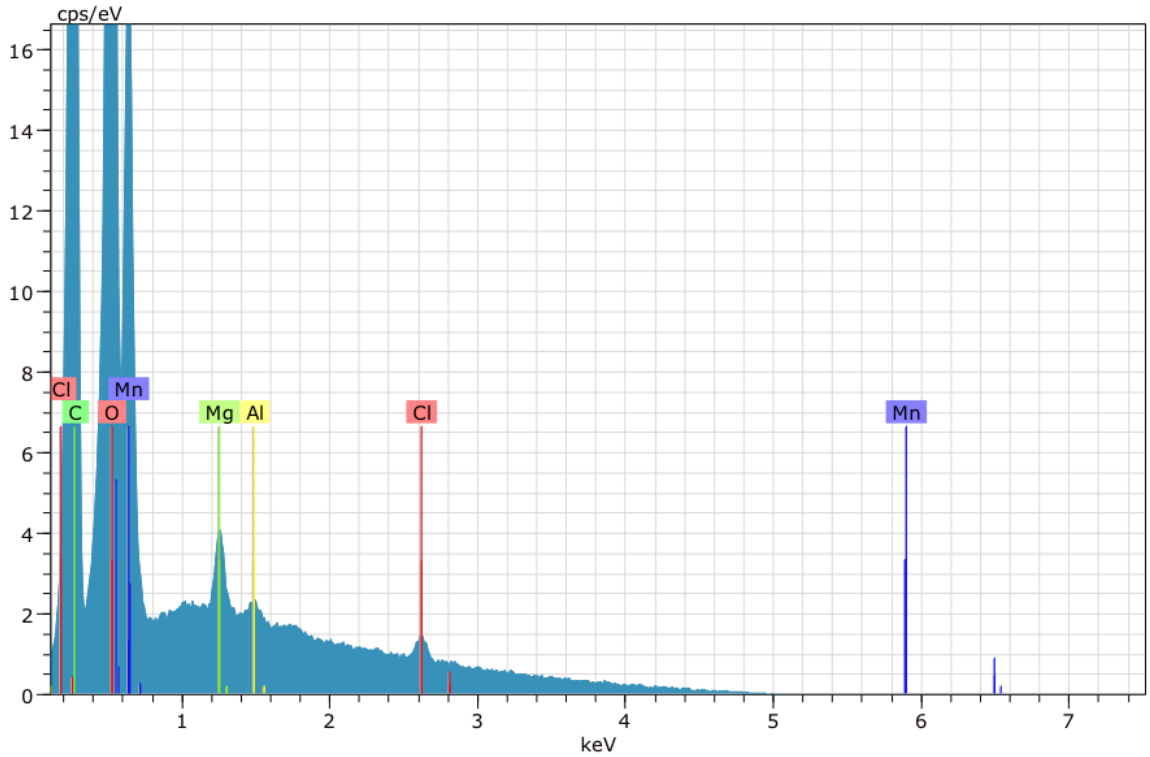

Figure D.26: EDS spectra of the left square in the SEM image above.

Spectrum: 25

El	AN	Series	Net	unn. C [wt.%]	norm. C [wt.%]	Atom. C [at.%]	Error (1 Sigma) [wt.%]
Mn	25	L-series	88883	48.40	48.40	20.10	5.51
O	8	K-series	141257	28.52	28.52	40.68	3.18
C	6	K-series	89097	19.03	19.03	36.15	2.18
Cl	17	K-series	3877	2.37	2.37	1.52	0.16
Mg	12	K-series	7634	1.40	1.40	1.31	0.10
Al	13	K-series	1357	0.28	0.28	0.23	0.04
		Total:		100.00	100.00	100.00	

Figure D.27: Accurate amount values obtained from the scanned area.

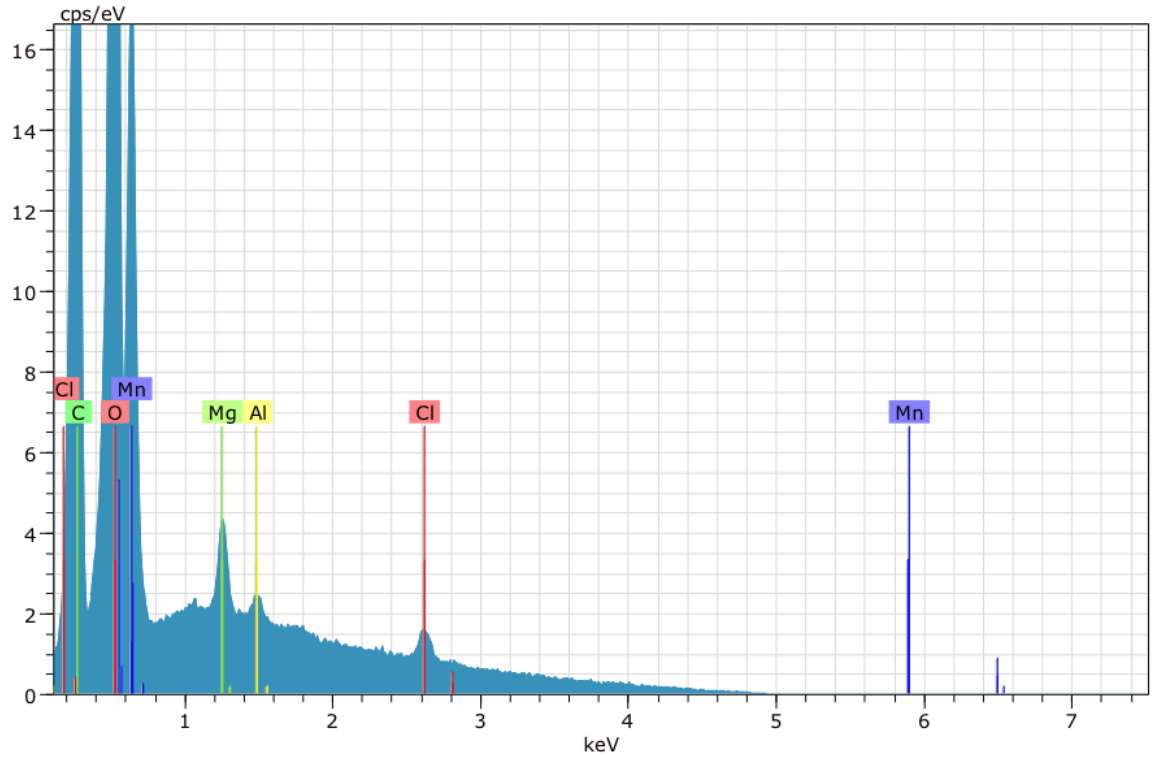

Figure D.28: EDS spectra of the right square in the SEM image above.

Spectrum: 26

El	AN	Series	Net	unn. C [Wt.%]	norm. C [Wt.%]	Atom. C [at.%]	Error (1 Sigma) [Wt.%]
Mn	25	L-series	84815	47.90	47.90	20.11	5.47
O	8	K-series	140656	29.27	29.27	42.19	3.26
C	6	K-series	77420	17.54	17.54	33.67	2.03
Cl	17	K-series	5046	3.19	3.19	2.08	0.20
Mg	12	K-series	8829	1.67	1.67	1.59	0.11
Al	13	K-series	2023	0.43	0.43	0.37	0.05
		Total:		100.00	100.00	100.00	

Figure D.29: Accurate amount values obtained from the scanned area.

D.4 Cathode D

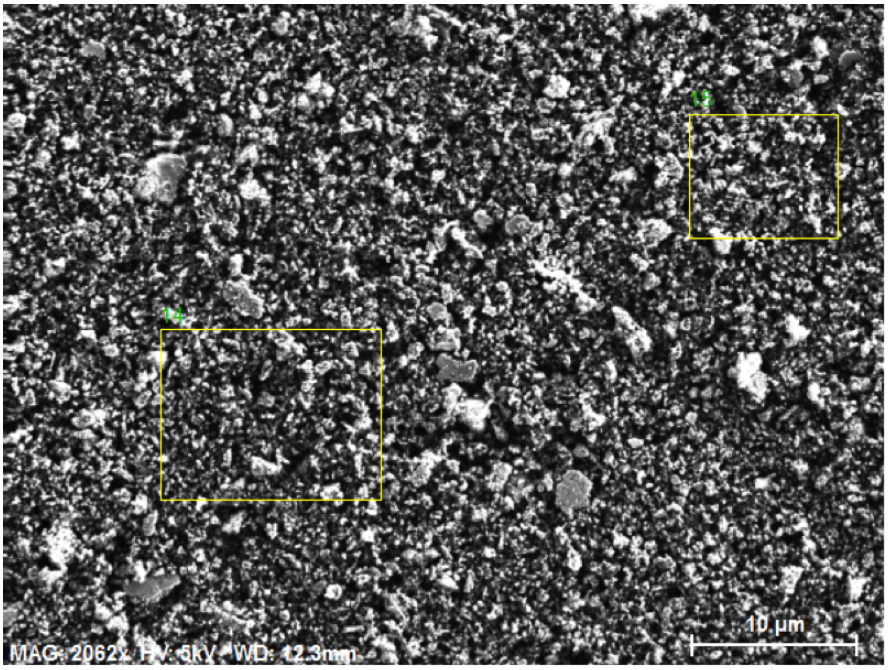

Figure D.30: SEM image showing the two first scanned areas of cathode D, i.e. the two yellow squares in the figure.

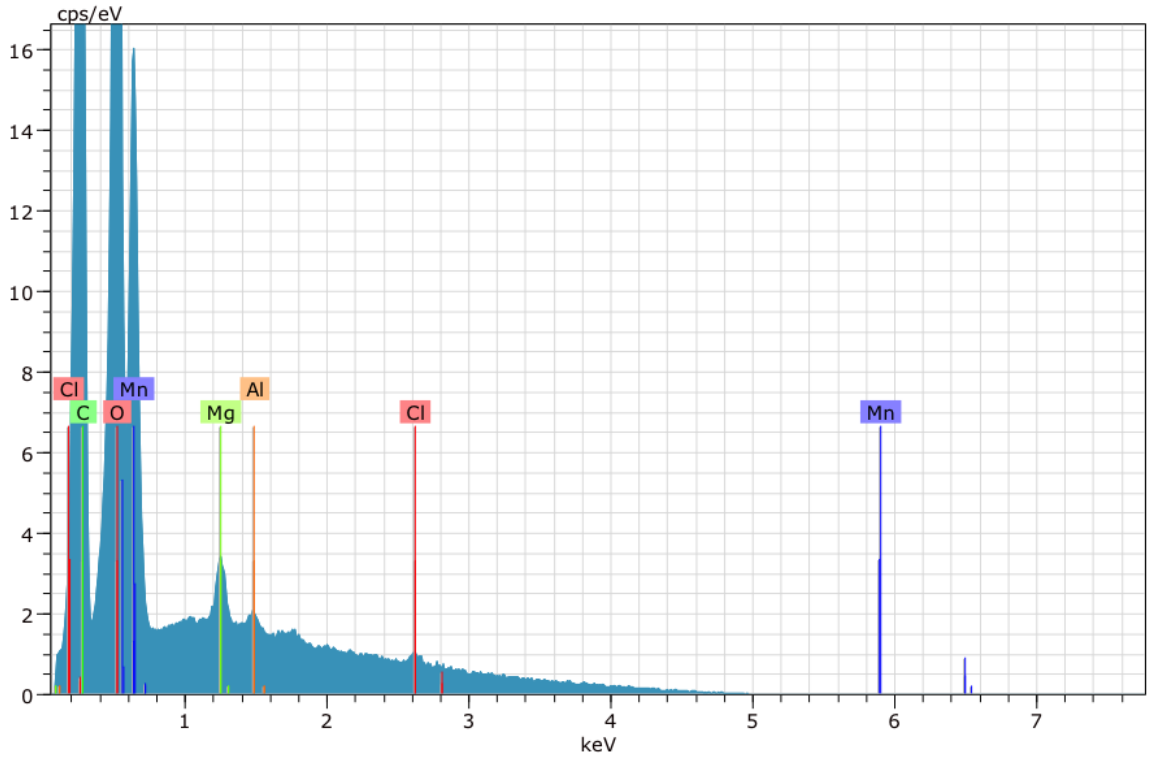

Figure D.31: EDS spectra of the left square in the SEM image above.

Spectrum: 14

El	AN	Series	Net	unn. C [wt.%]	norm. C [wt.%]	Atom. C [at.%]	Error (1 Sigma) [wt.%]
Mn	25	L-series	77622	48.43	48.43	19.76	5.56
O	8	K-series	117636	27.48	27.48	38.49	3.09
C	6	K-series	88724	21.16	21.16	39.48	2.43
Cl	17	K-series	1990	1.39	1.39	0.88	0.11
Mg	12	K-series	6096	1.27	1.27	1.17	0.09
Al	13	K-series	1132	0.26	0.26	0.22	0.04
		Total:		100.00	100.00	100.00	

Figure D.32: Accurate amount values obtained from the scanned area.

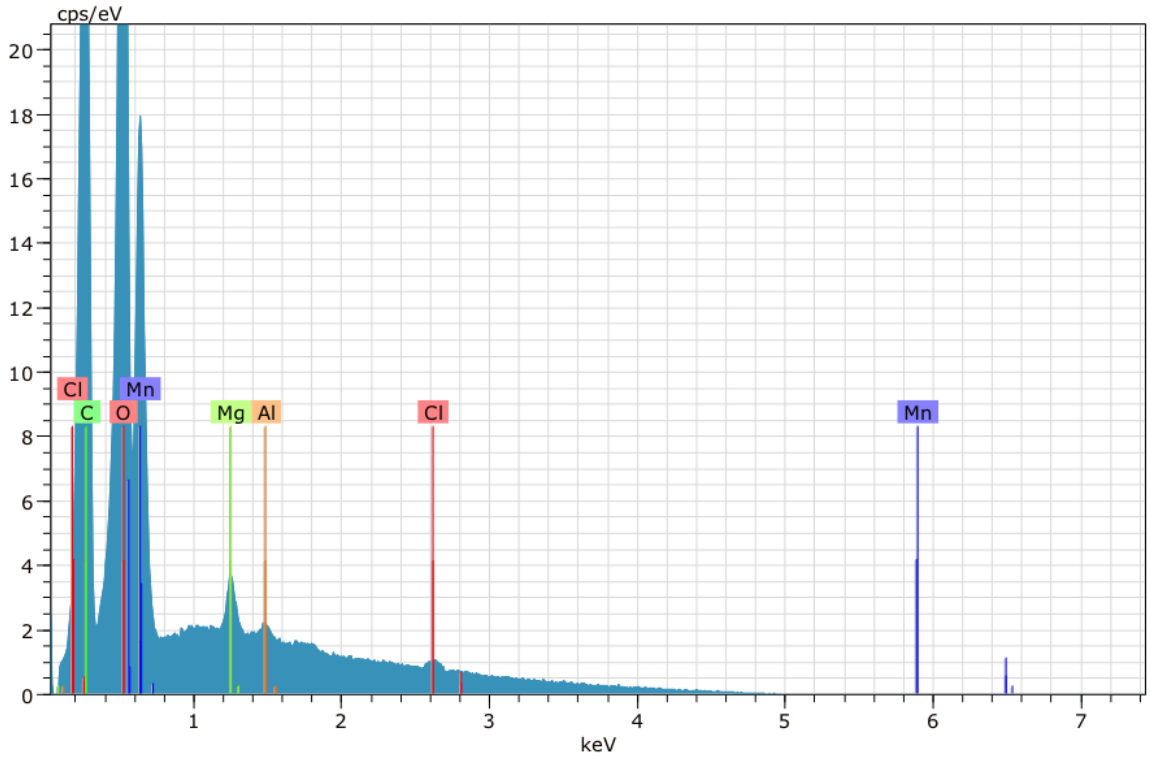

Figure D.33: EDS spectra of the right square in the SEM image above.

Spectrum: 15

El	AN	Series	Net	unn. C [wt.%]	norm. C [wt.%]	Atom. C [at.%]	Error (1 Sigma) [wt.%]
Mn	25	L-series	87279	49.54	49.54	20.55	5.65
O	8	K-series	131931	27.85	27.85	39.68	3.12
C	6	K-series	90793	19.78	19.78	37.53	2.27
Cl	17	K-series	2026	1.29	1.29	0.83	0.10
Mg	12	K-series	6529	1.24	1.24	1.17	0.09
Al	13	K-series	1422	0.30	0.30	0.26	0.04
		Total:		100.00	100.00	100.00	

Figure D.34: Accurate amount values obtained from the scanned area.

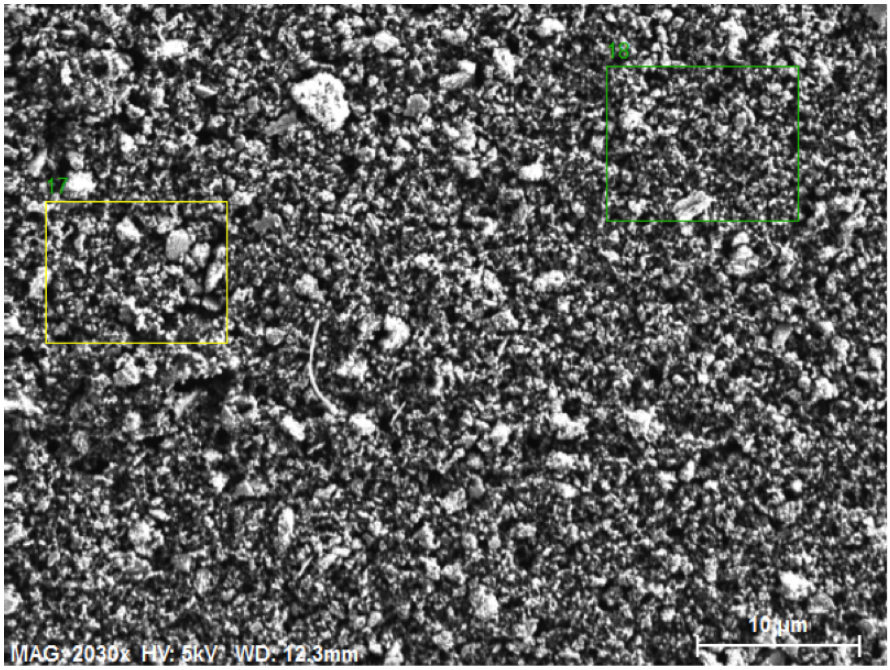

Figure D.35: SEM image showing the third and fourth scanned areas of cathode D, i.e. the yellow and green squares in the figure.

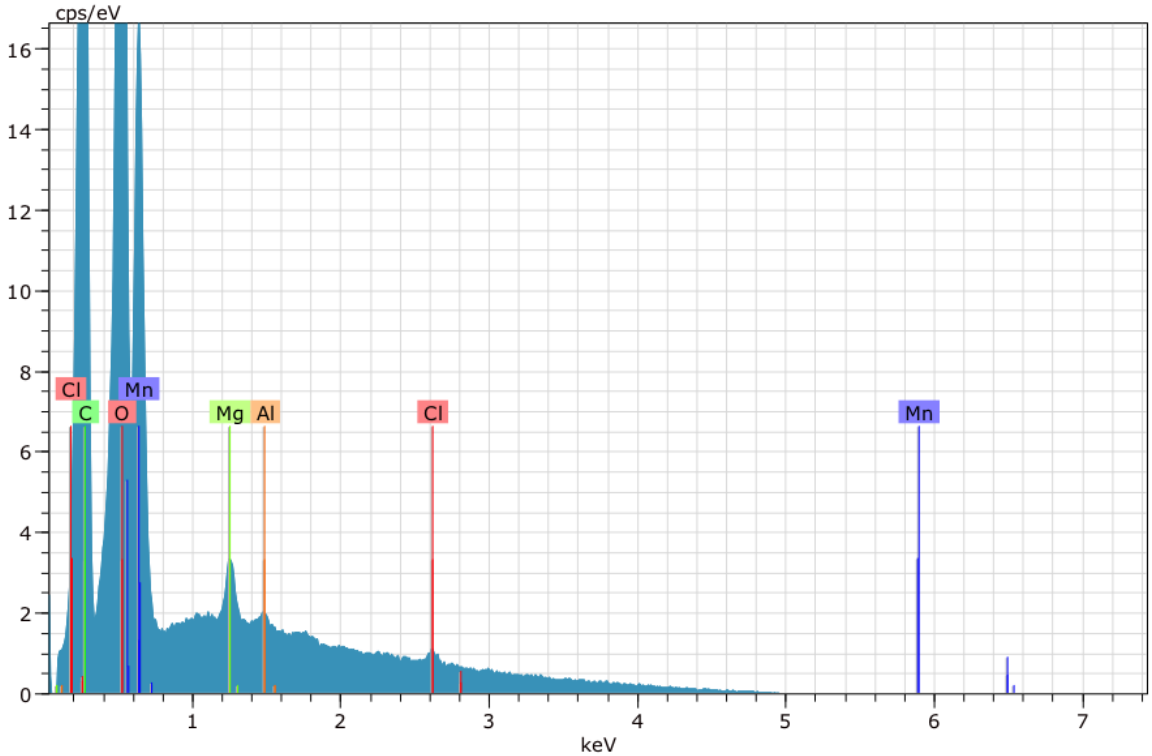

Figure D.36: EDS spectra of the yellow square in the SEM image above.

Spectrum: 17

El	AN	Series	Net	unn. C [wt.%]	norm. C [wt.%]	Atom. C [at.%]	Error (1 Sigma) [wt.%]
Mn	25	L-series	81662	49.73	49.73	20.69	5.69
O	8	K-series	122618	27.79	27.79	39.70	3.12
C	6	K-series	83783	19.65	19.65	37.40	2.26
Cl	17	K-series	2126	1.45	1.45	0.94	0.11
Mg	12	K-series	5645	1.16	1.16	1.09	0.09
Al	13	K-series	962	0.22	0.22	0.19	0.04
		Total:		100.00	100.00	100.00	

Figure D.37: Accurate amount values obtained from the scanned area.

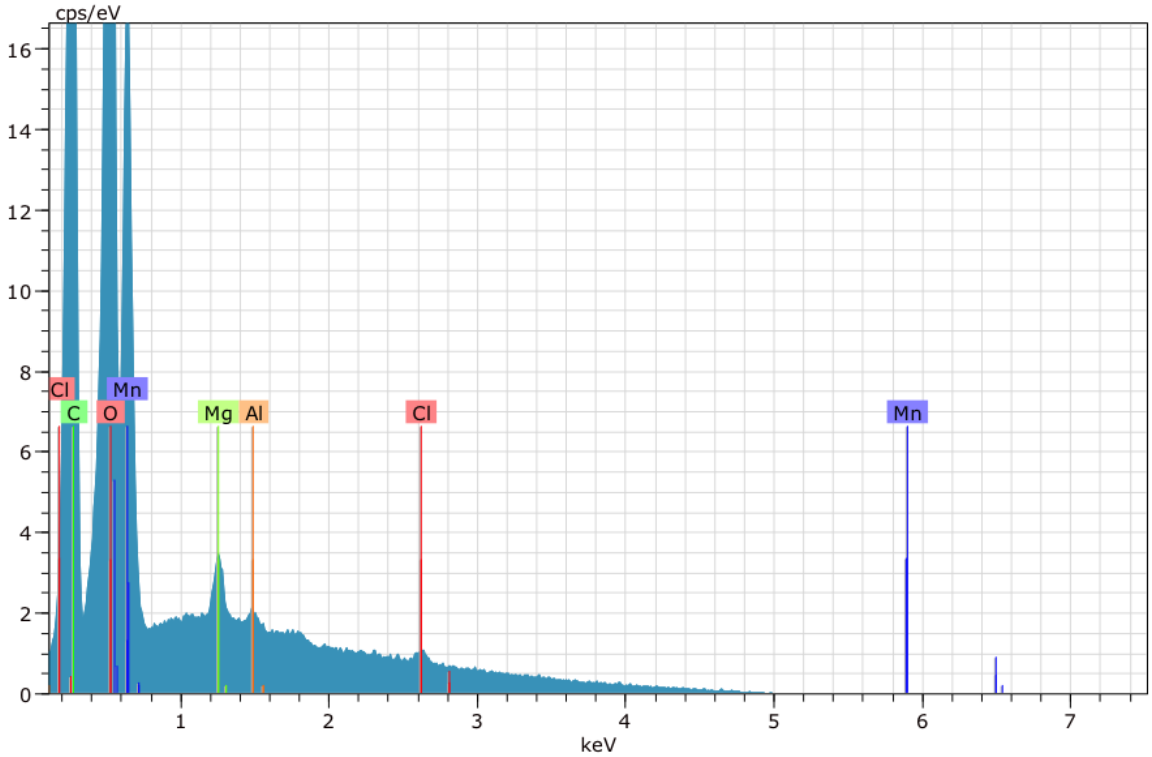

Figure D.38: EDS spectra of the green square in the SEM image above.

Spectrum: 18

El	AN	Series	Net	unn. C [wt.%]	norm. C [wt.%]	Atom. C [at.%]	Error (1 Sigma) [wt.%]
Mn	25	L-series	83284	50.41	50.41	21.23	5.76
O	8	K-series	125162	28.07	28.07	40.59	3.15
C	6	K-series	79415	18.61	18.61	35.86	2.15
Cl	17	K-series	2151	1.46	1.46	0.95	0.11
Mg	12	K-series	5987	1.22	1.22	1.16	0.09
Al	13	K-series	1023	0.23	0.23	0.20	0.04
		Total:		100.00	100.00	100.00	

Figure D.39: Accurate amount values obtained from the scanned area.

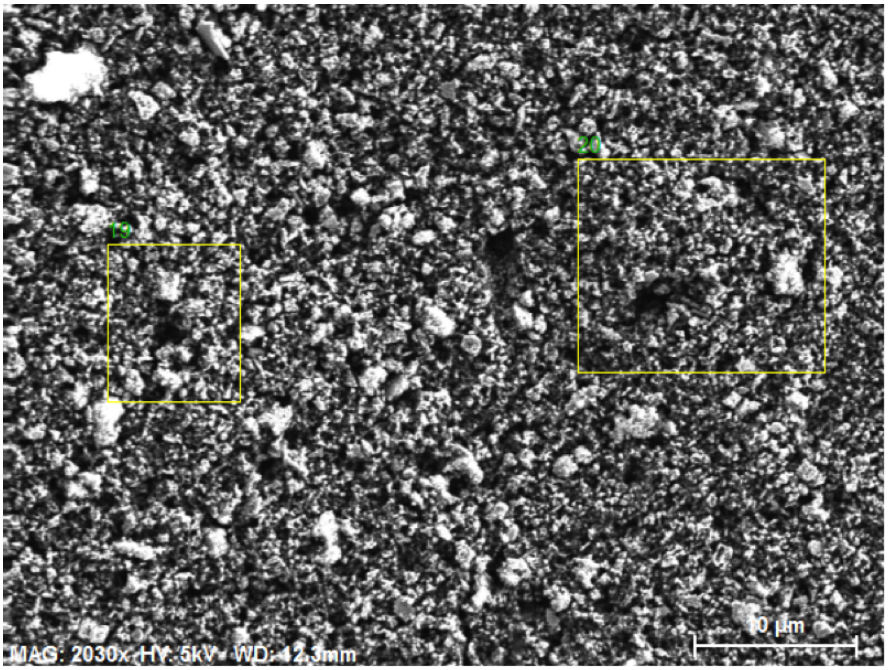

Figure D.40: SEM image showing the two last scanned areas of cathode D, i.e. the two yellow squares in the figure.

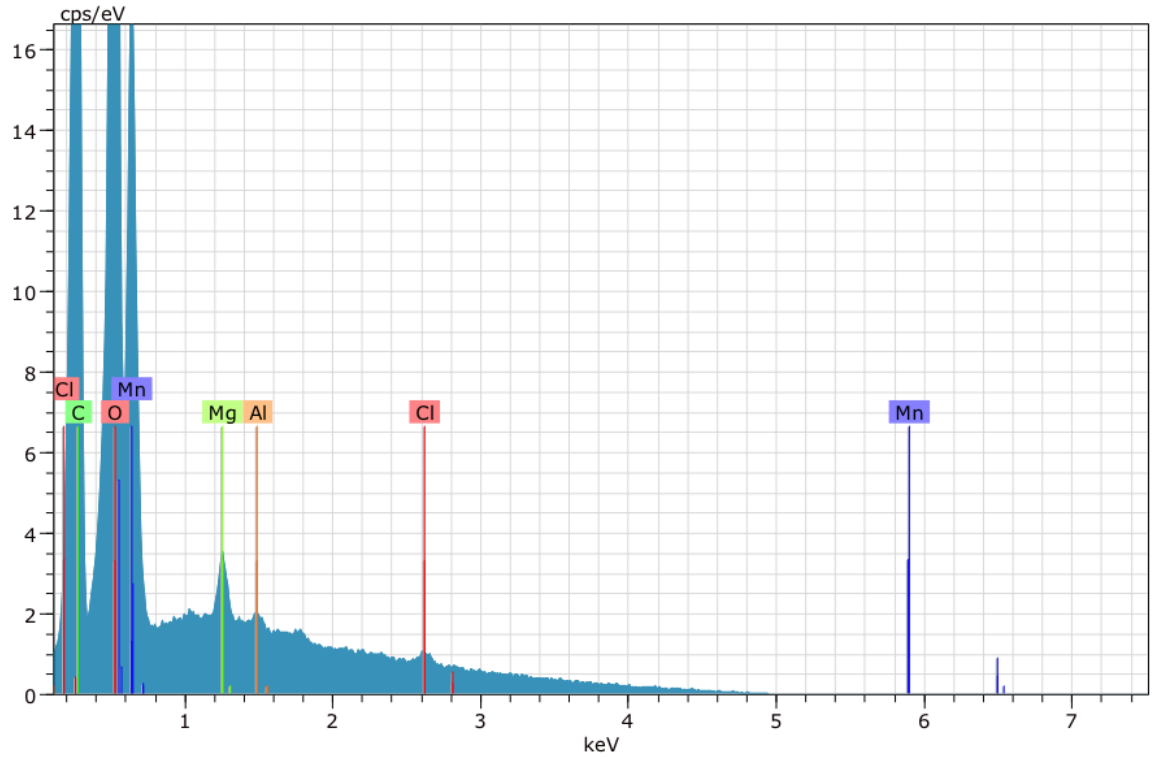

Figure D.41: EDS spectra of the left square in the SEM image above.

Spectrum: 19

El	AN	Series	Net	unn. C [wt.%]	norm. C [wt.%]	Atom. C [at.%]	Error (1 Sigma) [wt.%]
Mn	25	L-series	83859	50.49	50.49	21.24	5.77
O	8	K-series	126293	28.15	28.15	40.66	3.16
C	6	K-series	80631	18.71	18.71	36.00	2.16
Cl	17	K-series	2021	1.36	1.36	0.89	0.11
Mg	12	K-series	5632	1.14	1.14	1.09	0.09
Al	13	K-series	651	0.15	0.15	0.13	0.04
		Total:		100.00	100.00	100.00	

Figure D.42: Accurate amount values obtained from the scanned area.

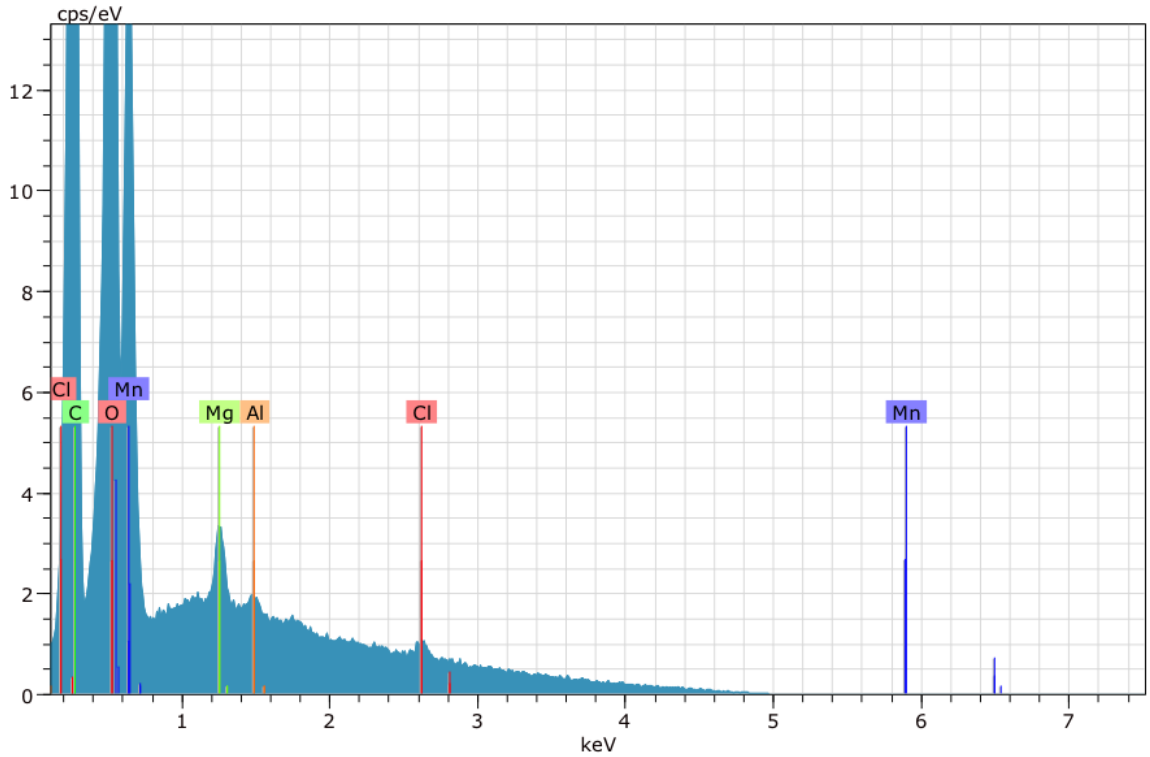

Figure D.43: EDS spectra of the right square in the SEM image above.

Spectrum: 20

El	AN	Series	Net	unn. C [wt.%]	norm. C [wt.%]	Atom. C [at.%]	Error (1 Sigma) [wt.%]
Mn	25	L-series	76825	48.94	48.94	20.17	5.62
O	8	K-series	115341	27.48	27.48	38.88	3.10
C	6	K-series	83126	20.44	20.44	38.52	2.35
Cl	17	K-series	2297	1.64	1.64	1.05	0.12
Mg	12	K-series	6030	1.29	1.29	1.20	0.10
Al	13	K-series	934	0.22	0.22	0.19	0.04
		Total:		100.00	100.00	100.00	

Figure D.44: Accurate amount values obtained from the scanned area.

Appendix E

Ex situ TEM

E.1 Element analysis spectra

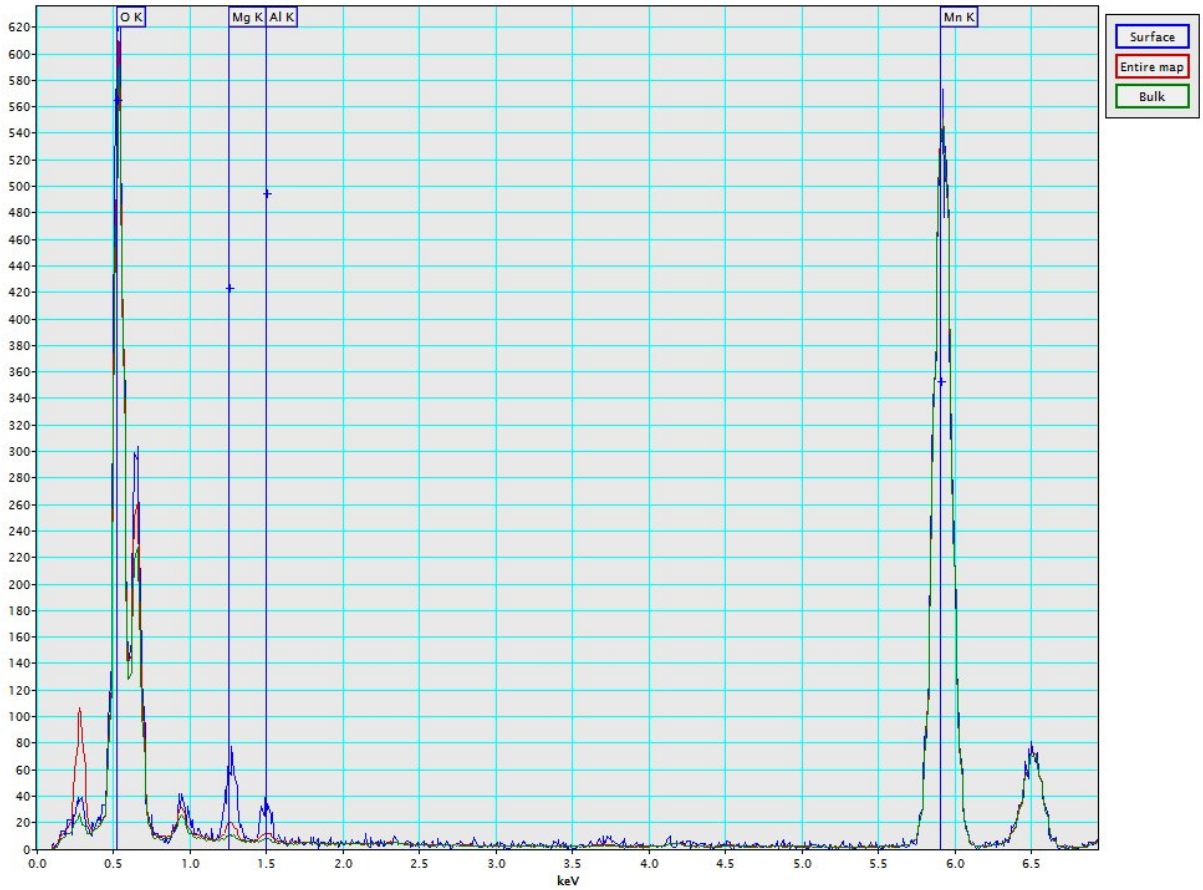

Figure E.1: STEM element analysis spectra for charged sample.

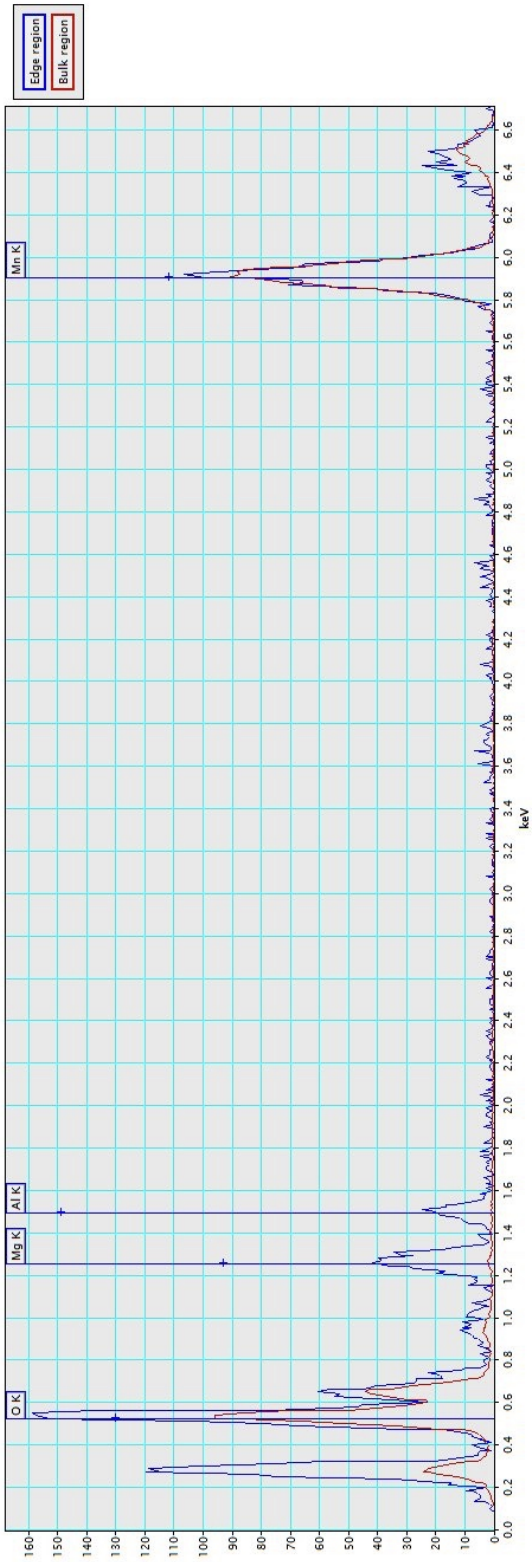

Figure E.2: STEM element analysis spectra for discharged sample.